

VOLUME 32

FEBRUARY 1954

NUMBER 2

# Canadian Journal of Physics

**Editor: G. M. VOLKOFF**

**Associate Editors:**

- L. G. ELLIOTT, *Atomic Energy of Canada, Ltd., Chalk River*
- J. S. FOSTER, *McGill University*
- L. LEPRINCE-RINGUET, *Ecole Polytechnique, Paris*
- D. W. R. MCKINLEY, *National Research Council*
- B. W. SARGENT, *Queen's University*
- F. E. SIMON, *Clarendon Laboratory, University of Oxford*
- W. H. WATSON, *University of Toronto*

**Published by THE NATIONAL RESEARCH COUNCIL  
OTTAWA CANADA**

## CANADIAN JOURNAL OF PHYSICS

(Formerly Section A, Canadian Journal of Research)

The CANADIAN JOURNAL OF PHYSICS is published monthly by the National Research Council of Canada under the authority of the Chairman of the Committee of the Privy Council on Scientific and Industrial Research. The National Research Council publishes also: *Canadian Journal of Biochemistry and Physiology*, *Canadian Journal of Botany*, *Canadian Journal of Chemistry*, *Canadian Journal of Technology*, *Canadian Journal of Zoology*.

Matters of general policy concerning the Council's journals are the responsibility of a joint Editorial Board consisting of: the Editors of the journals; members representing the National Research Council of Canada and the Royal Society of Canada and two other scientific societies; and two ex-officio members.

---

### EDITORIAL BOARD

#### Editors of the Journals

D. L. Bailey, *University of Toronto*  
J. B. Collip, *University of Western Ontario*  
E. H. Craigie, *University of Toronto*

G. A. Ledingham, *National Research Council*  
Léo Marion, *National Research Council*  
G. M. Volkoff, *University of British Columbia*

#### Representatives of the National Research Council

C. W. Argue (Chairman), *University of New Brunswick*  
G. E. Hall, *University of Western Ontario*

T. Thorvaldson, *University of Saskatchewan*  
W. H. Watson, *University of Toronto*

#### Representatives of Societies

D. L. Bailey, *University of Toronto*  
Royal Society of Canada  
E. H. Craigie, *University of Toronto*  
Royal Society of Canada  
H. G. Thode, *McMaster University*  
Chemical Institute of Canada

T. Thorvaldson, *University of Saskatchewan*  
Royal Society of Canada  
G. M. Volkoff, *University of British Columbia*  
Royal Society of Canada  
Canadian Association of Physicists

#### Ex officio

Léo Marion (Editor-in-Chief)  
*National Research Council*

H. H. Saunderson  
*National Research Council*

---

*Manuscripts* should be addressed to:

Dr. Léo Marion,  
Editor-in-Chief,  
*Canadian Journal of Physics*,  
National Research Council,  
Ottawa 2, Canada.

*Subscriptions, renewals, and orders for back numbers* should be addressed to:

Division of Administration,  
National Research Council,  
Ottawa 2, Canada.

*Subscription rate: \$4.00 a year, single numbers: 50 cents.* Remittances should be made payable to the Receiver General of Canada, credit National Research Council.





# Canadian Journal of Physics

*Issued by THE NATIONAL RESEARCH COUNCIL OF CANADA*

VOLUME 32

FEBRUARY 1954

NUMBER 2

## COUNTING SLOW ELECTRONS WITH AN ELECTRON MULTIPLIER<sup>1</sup>

By J. A. COWAN<sup>2</sup>

### ABSTRACT

The efficiency of counting slow velocity electrons by a 12-stage activated beryllium-copper electron multiplier was investigated. The total electron current in the incident beam was measured using an electrometer tube circuit. The number of pulses produced in the multiplier by the whole beam was counted using high speed scaling circuits. The efficiency of counting was thus determined without depending on calibrated slits to divide the beam.

Efficiency curves for primary energies between 200 and 900 ev. are shown for freshly activated surfaces and also for surfaces which had been exposed to still air for five months. The curves were similar in shape, the former being a few per cent above the latter. A maximum of 63% was obtained for 300 ev. input energies.

### INTRODUCTION

The electron multiplier is used frequently as a particle detector. One great advantage is that it operates in a high vacuum and therefore requires no window to separate it from processes occurring in a vacuum. Also, its recovery time is so fast that the over-all counting speed is limited only by the associated circuits.

Quantitative work requires that the counting efficiency be known. Very little work has been published on this aspect of the electron multiplier. For protons with energies of 10 kev., Robson (4) found 100% efficiency with an accuracy of 20%. In this case the current of incident protons was measured with an electrometer circuit and a calibrated slit permitted the protons to enter the multiplier. Also using calibration slits, Allen (1) gave the counting efficiency for electrons as 100% for 500 ev. and 40% for 6000 ev. input energies. Allen's results differ appreciably from those in this paper. The most probable explanation for this discrepancy is that the calibration of his slits was done at much higher currents than those actually used in the efficiency measurement. The curve shown goes over 100% at 300 ev. so the calibration may have changed considerably with the current density.

Since the usefulness of the electron multiplier as a counter depends on its efficiency for detecting the incoming particles, this work was undertaken to

<sup>1</sup> Manuscript received in original form January 28, 1952, and, as revised, October 13, 1953.

Contribution from the Department of Physics, University of Toronto, Toronto, Ontario. Based on a thesis submitted in partial fulfillment of the requirements governing the award of the degree of Doctor of Philosophy at the University of Toronto.

<sup>2</sup> Holder of Studentships under the National Research Council of Canada, 1947-48-49-50; now at the Defence Research Telecommunications Establishment (Electronics Laboratory), Ottawa.

investigate the possibility of using an electron multiplier for quantitative measurements of low velocity electrons which could if necessary be accelerated up to a few hundred volts within the detector.

## DESCRIPTION OF APPARATUS

### *Electron Multiplier*

The electron multiplier was of similar design to that used by Allen (1), that is, a 12-stage multiplier with electrostatic focusing. The multiplier plates were made of 0.010 in. sheet beryllium copper. Nickel wires were spot-welded to the edges of the plates which fitted into holes in the supporting mica to give accurate positioning. Details of the spacing and curvature of these plates are shown in Fig. 1. The mica was held by screws to brass plates which in turn were bolted to the removable cover of the vacuum container. After being cleaned, the plates were activated by heating to a dull red heat in air at a pressure of  $10^{-3}$  mm. Hg for 20 min.

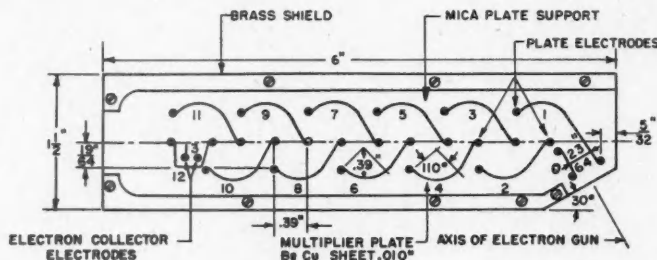


FIG. 1. Cross section of the electron multiplier.

The voltage divider which supplied potential to the plates consisted of 12 2.2-megohm (1 w., 1%) resistors. Since Welwyn resistors were found to have excellent degassing properties, this voltage divider was placed inside the vacuum container. Thus only one insulated seal was required and the resistors were shielded.

The output pulses from the electron multiplier are due to a number of electrons arriving at its collector. To make these pulses a maximum the effective output capacity was kept to a minimum in the following ways: (1) the collector was made as small as possible; (2) leads were kept short; (3) a cathode follower was used as the initial tube in the following circuits. The capacity of the collector, including wiring and the input capacity of the first tube, was measured to be  $23 \mu\text{f}$ . The time constant of the multiplier load and all stray capacities in the apparatus used was  $0.25 \mu\text{sec}$ . Making allowance for a random distribution of pulses with time, this allows counting at the rate of  $10^5$  counts per second with a statistical error due to unresolved counts of  $2\frac{1}{2}\%$  (3).

To obtain the optimum value of the over-all voltage applied to the multiplier, a curve was taken of the number of counts, for a constant input, as the H.T.

voltage was varied. A value of 5000 v., 417 v. per plate, was chosen as it was in the middle of a broad maximum on this curve. The discrepancy between this value and the maximum of the efficiency curve (see results) is probably due to the fact that the best focusing of the multiplier plates occurs at 417 v.

#### Electron Gun

An electron gun was used as the source of primary electrons for testing the multiplier. Currents of the order of  $10^{-14}$  amp. were obtained by using small limiting apertures in the grid and also by using a temperature limited filament. The geometry of the system was such that any electron going through both apertures would strike the first plate of the multiplier. The ratio of the grid accelerating voltage and the anode voltage was always set at such a value that the electrons converged as they approached the multiplier. The structure of this gun is shown in Fig. 2.

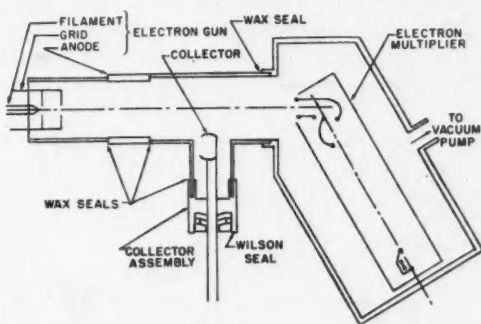


FIG. 2. Diagram of the electron gun, multiplier, and collector.

The filament was a U-shaped 0.005 in. diameter tungsten wire, requiring about four watts input power. Since the gun was temperature limited it was necessary to stabilize the heating voltage supplying it. A 200 amp.-hr. storage battery was used in parallel with a selenium rectifier charging circuit. The charging current was kept within 0.1 amp. of the filament current to assure constancy of voltage over a period of an hour. This voltage changed by less than 0.0005 v. as measured on a potentiometer.

#### Collector

The collector was designed to pick up the total beam from the electron gun. It was a brass cup threaded onto the end of the moving rod of a sliding vacuum seal which allowed the rod to be pushed in or out. The side arm (see Fig. 2) in the glass section was made large enough to house the collector so it could be drawn completely out of the electron beam. The glass surfaces were coated with dri-film to ensure against electrical leakage, since the resistance to ground had to be kept high compared with the electrometer grid resistance ( $10^{12}$  ohms).

*Electronic Circuits**(a) Amplifier*

The pulses at the output of the multiplier were of the order of  $10^{-3}$  v. so it was necessary to amplify them in order to trip the scaling circuits. A wide band amplifier, 10 kc. to 8 Mc./s., was used to preserve the pulse shape. For this frequency response the rise time of 10% to 90% of a step function is  $1/20 \mu\text{sec}$ . as stated by Valley and Wallman (5). Since this was much less than the resolving time of the input scaler, the band width was sufficient for this work.

A standard resistance condenser coupled amplifier with peaking coils to extend the high frequency response was used. Its total gain was  $1.5 \times 10^5$ . A multiposition switch on a low impedance attenuator was used as a gain control to assure that the same setting could be obtained repeatedly. A curve of the relative number of counts plotted against the amplifier gain is shown in Fig. 3. A gain of 5000 was used for the efficiency measure as the curve approaches the horizontal at that point. Above this value of gain, noise caused the number of counts to increase. A cascode cathode follower was used as the output tube to feed a negative pulse to the 200 ohm input impedance of the first scaler.

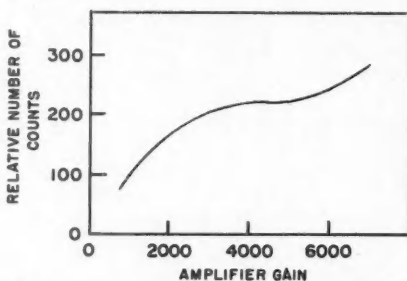


FIG. 3. Graph showing the variation of counting rate with H.T. voltage across the electron multiplier.

*(b) Scaling Circuits*

The first scale-of-four, which required a resolving time of  $\frac{1}{4} \mu\text{sec}$ . to match the output of the multiplier, was designed following the general scheme shown in Vol. 19 of the Radiation Laboratory Series (2). 6AK5 tubes were used for the Eccles-Jordon relays. To speed up the circuit, the anode voltages were limited at  $67\frac{1}{2}$  and 90 v. The circuit used counted regular pulses up to a frequency of 6 Mc./s. Up to this speed no difference was found between 6AL5 tubes and IN35 crystals when used as holding diodes.

The scale-of-four was followed by a scale-of-eight with a resolving time of  $2 \mu\text{sec}$ . This was followed by a commercial scale-of-1000 and mechanical counter with a resolving time of  $10 \mu\text{sec}$ . This combination of scaling circuits was capable of counting random pulses at the rate of  $10^6$  per second with a statistical error of  $2\frac{1}{2}\%$  due to unresolved pulses.

(c) *Electrometer Circuit*

The current measurement was made by a balanced electrometer circuit which is shown in Fig. 4. The variable resistors were used to balance the circuit, so that small changes in battery voltages would cause negligible current flow through the galvanometer in the plate circuit. The control in the filament circuit had the greatest effect on the drift in the value of current through the galvanometer. Other variations due to lack of temperature equilibrium were eliminated by leaving the circuits connected continuously.

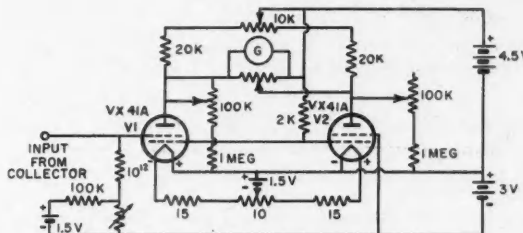


FIG. 4. Schematic diagram of the electrometer circuit.

The value of the effective grid resistance,  $R$ , of the electrometer tube enters into the calculation of current. This resistance consists not only of the actual resistor but also of any leakage paths and the effect of grid current within the tube.

The resistance measurement was made by determining the time constant of discharge of a condenser through  $R$ . To obtain a suitable time constant so that the time could be determined with sufficient accuracy with a stop watch, i.e. order of four minutes, the grid capacity had to be increased by adding an external condenser. Since  $R$  is of the order of  $10^{12}$  ohms the leakage resistance of the condenser must be considered. Thus two variable standard air condensers were used first separately and then in parallel. The discharge curves obtained showed no effect indicating a change in  $R$  throughout the voltage range used in this experiment. Several trials were taken for each case and a least squares solution applied to the results.  $R$  was estimated as  $1.07 \times 10^{12}$   $\pm 1\%$  ohms.

The electrometer circuit was calibrated to find its deflection sensitivity. This was done by noting the deflection of the galvanometer in the plate circuit for a small known voltage added to the control grid of V1 in Fig. 4. With a grid resistance of  $1.07 \times 10^{12}$  ohms and a galvanometer with a sensitivity of  $10^{-10}$  amp. per mm. the sensitivity of the circuit was found to be  $1.9 \times 10^{-17}$  amp. per mm.

#### EFFICIENT MEASUREMENT

The efficiency measurement was done by first measuring the electron beam as a current with an electrometer circuit and then counting the number of pulses produced by the electron multiplier. The whole of the beam was meas-

ured in both cases to eliminate the possibility of the transmission through calibrated slits varying with current density. The size of the current which could be used was governed by the possible accuracies of the two measurements. The larger the input currents the easier it would be to obtain an accurate current reading. On the other hand there is a limit to the speed of counting. A compromise of  $10^{-14}$  amp. or 60,000 electrons per second was chosen since currents are readily measurable down to  $10^{-16}$  amp. and counting is almost impossible with present circuits much above  $10^6$  counts per second. By comparing the number of output pulses per second with the number of electrons per second equivalent to the input current, the efficiency could be found. Efficiency readings were taken for input electron energies ranging from 200 to 900 ev. Below 200 ev. the earth's field and other stray fields affect the electron beam so readings were not taken in that region. Since the maximum efficiency occurs near 300 ev. and the efficiency decreases gradually for higher input energies, readings were not taken above 900 ev.

#### (a) Current Measurement

With all voltages on the electron gun, the collector was placed so the electron beam would enter the middle of the cup. This was checked by moving in the collector while the electron multiplier was operating. The counting rate of the electron multiplier behind the cup was reduced to noise level when the collector was in the correct position, which was not critical. To ensure that no secondary electrons would be lost the collector was made 45 v. positive to the anode.

The gun filament was turned off and the circuit was left for several hours so the electric charges on the glass envelope would come to equilibrium. Then the zero of the galvanometer was found by reading its deflection every 15 sec. for 20 min. The large number of readings allowed the evaluation of drift and also the averaging out of noise fluctuations.

Next the filament of the electron gun was switched on to give a current of about  $10^{-14}$  amp. At the same time the galvanometer deflection was kept near to the zero reading by adjusting the bias voltage in the grid circuit. When the deflection became steady the galvanometer deflections were read every 15 sec. for 20 min. as before.

The additional bias voltage almost balances the voltage caused by the current of the collected electrons flowing through the grid resistance ( $1.07 \times 10^{12}$  ohms). The two sets of deflection readings were plotted against time and the mean curves drawn. By extrapolating the curve from the first set of readings to allow for the steady drift, the change in deflection of the galvanometer was found at the end of the second set of readings. This deflection was multiplied by the sensitivity of the circuit and added to the current measurement (from the bias setting) as a small correction.

#### (b) Counting Measurement

Immediately after the electrometer measurement the collector was withdrawn from the electron beam and the 45 v. bias removed from it. The multi-

plier voltages were switched on and the reading of the mechanical counter taken every minute for 20 min.

The number of counts per minute was plotted against time and the curve extrapolated back to the time at which the difference in electrometer deflection was taken in part (a) above. The statistical correction (3) for the number of counts lost as a result of the  $\frac{1}{4} \mu\text{sec}$ . resolving time was added to the counting reading. This correction was usually less than  $2\frac{1}{2}\%$ .

From these two measurements, (a) and (b), the efficiency can be found by dividing the value of the counting measurement by the value of the current measurement in the same units.

An example of an efficiency measurement is shown in Fig. 5. A and B show

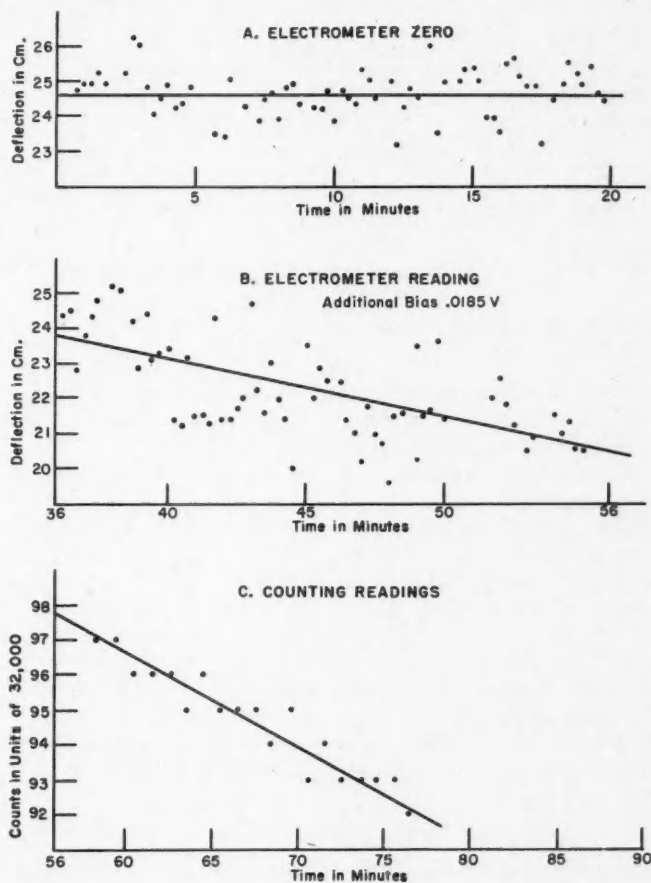


FIG. 5. Sample of the current and counting readings.

the readings of the galvanometer deflections. The large variation is due mainly to the thermal noise in the effective grid resistance of the electrometer tube. Averaging many readings tends to minimize the effect of this noise. Fig. 5C shows the counting readings. The slope of the current and counting curves is due to the gradual decrease of the electron emission of the electron gun. During a measurement, the current and counting readings decreased similarly.

### RESULTS

The electron multiplier efficiency curve for different primary energies is shown in Fig. 6. From 200 to 275 ev. the curve rises steeply; from 275 to 350 ev. there is a broad maximum at approximately 63% efficiency; above 350 ev. the efficiency decreases gradually to 56% at 900 ev. Activated multiplier

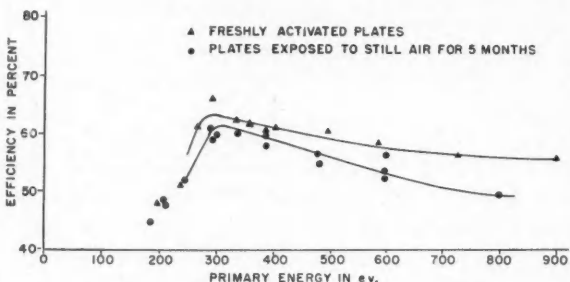


FIG. 6. Graph showing the efficiency of counting low velocity electrons with a Be-Cu electron multiplier.

plates which had been exposed to still air for five months gave a very similar curve. This would indicate that plates activated in the manner described were very stable towards exposure to still air.

The maximum deviation from the efficiency curve is about 5% giving a probable error of about 2%. The measured efficiency for primary energies below 225 ev. may be too high. This is probably due to electrons not being picked up by the collector and still striking the first plate of the multiplier. This effect was definitely detected below 200 ev.

As shown by the efficiency curves, the electron multiplier can be used directly for counting electrons with energies down to 250 ev. with efficiencies over 50%. The electron multiplier permits very fast counting but its main disadvantage is that the output pulses have a large range of amplitude. Since the electron multiplier operates in a vacuum and has its maximum efficiency at about 300 ev., it is evident that very slow electrons of the order of a few volts in energy may easily be accelerated, in the detector itself, to a speed permitting counting.

### ACKNOWLEDGMENTS

The author wishes to express his thanks to Prof. J. M. Anderson and Prof. R. W. McKay who gave valuable advice and assistance at all times.

During this investigation financial assistance was received from the National Research Council by studentships (1947-1950).

## REFERENCES

1. ALLEN, J. S. *Rev. Sci. Instr.* 18: 739. 1947.
2. CHANCE, B., HUGHES, V., MACNICHOL, E. F., SAYRE, D., and WILLIAMS, F. C. *Waveforms*. Vol. 19, M.I.T. Radiation Laboratory Series. McGraw-Hill Book Company, Inc., New York. 1948. p. 607.
3. LEWIS, W. B. *Electrical counting*. MacMillan & Co., Ltd., London. 1942. p. 116.
4. ROBSON, J. M. *Rev. Sci. Instr.* 19: 865. 1948.
5. VALLEY, G. E. and WALLMAN, H. *Vacuum tube amplifiers*. Vol. 18, M.I.T. Radiation Laboratory Series. McGraw-Hill Book Company, Inc., New York. 1948. p. 80.

# FINE STRUCTURE OF THE SCHUMANN-RUNGE BANDS NEAR THE CONVERGENCE LIMIT AND THE DISSOCIATION ENERGY OF THE OXYGEN MOLECULE<sup>1</sup>

BY P. BRIX<sup>2</sup> AND G. HERZBERG

## ABSTRACT

The Schumann-Runge absorption bands of  $O_2$  ( $B^3\Sigma_u^- - X^3\Sigma_g^-$ ) have been photographed in the fourth order of a 3 m. vacuum spectrograph with a resolution of 160,000. Some spectra were taken with the  $O_2$  at liquid air temperature. A detailed fine structure analysis has been carried out for all bands with  $v' > 11$ . In addition to the six main branches (with  $\Delta J = \Delta N = \pm 1$ ), for low values of the quantum number  $N$  (total angular momentum apart from spin), several lines of the six satellite branches (with  $\Delta N = \pm 1$ ,  $\Delta J = 0, \mp 1$ ) as well as of the two "forbidden" branches (with  $\Delta N = \pm 3$ ,  $\Delta J = \pm 1$ ) have been identified. Values of the rotational constants and the vibrational quanta in the upper state have been derived up to  $v' = 21$ . The triplet splitting increases rapidly with  $N$  and with  $v'$ ; it cannot be described accurately by the known theoretical formulae.

The origin of the 21-0 band is at  $57115 \text{ cm}^{-1}$ . A very short extrapolation gives the convergence limit at  $57128 \pm 5 \text{ cm}^{-1}$ . This limit agrees excellently with the one derived from the near ultraviolet ( $A^3\Sigma_u^+ - X^3\Sigma_g^-$ ) bands if it is assumed that at both limits those  $O$  atoms that are produced in the  ${}^3P$  state are in the lowest component level of this state, viz.  ${}^3P_2$ . A discrepancy pointed out earlier by Herzberg is thus removed. The convergence limit just mentioned and certain other data derived from the spectrum lead to very precise information about the dissociation energy of  $O_2$ . Without any extrapolation the dissociation energy into normal atoms can be given as  $41260 \pm 15 \text{ cm}^{-1}$  (or  $5.114 \pm 0.002 \text{ ev.}$  or  $117.96 \pm 0.04 \text{ kcal./mole}$ ), which is 0.63% higher than the old value.

## A. INTRODUCTION

The rotational structure of the Schumann-Runge absorption bands of  $O_2$  has been analyzed by Curry and Herzberg (4) for low values of the vibrational quantum number  $v'$  of the upper state ( $v' = 1, 2, \dots, 7$ ) and by Knauss and Ballard (12) for higher  $v'$  values ( $v' = 4, 5, \dots, 15$ ). In emission the Schumann-Runge bands have been studied by Lochte-Holtgreven and Dieke (13) for values of  $v' = 0, 1, 2$  and  $v'' = 11, 12, \dots, 21$ . While these bands have long been known to be due to a  ${}^3\Sigma_u^- - {}^3\Sigma_g^-$  transition (Mulliken (17)), no detailed analysis of the triplet structure has been made except that Lochte-Holtgreven and Dieke did observe a splitting of the lines of high rotational quantum number and Knauss and Ballard found a splitting of the lines of the 14-0 and 15-0 bands.

Slightly different values for the convergence limit of the Schumann-Runge bands have been obtained by different methods of extrapolation, the most recent ones being  $56877 \text{ cm}^{-1}$  (Gaydon (7)) and  $56859 \text{ cm}^{-1}$  (Herzberg (10)). Since the upper state  $B^3\Sigma_u^-$  dissociates into one normal ( ${}^3P_2$ ) and one excited ( ${}^1D_2$ ) oxygen atom (Herzberg (9)), and since the term difference  ${}^3P_2 - {}^1D_2$  is well known from the OI spectrum, the dissociation energy  $D_0^0$  of the  $O_2$  molecule in its ground state is immediately obtained from the convergence limit of the

<sup>1</sup> Manuscript received August 24, 1953.

Contribution from the Division of Physics, National Research Council, Ottawa, Canada.  
Issued as N.R.C. No. 3127.

<sup>2</sup> National Research Laboratories Postdoctorate Fellow.

Schumann-Runge bands. This is the value usually quoted in the literature. However, in a recent paper (Herzberg (11)) it was pointed out that a precise evaluation of the convergence limit of the near ultraviolet ( $A^3\Sigma_u^+ - X^3\Sigma_g^-$ ) bands of O<sub>2</sub> leads to a value for  $D_0^0(O_2)$  that is 220 cm<sup>-1</sup> higher than that obtained from the Schumann-Runge bands. This discrepancy can be explained either by the assumption that at the two convergence limits the O atoms are in different component states of the  $^3P$  ground state or by the assumption that the extrapolation of the convergence limit of the Schumann-Runge bands is inaccurate.

In order to settle this question and to obtain a definitive value for the dissociation energy of oxygen, new measurements of the Schumann-Runge bands near the convergence limit were undertaken with the new 3 m. vacuum spectrograph of this laboratory. Since near the convergence limit the triplet fine structure of the bands becomes of the same order of magnitude as the rotational structure, a detailed study of this triplet structure was necessary in order to analyze the bands. The problem of the variation of the triplet splitting near the convergence limit is, in itself, one that deserves some interest and about which very little is known at present.

In the present work, all the Schumann-Runge bands from  $v' = 12$  right up to the convergence limit were analyzed and a new value for  $D_0^0(O_2)$  was obtained which we believe is definitive and accurate. This value differs appreciably from the previously accepted value but is close to that derived from the near ultraviolet bands.

#### B. EXPERIMENTAL

The vacuum spectrograph used for the study of the Schumann-Runge bands was of fairly conventional design. A schematic diagram of the apparatus is shown in Fig. 1. Slit S, plate holder P, and grating are all contained in a large pipe of 26 in. internal diameter. Plate holder and grating can be adjusted from outside for various spectral regions without breaking the vacuum. The plate holder which carries 2  $\times$  18 in. plates can be moved up and down so that several spectra can be taken on the same plate.

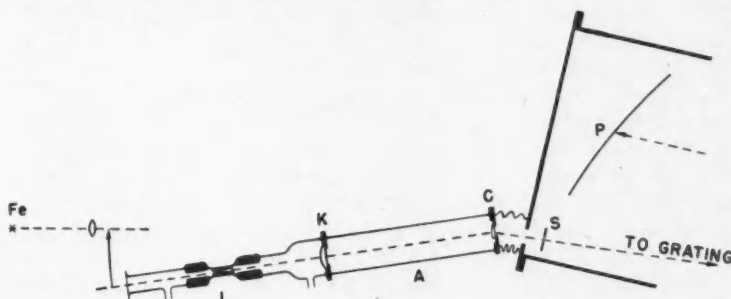


FIG. 1. Diagram of apparatus.  
A: absorption tube, C: cylindrical LiF prism, Fe: iron arc, K: collimator lens, L: Lyman discharge tube, P: plate holder, S: slit. The circular arrow indicates how the arm L, K, A is rotated for the iron arc exposure.

Several gratings were tried as they became available. A grating ruled by D. Richardson of the Bausch and Lomb Co. proved to be the best of these. It has 30,000 lines per inch and a ruled area of  $40 \times 90$  mm. The blaze is at about  $6000 \text{ \AA}$  in first order and correspondingly shorter wave lengths in higher orders.

In building this vacuum spectrograph one of the main objects was to obtain a high resolution by the use of high orders. In order to study spectra in a high order, particularly in absorption, it is necessary to eliminate overlapping lower orders. This was done by means of a cylindrical LiF lens (C in Fig. 1) in the way described by Curry and Herzberg (4). This lens acts as a fore-prism and at the same time forms a line image of the source on the slit. By means of this cylindrical lens it has been possible to obtain absorption spectra down to  $1200 \text{ \AA}$  in the fourth, fifth, and sixth order with dispersions of 0.65, 0.5, 0.4  $\text{\AA}/\text{mm.}$ , respectively, and resolving powers up to 200,000. Because of the much greater intensity of longer wave length light, which is far better reflected by the grating, it is imperative for a successful operation of the fore-prism to exclude completely all light scattered by dust on the prism or small fractures in it. In order to focus different wave length regions on the slit S, the whole arm L, K, A, which was mounted on a triangular bar, was rotated about C, the position of the cylindrical prism.

The absorption tube A (Fig. 1) of 50 cm. length was separated from the spectrograph by the cylindrical prism C and from the light source L by a plano-spherical lens K which produced approximately parallel light through the absorption tube. For some experiments an absorption tube which could be cooled to liquid nitrogen temperature was inserted at A. It consisted of a quartz tube of 27 cm. length with fused-on thin quartz windows. This tube was surrounded by a glass jacket filled with liquid nitrogen and this in turn was surrounded by an evacuated brass tube.

The light source was a Lyman discharge tube viewed end-on. A  $2 \mu\text{f.}$  condenser was charged to 16,000 volts and discharged through the tube which was lined with a  $\text{ZrO}$  liner of 3 mm. internal diameter. From 100 to 1000 flashes were required for an exposure depending on the slit width used, the type of plate, the spectral region, and other factors. After about 8000 to 10000 flashes the liner had to be renewed since its diameter had increased to 5 mm. and the spectrum became more and more spoiled by many emission lines.

For most exposures Ilford Q2 plates were used; for a few final exposures Ilford Q1 plates were used which have a much finer grain but require much longer exposure times.

In the present work all spectra were taken in the fourth order. Only the region from the head of the 11-0 band at  $1804 \text{ \AA}$  to the limit of discrete absorption at  $1750 \text{ \AA}$  was studied in detail. The pressure of oxygen in the absorption tube was varied from about 3 to 350 mm. yielding from weak to nearly complete absorption. Fig. 2 gives a general view of the whole region studied. With increasing pressure many weak lines are brought out in the "windows" left by the strong absorption lines (see Fig. 3). Since the strong absorption lines at high pressure appear very broad, several spectra at different pressures had to be measured in order to include all lines at the best conditions for their measurement.

Fig. 2

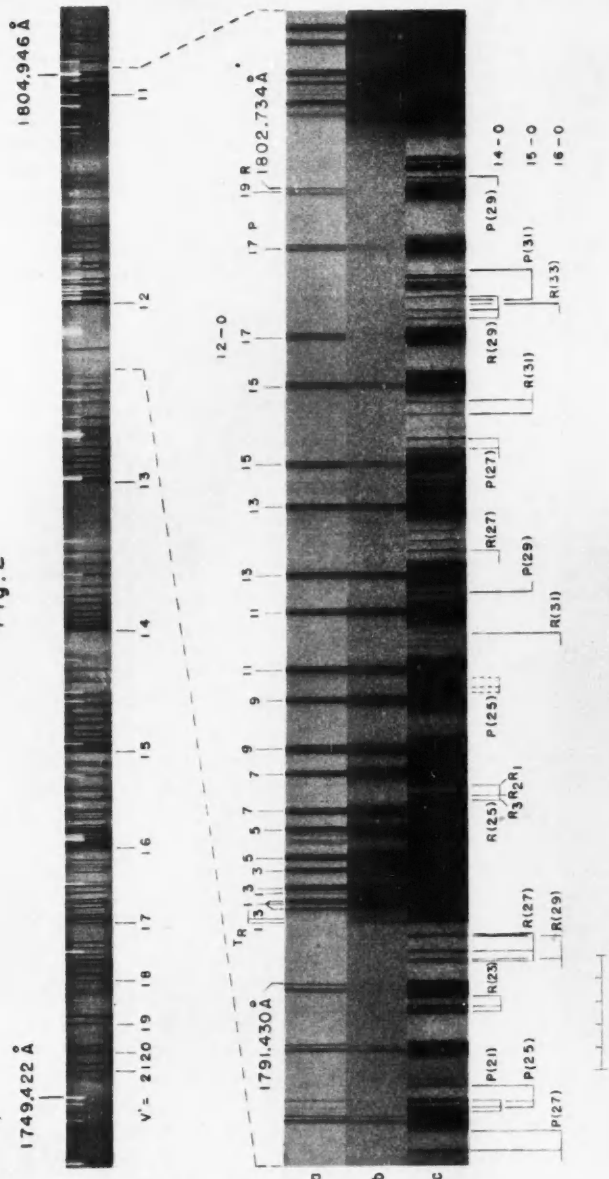


Fig. 3

Fig. 2. Absorption spectrum of  $O_2$  in the region 1750-1805 Å with an absorbing path of 27 cm, and an oxygen pressure of 1.3 mm, at liquid nitrogen temperature (fourth order of 3 m. grating). The iron arc comparison lines (second order) appear at the top of the strip. A similar spectrogram taken at room temperature would show the band heads above  $v' = 15$  much less distinctly.

Fig. 3. Enlarged portion of the absorption spectrum of  $O_2$  in the region 1789–1805 Å. As in Fig. 2, absorption decreases from 3.5 to 0.5 mm $\text{Hg}$  at 1789 Å. A horizontal line at 1805 Å indicates the final ultraviolet temperature ( $b = 15$  mm)  $/ = 97$  cm.

(a) At room temperature and low pressure ( $\rho = 3.0 \text{ mm}$ , path length  $l = 30 \text{ cm}$ ).  
 (b) At room temperature and high pressure ( $\rho = 150 \text{ mm}$ ,  $l = 50 \text{ cm}$ ).

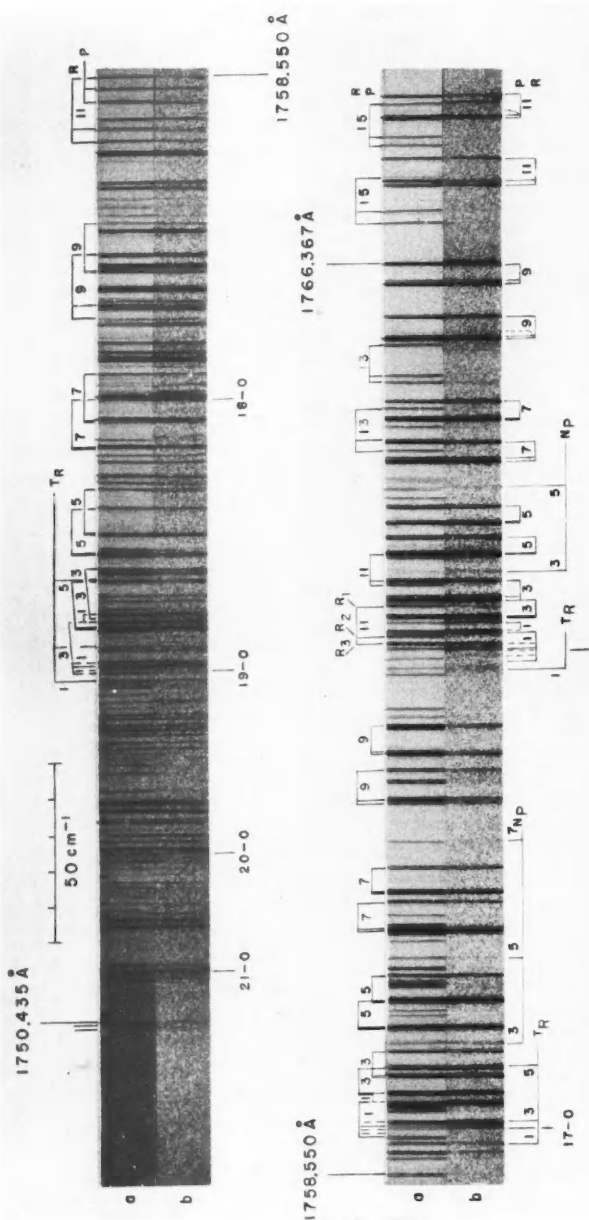


Fig. 4. Enlarged portion of the absorption spectrum of  $O_2$  near the convergence limit (1750-1768 Å). The top strips (a) are from a spectrum taken at room temperature (same plate as Fig. 3a), the bottom strips (b) from one taken at liquid nitrogen temperature (same plate as Fig. 2). Lines are marked for the 18-0, 17-0, 19-0 bands. For the 18-0, 20-0, 21-0 bands only the origins (of the  $\bar{P}_2$  components) have been indicated. Broken leading lines refer to satellite lines, dotted leading lines to the extra lines originating from perturbations. A very conspicuous perturbation can be noticed in the  $R(7)$  and  $P(9)$  'lines' of the 16-0 band.

The spectra taken at liquid nitrogen temperature were mainly used for a comparison of intensities. It is seen, for example, from Fig. 3 that most of the lines that appear weakly at room temperature are absent at low temperature indicating that they originate from the high rotational levels of the ground state which are less populated at lower temperature. On the other hand, a few weak lines such as those marked <sup>7</sup>R in Fig. 3 to the left of the 12-0 head are relatively enhanced at low temperature and must therefore originate in low rotational levels.

Some lines were measured on the low temperature plates rather than on the room temperature plates because they are less blended. These lines are marked by L in the tables.

All measurements were made against second order iron lines. These were obtained by sending the light from an iron arc (Fe in Fig. 1) through the source and the absorption tube in a position in which the region 3000-4000 Å was concentrated by the cylindrical prism on the slit. The wave lengths of the Fe lines given in the M.I.T. Tables (8) were converted to vacuum by using Edlén's tables (6). By dividing these vacuum wave lengths by 2, standards were obtained in the fourth order from which the wave lengths of the O<sub>2</sub> lines could be determined. Judging from the agreement of measurements made on different plates, the relative wave numbers of unblended lines are accurate to about  $\pm 0.05 \text{ cm}^{-1}$ , whereas the absolute wave numbers may be in error by  $\pm 0.2 \text{ cm}^{-1}$ . Lines of equal and favorable absorption were resolved when they were more than 0.35  $\text{cm}^{-1}$  apart, thus indicating an actual resolving power of approximately 160,000.

### C. ROTATIONAL ANALYSIS

#### (1) Assignment of Branches

Fig. 5 shows an energy level diagram for a  ${}^3\Sigma_u^- - {}^3\Sigma_g^-$  transition. The figure is drawn to scale for the 15-0 band of the Schumann-Runge system and shows at the bottom the resulting spectrum for low values of  $N$ , the rotational quantum number corresponding to the total angular momentum apart from spin<sup>1</sup>. In a  ${}^3\Sigma$  state, for each value of  $N$ , except  $N = 0$ , there are three sublevels designated  $F_1, F_2, F_3$  depending on whether the quantum number  $J$  of the total angular momentum including spin is  $N + 1, N$ , or  $N - 1$ , respectively. The selection rules applicable to a  ${}^3\Sigma - {}^3\Sigma$  transition are

$$\Delta J = 0, \pm 1, \Delta N = \pm 1, s \longleftrightarrow a, + \longleftrightarrow -.$$

All of these rules, except  $\Delta N = \pm 1$ , apply rigorously. The two symmetry rules are automatically fulfilled since, on account of the zero nuclear spin of O<sup>16</sup>, only symmetric levels ( $s$ ) occur and since, therefore, in the upper state only "negative", in the lower state only "positive" rotational levels occur. On the basis of the selection rules for  $J$  and  $N$ , the twelve branches  $P_1, P_2, P_3, R_1, R_2, R_3$  and  ${}^P Q_{12}, {}^P Q_{23}, {}^P R_{13}, {}^R Q_{21}, {}^R Q_{32}, {}^R P_{31}$  result which are indicated by full and broken vertical lines in Fig. 5. According to well-known intensity rules (see Herzberg (10)) the branches with  $\Delta J \neq \Delta N$  have rapidly decreasing intensities

<sup>1</sup>Previously this quantum number was designated  $K$ . We follow here the recent recommendation of the Joint Commission for Spectroscopy (J. Opt. Soc. Amer. 43: 410, 1953).

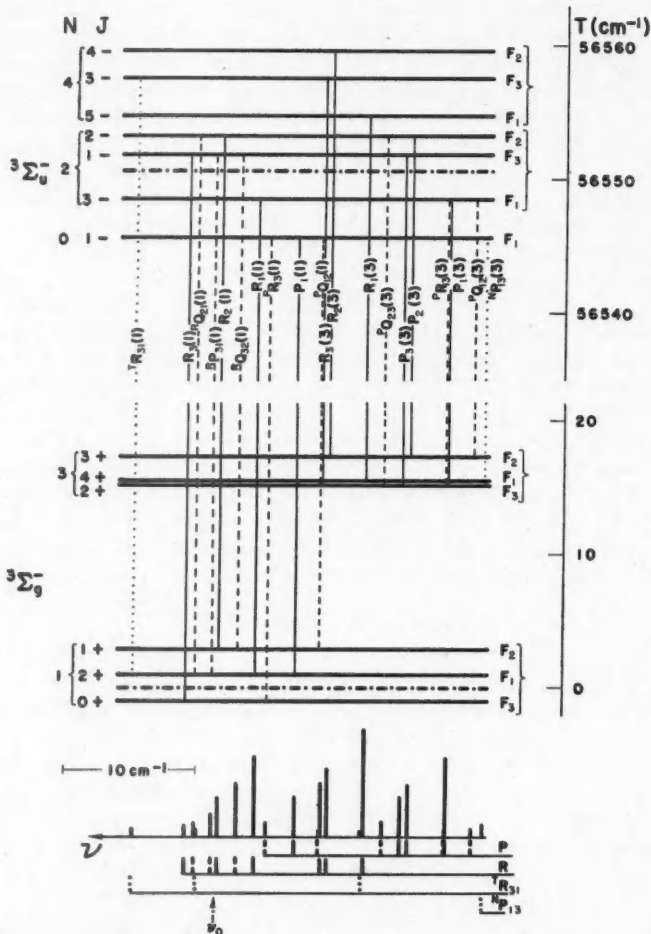


FIG. 5. Energy level diagram of a  $^3\Sigma_u^- - ^3\Sigma_g^-$  band.

The figure is drawn to scale for the 15-0 band of the Schumann-Runge system. The vertical lines representing the transitions are drawn in such a way that their projections below give a representation of the spectrum. The main branches are indicated by full lines, the satellite branches by broken lines, and the "forbidden" branches (with  $\Delta N = \pm 3$ ) by dotted lines. The (nonexisting)  $N = 0, J = 0$  levels and, correspondingly, the band origin  $\nu_0$  are marked by dot-dash lines. Estimated intensities are indicated by different heights of the "lines" in the schematic spectrum. The lines  $^7R_{31}(3)$  and  $^7R_{31}(5)$  originating from higher rotational levels of the upper state could not be shown in the energy level diagram. Their positions have, however, been marked in the schematic spectrum below because they fall into the region of the band head. The lines  $^7Q_{13}(1)$  and  $^7R_{13}(3)$  as well as the satellite lines for the  $R(3)$  transition (not drawn) have not been observed in any of the bands under investigation.

with increasing  $J$ ; they are satellite branches, while the branches with  $\Delta J = \Delta N$  are the main branches with the regular intensity distribution characteristic of normal branches. In the present case in addition to the main branches, lines of all six satellite branches have been observed at low  $N$  values.

The selection rule  $\Delta N = \pm 1$ , while not rigorous, is a fairly strong rule for  $\Sigma - \Sigma$  transitions. Exceptions to this rule have up to now been observed only in forbidden transition in which the normal branches are rigorously forbidden by the symmetry rules, e.g., in the  ${}^3\Sigma_u^+ - {}^3\Sigma_g^-$  bands (11) of O<sub>2</sub>. Such transitions violating the  $\Delta N = \pm 1$  rule (but in accord with the other rigorous selection rules) may be produced by spin-orbit interaction. The present case appears to be the first one in which such transitions have been observed in an allowed band system. The transitions with  $\Delta N = \pm 3$  are of this type. They are marked by dotted lines in Fig. 5 and designated  ${}^7R_{31}$  and  ${}^NP_{13}$  (or, for short,  ${}^7R$  and  ${}^NP$ ). It is easily seen from Fig. 5 that they are the only branches of this type possible in a  ${}^3\Sigma_u^- - {}^3\Sigma_g^-$  transition. They have been observed to occur weakly at low  $N$  values in all the Schumann-Runge bands investigated here and can be identified particularly well on the low temperature spectra (see Figs. 3 and 4). The  ${}^7R$  branch gives rise to lines on the shortward side of the band head formed by the main  $R$  branches. The satellite and forbidden branches are mainly responsible for the crowding of lines near the band heads.

The main  $P$  and  $R$  branches of the 12-0, 13-0, 14-0, 15-0 bands can be readily picked out by inspection. The assignments agree with those of Knauss and Ballard (12). The branches can be followed to high  $N$  values even when they pass through several bands of lower  $v'$  values which obscure certain regions of the branches under consideration. In Fig. 3 some of the lines of high  $N$  (up to  $N'' = 33$ ) are marked.

The identification of the satellite and forbidden branches is not quite as straightforward. However, as mentioned before, it was greatly aided by the low temperature spectrograms. On the other hand, it can be seen from Fig. 5 for the 15-0 band how the exact wave numbers of the lines of the forbidden branches  ${}^NP_{13}$  and  ${}^7R_{13}$  allow one to ascertain which components of the main branches are  $P_1, R_1$ , which  $P_2, R_2$ , and which  $P_3, R_3$ . It turns out that in all unperturbed bands the order is with increasing wave number  $P_1, P_2, P_3$  and  $R_1, R_2, R_3$ . (Only  $R_2(7), R_3(7)$  and  $P_2(9), P_3(9)$  of the 19-0 band were found to be interchanged owing to a perturbation.)

The triplet splitting is very small for the 12-0 band, and is only partially resolved for  $N < 17$ . It increases rapidly with increasing vibrational and rotational quantum numbers, e.g., for the  $R(29)$  "line" of the 14-0 band (see Fig. 3c) the total splitting has reached  $9 \text{ cm}^{-1}$ , and in the 19-0 band a total splitting of  $18 \text{ cm}^{-1}$  occurs for the  $R(11)$  "line" (see Fig. 4a).

For the 16-0 and higher bands, perturbations (cf. Fig. 4) involving extra lines and intensity anomalies occur. These perturbations in addition to the large fine structure splittings made the analysis somewhat difficult. The known energy levels of the ground state and a comparison of line intensities at the two different temperatures were used as the main clues. Once a strong perturbation was encountered it was usually not possible to follow the respective branch to

TABLE IIa  
WAVE NUMBERS OF THE OBSERVED LINES

Explanation of symbols:

<sup>a</sup> Blend with line of comparable intensity.

<sup>§</sup> Indicates that the  $R_2$  and  $R_3$ , or  $P_2$  and  $P_3$ , lines are blended.

<sup>o</sup> Blend with much weaker line.

<sup>†</sup> Wave number has a greater uncertainty, e.g., very faint lines.

Extra lines connected with perturbations are assigned the symbols  $R^x$  or  $P^x$ , respectively.

12-0 band, $\nu_0 = 55784.59 \text{ cm}^{-1}$							13-0 band, $\nu_0 = 56085.51 \text{ cm}^{-1}$												
$N''$	$P_1$	$P_2$	$P_3$	$R_1$	$R_2$	$R_3$	$N' P_{15}$	$T_{R_{15}}$	$N''$	$P_1$	$P_2$	$P_3$	$R_1$	$R_2$	$R_3$	$N' P_{13}$	$T_{R_{13}}$		
1	55780.75	—	—	55784.40	55785.24*	—	—	55783.12†	3	5770.80§	752.71§	765.76§	55778.64§	765.13§	—	791.23†	55782.88		
3	770.10	55770.80§	—	777.99	778.04§	—	—	—	5	752.10	727.71§	764.40	765.13§	744.58§	744.58§	—	783.78*		
5	752.10	732.71§	—	743.73	743.73	—	—	—	7	727.13	695.80§	716.02	716.02	717.37†	717.37†	—	708.08†		
—	—	—	—	—	—	—	—	—	9	695.01	685.80§	685.80§	685.80§	682.54§	682.54§	—	772.93†		
—	—	—	—	—	—	—	—	—	11	655.82	656.77§	681.32	681.32	640.80§	640.80§	—	—		
—	—	—	—	—	—	—	—	—	13	609.60	610.65§	639.56	639.56	592.16§	592.16§	—	—		
—	—	—	—	—	—	—	—	—	15	556.20	557.55§	590.63	590.63	534.54	536.32§	536.32§	—		
—	—	—	—	—	—	—	—	—	17	495.92	497.18	497.72§	497.72§	471.30	472.92	473.71	—		
—	—	—	—	—	—	—	—	—	19	—	—	—	—	—	—	—	—		

14-0 band, $\nu_0 = 56340.47 \text{ cm}^{-1}$							15-0 band, $\nu_0 = 56350.54 \text{ cm}^{-1}$												
$N''$	$P_1$	$P_2$	$P_3$	$R_1$	$R_2$	$R_3$	$N' P_{13}$	$T_{R_{31}}$	$N''$	$P_1$	$P_2$	$P_3$	$R_1$	$R_2$	$R_3$	$N' P_{13}$	$T_{R_{31}}$		
1	56335.47	—	56326.38 <sup>§</sup> L	56338.77*	56340.54*	56333.02 <sup>§</sup>	—	56347.42	1	56344.56	—	56340.34*	56352.83†	—	56356.71L	56337.53*	—		
3	324.34	—	307.14 <sup>§</sup> L	307.14 <sup>§</sup> L	315.68	317.74 <sup>§</sup>	333.02 <sup>§</sup>	343.40*	3	533.13*	516.40 <sup>§</sup>	516.40 <sup>§</sup>	516.36	512.21 <sup>§</sup>	512.21 <sup>§</sup>	512.21 <sup>§</sup>	56346.66	56346.66	
5	305.19	—	280.37 <sup>§</sup>	280.37 <sup>§</sup>	292.67 <sup>§</sup>	294.86 <sup>§</sup>	317.74 <sup>§</sup>	317.74 <sup>§</sup>	5	485.54	488.60 <sup>§</sup>	488.60 <sup>§</sup>	488.60 <sup>§</sup>	525.99 <sup>§</sup>	525.99 <sup>§</sup>	525.99 <sup>§</sup>	552.07*	552.07*	
7	278.30	—	246.02 <sup>§</sup>	246.02 <sup>§</sup>	261.64	264.25 <sup>§</sup>	264.25 <sup>§</sup>	264.25 <sup>§</sup>	7	409.10*	452.97 <sup>§</sup>	452.97 <sup>§</sup>	452.97 <sup>§</sup>	465.76	469.41 <sup>§</sup>	470.00	548.94	548.94	
9	243.69	—	203.74	204.13	223.15	225.72	226.29	226.29	9	405.45	409.30 <sup>§</sup>	409.30 <sup>§</sup>	409.30 <sup>§</sup>	424.97	428.91	429.75	531.77†	531.77†	
11	201.37	—	153.89	154.41 <sup>§</sup>	176.80	179.62 <sup>§</sup>	180.39	180.39	11	353.20	357.10	357.97	357.97	360.29	381.53	388.10L	322.21†	322.21†	
13	151.32	—	996.28	997.20 <sup>§</sup>	122.62 <sup>§</sup>	125.59	126.81	126.81	13	327.75	630.87	632.07	632.07	640.49	665.52†	665.52†	328.14	328.14	
15	993.44 <sup>§</sup>	—	872.95 <sup>§</sup>	872.95 <sup>§</sup>	878.41	912.64	55916.64	55916.64	15	55959.13	55959.13	55959.13	55959.13	55985.93†	55985.93†	55985.93†	—	—	
17	872.95 <sup>§</sup>	—	876.37	876.37	879.63	826.62	820.95	820.95	17	680.84	690.81	693.06	693.06	732.46	737.18	739.92	—	—	
21	872.95 <sup>§</sup>	—	680.37	680.37	690.81	588.29	630.02	630.02	21	585.49	585.49	588.29	588.29	519.16	524.77	528.12†	—	—	
23	783.78 <sup>§</sup>	—	680.84	680.84	690.81	588.29	588.29	588.29	23	467.08	517.08	517.08	517.08	519.16	524.77	528.12†	—	—	
25	680.37	—	680.84	680.84	690.81	588.29	588.29	588.29	25	585.49	585.49	588.29	588.29	519.16	524.77	528.12†	—	—	
27	580.84	—	585.49	585.49	588.29	588.29	588.29	588.29	27	467.08	517.08	517.08	517.08	519.16	524.77	528.12†	—	—	
29	467.08	—	517.08	517.08	517.08	517.08	517.08	517.08	29	517.08	517.08	517.08	517.08	519.16	524.77	528.12†	—	—	
31	507.49	—	517.08	517.08	517.08	517.08	517.08	517.08	31	507.49	517.08	517.08	517.08	519.16	524.77	528.12†	—	—	

TABLE Ia (Concluded)

16-0 band, $\nu_0 = 56719.50 \text{ cm}^{-1}$									
$N''$	$P_1$	$P_2$	$P_3$	$R_1$	$R_2$	$R_3$	$N P_{13}$	$T_{R_{13}}$	
1	56711.94	—	56704.64	56705.72*	56714.65	56718.99	56721.72*	56724.48†	
3	700.37*	—	694.40§	694.40§	705.72*	710.28§	693.05§	674.90*	$P R_{13}(1) = 56714.02$
5	679.97	—	655.68§	655.68§	688.30	693.05§	697.76*	682.95	$R Q_{21}(1) = 720.78\ddagger$
7	650.96	—	662.07*	662.07*	666.73	667.76*	642.45	682.95	$R P_{21}(1) = 719.47$
9	613.38	—	618.84*	618.84*	627.72	633.32	633.90	633.90	$R O_{21}(1) = 717.66\ddag$
11	567.40	—	573.06	573.06	584.62	590.63	591.77	581.77	$P Q_{13}(3) = 697.93\ddag$
13	513.18*	—	518.82	518.82	533.13*	539.34*	541.15	541.15	$P Q_{21}(3) = 706.69$
15	449.60*	—	456.21	457.90	472.60	479.69	481.92	481.92	$R Z_{21}(7) = 697.71\ddag$
17	377.96	—	385.00	387.17	403.61	411.20*	414.04	414.04	$P Z_{21}(9) = 618.84\ddag$
19	307.81	—	307.81	333.81	333.81	337.53*	271.61†	369.97	$R Z_{13}(9) = 631.92$
21	208.13	—	216.35	219.89	238.92	247.67	252.03	252.03	$P Z_{13}(11) = 671.59$
23	109.95	—	118.73	118.73	143.03	143.03	147.07	147.07	$R Z_{13}(23) = 160.88$
25	992.78	—	55865.40	55901.60	55923.72	55973.73	55890.95	55890.95	$P Z_{13}(25) = 020.46$
27	55866.43	—	55865.40	55901.60	55923.72	55973.73	55890.95	55890.95	
29	—	—	—	—	—	—	—	—	
31	625.52	—	666.04	666.04	666.04	666.04	666.04	666.04	
33	33	—	532.20	532.20	532.20	532.20	532.20	532.20	
17-0 band, $\nu_0 = 56852.41 \text{ cm}^{-1}$									
$N''$	$P_1$	$P_2$	$P_3$	$R_1$	$R_2$	$R_3$	$N P_{13}$	$T_{R_{13}}$	
1	56842.30*	—	56837.33*	56838.15	56844.85*	56851.58	56854.33*	56856.49	
3	830.70	—	816.57*	816.57*	835.45	842.30*	824.02§	850.14†	
5	809.62	—	786.51§	786.51§	816.57*	824.02§	804.99*	834.50*	$P R_{13}(1) = 56840.44\ddag$
7	779.63	—	747.81	748.43	789.26	796.63	797.35	772.28	$P R_{21}(1) = 844.83\ddag$
9	740.50	—	700.37*	701.47	752.82	760.80*	761.86	750.57	$R Q_{21}(1) = 853.43\ddag$
11	693.03*	—	643.58	645.75	701.37	715.72	717.66*	778.03†	$R Q_{21}(3) = 852.22\ddag$
13	635.58	—	643.99	645.75	652.97	662.07*	664.46	620.69	$R O_{21}(1) = 850.40$
15	569.71	—	578.61	581.09	580.49	588.72	588.72	602.20	$P Q_{21}(3) = 839.36$
17	494.70	—	503.97	507.48	507.48	507.48	507.48	507.48	

18-0 band, $v_0 = 56954.54 \text{ cm}^{-1}$		19-0 band, $v_0 = 57030.18 \text{ cm}^{-1}$					
$N''$	$P_1$	$P_3$	$P_1$				
1	56941.68	—	56943.70*	$R_1$	$R_3$	$N_{P_{11}}$	$T_{R_{11}}$
3	920.56	56639.05	56640.19	56953.46	56943.70*	56927.44	56958.09*
5	968.01	917.61*	917.61*	923.53	924.22*	923.78	950.13*
7	877.11	886.26	887.00	894.60	896.12	870.60†	952.46
9	834.50*	845.66	847.24	846.27?	855.96	—	927.44*
11	786.51?	795.56	798.14	—	—	—	941.32*
13	726.32	—	—	—	—	—	966.38?
							$P_{R_{11}}(1) = 56943.76^*$
							$R_{P_{11}}(1) = 954.60^*$
							$R_{Q_{11}}(1) = 952.46$
							$P_{Q_{11}}(3) = 941.32^*$
							$R_{11}^x(3) = 966.38?$
							$P_{11}^x(7) = 871.95?$
							$P_{11}^x(9) = 887.33?$
							$N^*P_{11}^x(11) = 776.76?$

$N''$	$P_1$	$P_3$	$P_1$	$R_1$	$R_3$	$N_{P_{11}}$	$T_{R_{11}}$
1	57014.52*	—	57014.52?	57018.47*	57028.07	—	57032.85*
3	002.11	57015.57	57015.57	005.61	018.09	57018.41	57000.12*
5	56679.76	56992.35	56992.35	56985.04	56987.80	56976.29*	004.95
7	947.63*	960.40*	960.40*	994.60	967.82?	942.40	029.88*
9	905.88	919.19	918.64	914.48*	928.46	932.22	027.80
11	854.33*	868.32	871.93*	865.02*	879.54	883.09*	000.12*
13	793.03	807.70	811.16	804.99*	820.71	782.45	016.47*
15	721.72	737.70*	—	735.62*	—	534.35	019.99
17	640.77	—	—	—	—	—	56962.38
19	—	—	—	—	—	—	973.45†
							$P_{R_{11}}(5) = 57010.89?$
							$R_{R_{11}}^x(5) = 56927.44^*$
							$P_{R_{11}}^x(9) = 866.70?$
							$P_{R_{11}}^x(7) = 976.29^*$

<sup>a</sup>It is probable that the following lines also belong to the  $P_{Q_{11}}$  branch:  $P_{Q_{11}}(1) = 56852.22^*$ ,  $P_{Q_{11}}(9) = 56903.78$ ,  $P_{Q_{11}}(11) = 56852.22^*$ ,  $P_{Q_{11}}(5) = 56977.99^*$ ,  $P_{Q_{11}}(7) = 56945.51^*$ ,  $P_{Q_{11}}(9) = 56977.99^*$ .

TABLE Ib

## WAVE NUMBERS OF THE OBSERVED LINES CLOSE TO THE CONVERGENCE LIMIT

This table lists the observed lines from the limit to the head of the 17-0 band (corresponding to the upper spectrogram in Fig. 4) except for the lines definitely assigned to the 18-0 and 19-0 bands. For a complete list of wave numbers in this region, the lines of the 18-0 and 19-0 bands have to be included beyond 57029.88 cm<sup>-1</sup>. Intensities are visual estimates from the plate reproduced in Fig. 4. The designations  ${}^n P_i$ ,  ${}^n R_i$ ,  ${}^n P X_{ik}$ , and  ${}^n R X_{ik}$  will be explained in section D(1).

$\nu_{\text{vac}}(\text{cm}^{-1})$	Intensity	Assignment	$\nu_{\text{vac}}(\text{cm}^{-1})$	Intensity	Assignment
57130.73	1	${}^n P X_{i3}(1)$	57051.94	3	
129.50	1	${}^n R_i(1)$	051.09	0†	
128.65	2	${}^n P X_{i1}(1)$	050.44	3	
117.70	0†		048.26	4	${}^{20} R_5(5)$
116.82	2	${}^n R_i(3)$	047.12	4	${}^{20} R_5(5)$
115.72	2		046.84	1†	${}^{21} R_2(7)$
115.30	2	${}^n P_i(3)$	046.02	3	
114.36	3s	${}^{21} R P_{31}(1)$	045.14	2	
112.98	2u, b	${}^{21} R_2(1)$	043.80	3	${}^{20} P_5(5)$
112.25	1	${}^{21} R Q_{32}(1)$	042.67	3	${}^{20} P_5(7)$
108.73	0b		042.14	1	
103.68	0†		040.78	2	${}^{21} P_2(7)$
102.36	5	${}^{21} R_3(3)$	038.83	2bb,d?	
101.58	1		036.53	1u	
100.55	4	${}^{21} R_2(3)$	035.21	1 <sup>b</sup>	
100.01	3	${}^{21} P_3(3)$	034.78		
099.00	1		034.14	2	
098.41	2	${}^{21} P_2(3)$	032.85	3bb,d?	*
095.69	0†,b?		030.91	3	*
093.88	0†		029.88	2	*
093.30	2	${}^n R_i(5)$	026.48	1	
092.58	1		024.69	3	
091.81	2		022.26	1†,b	
091.04	2	${}^n P_i(5)$	020.90	3	
089.78	3		019.10	3	${}^{20} R_3(7)$
087.36	1b		016.83	3	${}^{20} R_2(7)$
085.64	2		013.01	4	${}^{20} P_3(7)$
084.76	1		010.89	4	${}^{20} P_2(7)$
083.94	3		009.62	1	
082.92	1†,b	${}^{20} R Q_{21}(1)$	009.14	1	
082.22	1	${}^{20} R P_{31}(1)$	004.15	1	${}^{21} R_3(9)$
081.20	2	${}^{20} R_2(1)$	—	1 <sup>c</sup>	
080.14	4	${}^{21} R_3(5)$ , $+{}^{20} R Q_{32}(1)$	002.90	2	
079.59	1		001.62	1	${}^{21} R_2(9)$
078.17	3	${}^{21} R_2(5)$	56998.90	1	
076.46	3	${}^{21} P_2(5)$	998.27	3	${}^{21} P_2(9)$
076.16	0		996.77	2	
074.80	2	${}^{21} P_2(5)$	996.30	1	${}^{21} P_2(9)$
073.00	4		991.33	0	
072.00	3	${}^{20} R_3(3)$	990.65	0	
069.68	8	${}^{20} R_2(3)$	989.85	1	
067.69	3b,d?	${}^{20} P_3(3)$	985.92	1	
066.82	3	${}^{20} P_2(3)$	984.23	0	
065.94	1		982.77	0	
063.91	3		979.03	0†	
058.94	0bb <sup>a</sup>		977.96	3	${}^{20} R_3(9)^2$
057.95	1		975.48	2	${}^{20} R_2(9)$
056.78	2		974.03	0†	
055.93	1	${}^n P_i(7)$	973.45	0†	
055.24	1		972.23	5	
054.50	2		971.39	0	
053.42	2		970.26	3	${}^{20} P_3(9)$
052.56	0		967.82	10	${}^{20} P_2(9)^*$

TABLE Ib (Concluded)  
WAVE NUMBERS OF THE OBSERVED LINES CLOSE TO THE CONVERGENCE LIMIT

$\nu_{\text{vac}}(\text{cm}^{-1})$	Intensity	Assignment	$\nu_{\text{vac}}(\text{cm}^{-1})$	Intensity	Assignment
56965.80	2		56922.47	0	
964.52	1		917.61	10	<sup>20</sup> P <sub>3</sub> (11)*
961.13	2		915.11	2	<sup>20</sup> P <sub>2</sub> (11)
950.71	1		902.54	0	
958.09	1b?	*	901.31	1	
957.16	1		900.80	2	
953.97	2		898.93	2	*
951.40	1d?		891.08	1b	
950.13	3b,d?	*	889.74	0	
948.88	2b		888.64	2	
947.63	4	<sup>21</sup> R <sub>5</sub> (11)*	885.02	1	
945.51	2	*	875.54	1	<sup>21</sup> P <sub>3</sub> (13)
943.22	4	<sup>21</sup> P <sub>2</sub> (11)*	872.37	2	
941.32	2	<sup>21</sup> P <sub>2</sub> (11)*	865.02	5	*
938.77	1		863.35	1	
937.50	2		862.32	1	
936.32	1		861.17	0	
932.96	0		860.34	3	
931.08	0		858.74	6s <sup>d</sup>	
926.68	2	<sup>20</sup> R <sub>5</sub> (11)	854.85	2	<sup>20</sup> P <sub>3</sub> (13)
924.22	8	<sup>20</sup> R <sub>2</sub> (11)*	852.22	2	<sup>20</sup> P <sub>2</sub> (13)*

<sup>a</sup>Possibly several lines.<sup>b</sup>Possibly one broad line.<sup>c</sup>Unresolved group of lines between the two adjacent lines.<sup>d</sup>Probably two lines of intensity 4 and 2.

Abbreviations: b: Broad; bb: very broad.

d: Double.

s: Shaded to shorter wave lengths.

u: Unsymmetrical.

†: Difficult to measure, wave number has a greater uncertainty.

\*: Mainly or partly assigned to 18-0 or 19-0 band.

\*: Probably blended with weak line of 18-0 or 19-0 band.

higher  $N$  values without ambiguity. The assignment of the lines in the 16-0, 17-0, and 19-0 bands is partly shown in Fig. 4.

Tables Ia and Ib contain all the lines that have been assigned to branches. Between 1803 Å and 1759 Å approximately 100 of the weakest lines, out of a total of 500 measured ones, remain unclassified. The fraction of unclassified lines is much larger between 1759 Å and the end of the discrete absorption spectrum at 1750 Å. We have, therefore, listed all wave numbers measured in this region (Table Ib). A discussion of the assignments  ${}^n P_{ik}$  and  ${}^n R_{ik}$  will be given in section D(1).

## (2) Term Values and Rotational Constants

For the lowest vibrational level of the  $X^3\Sigma_g^-$  ground state ( $v'' = 0$ ) the rotational levels are very well known (2, 3, 1). We have not attempted to determine them independently from the Schumann-Runge bands. Rather, the knowledge of the energy levels of the ground state was used to derive the energy levels of the upper state from the observed lines. The usual procedure of using combination differences or combination sums was found to be less practicable

in the present case since many of the branches are incomplete. However, sufficient unblended lines from different branches were usually available to derive the levels of the upper state from the known levels of the ground state.

The following term values of the ground state were adopted: for the  $F_2$  levels ( $J = N$ , cf. Fig. 5), the  $\Delta_2 F_2''$  data given by Babcock and Herzberg were added up, using the mean observed values (Table IV, column 5 of Reference (2)) up to  $N = 25$ , and the computed ones (column 6) for  $N > 25$ . The differences  $F_2 - F_1$  and  $F_2 - F_3$  (measured by Burkhalter, Anderson, Smith, and Gordy (3) and Anderson, Johnson, and Gordy (1) up to  $N = 25$ ) were taken from (11), and for  $N > 25$  from (2). Finally  $2.87 \text{ cm}^{-1}$  were added to refer all term values to the (nonexisting)  $N'' = 0$ ,  $J'' = 0$  level, which incidentally is  $1.09 \text{ cm}^{-1}$  above the lowest actual level  $N'' = 1$ ,  $J'' = 0$  (see Fig. 5).

According to Schlapp (see subsection 3) the term values  $T_2$  of the  $F_2$  components of the  $B^3\Sigma_u^-$  state should follow the simple formula:

$$[1] \quad T_2 - \nu_0 = F_2(N) = B_v N(N+1) - D_v N^2(N+1)^2$$

where  $\nu_0$  is the wave number of the band origin and  $B_v$  and  $D_v$  have their usual meanings. The constants  $\nu_0$ ,  $B_v$ , and  $D_v$  were derived from the "observed" term values by graphical methods. Only for the 13-0 band was equation [1] found to hold within the experimental error (up to  $N' = 26$ ). The data are incomplete for the 12-0 band. For  $\nu' = 14$  and  $\nu' = 15$  slight deviations from equation [1] occur, but inclusion of a term  $H_v N^3(N+1)^3$  did not seem to be justified. For  $\nu' > 15$  large perturbations limit the accuracy of the rotational constants obtained in this way.

For low  $\nu'$  and  $N'$ , the  $P_2$  and  $P_3$  as well as the  $R_2$  and  $R_3$  lines are not resolved.

TABLE II  
ENERGY LEVELS FOR  $\nu' = 21$   
(Term values in  $\text{cm}^{-1}$ )

	$N'$	$J'$	From $R(N'-1)$	$P(N'+1)$	Mean, observed	Calc. <sup>b</sup>
$F_3$	2	1	<sup>a</sup>	57115.18	57115.18	
$F_2$		2	57115.85†	115.66	115.66	57115.62
$F_3$	4	3	117.53	117.58	117.55	
$F_2$		4	117.80†	117.93	117.89	117.91
$F_3$	6	5	121.26†	121.20	121.20	
$F_2$		6	121.30	121.28	121.29	121.26
$F_3$	8	7	125.65	125.68	125.67	
$F_2$		8	125.64	125.66	125.65	125.67
$F_3$	10	9	131.56	(130.99)	131.56	
$F_2$		10	130.98	131.01	130.99	130.99
$F_3$	12	11	(137.32)	137.04	137.04	
$F_2$		12				137.02

<sup>a</sup>From  $R P_{31}(1) : 57115.35†$ , from  $R Q_{32}(1) : 57115.12$ .

<sup>b</sup> $T_2 = [57114.77 + 0.159 N'(N'+1) - 0.000105 N'^2(N'+1)^2] \text{ cm}^{-1}$ .

†A dagger indicates a larger uncertainty.

(<sup>a</sup>) Term values in parentheses have been derived from blends in which the line in question is probably completely hidden by another stronger line.

In order to obtain even in such cases approximate term values for the  $F_3$  levels the following assumptions were made: (1) the calculated  $F_2$  levels are good approximations to the real  $F_2$  levels; (2) both components ( $P_2$  and  $P_3$  or  $R_2$  and  $R_3$ ) have the same intensity. Let  $[F_2]$  and  $[F_3]$  be the term values derived from the wave numbers of the blends using the correct ground state levels. Then obviously

$$[F_2] \approx F_2 - x, \quad [F_3] \approx F_3 + x,$$

and therefore

$$[2] \quad F_3 \approx [F_3] + ([F_2] - F_2)$$

where for  $F_2$  we can use the calculated value (i.e., calculated from the  $B'$  and  $D'$  values obtained from unblended lines).

The final data are collected in Tables II, III, and IV. Table II compares, as an example, the term values obtained from different lines (listed in Table I<sup>b</sup>) for the important  $v' = 21$  vibrational level. The calculated  $F_2$  levels are given in the last column. The band origins  $\nu_0$  and the rotational constants  $B_{v'}$  and  $D_{v'}$  are collected in Table III. In this table, for the sake of completeness, the data given by Knauss and Ballard (12) as well as Curry and Herzberg (4) are

TABLE III  
BAND ORIGINS, VIBRATIONAL QUANTA, AND ROTATIONAL CONSTANTS OF THE SCHUMANN-RUNGE ABSORPTION BANDS

$v'$	$\nu_0$ (cm <sup>-1</sup> )		$\Delta G'(v' + \frac{1}{2})$ (cm <sup>-1</sup> )		$B_{v'}$ (cm <sup>-1</sup> )		$D_{v'}$ (10 <sup>-6</sup> cm <sup>-1</sup> )
	KB(12)	CH(4) Present work	KB(12)	CH(4) Present work	KB(12)	CH(4) Present work	
0		(49357.6) <sup>a</sup>			688.0 <sup>b</sup>		
1		50045.6 <sub>s</sub>			665.1		0.798
2		50710.7 <sub>s</sub>			641.4 <sub>s</sub>		0.785
3		51352.2			617.6 <sub>s</sub>		0.770
4	51969.6	51969.8 <sub>s</sub>	593.0	591.8 <sub>s</sub> <sup>c</sup>			0.754
5	52562.6	52561.6 <sub>s</sub> <sup>c</sup>	561.7	561.1 <sub>s</sub> <sup>c</sup>			0.735 <sup>c</sup>
6	53124.3	53122.8 <sub>s</sub> <sup>c</sup>	534.2	534.0 <sup>c</sup>	0.719	0.719 <sup>c</sup>	
7	53658.5	53656.8 <sup>c</sup>	500.4		0.703	0.702 <sup>c</sup>	
8	54158.9		485.5		0.671		
9	54624.4		428.9		0.651		
10	55053.3		388.2		0.633		
11	55441.5		345.4		0.593		
12	55786.9	55784.59	300.7	300.92	0.554	0.562 <sub>s</sub>	13
13	56087.6	56085.51	255.0	254.96	0.523	0.5247	16.8
14	56342.6	56340.47	208.4	210.07	0.492	0.4836	21.2
15	56551.0	56550.54		168.96	0.431	0.4399	25.7
16		56719.50		132.91		0.395 <sub>s</sub>	34.3
17		56852.41		102.13		0.347	45
18		56954.54		75.64		0.296	152
19		57030.18		52.65		0.258	49
20		57082.83		31.94		0.207	76
21		57114.77				0.159	105

<sup>a</sup>Obtained from the observed origin of the 1-0 band and the observed  $\Delta G'(\frac{1}{2})$ . This is not an extrapolated value as erroneously stated by (12).

<sup>b</sup>From Lochte-Holtgreven and Dicke (13).

<sup>c</sup>From bands with  $v'' = 1$ .

TABLE IV

## TERM VALUES OF THE TRIPLET COMPONENTS IN THE $B^3\Sigma_u^-$ STATE

The term values are given in the form  $F_1 - F_2^{\text{calc}}$ , etc., where  $F_2^{\text{calc}}$  are the calculated  $F_2$  levels, using the constants  $v_0$ ,  $B_y$ , and  $D_y$  given in Table III. All data are in  $\text{cm}^{-1}$ . The values for  $v' = 21$  are contained in Table II.

Whenever the  $P_2$  and  $R_2$  lines are blended with the corresponding  $P_3$  and  $R_3$  lines, the  $F_2$  levels derived from the wave numbers of these blends are given in square brackets [ ]. The  $F_3$  levels derived from these blends, corrected by the amount  $F_3 - F_2^{\text{calc}}$ , as described in the text, are marked by a § sign. Values in parentheses () are interpolated ones.

Extra levels connected with perturbations are given as  $F_1^x$ , etc.

†Values marked by a dagger have a greater uncertainty.

?A question mark indicates that the level is doubtful

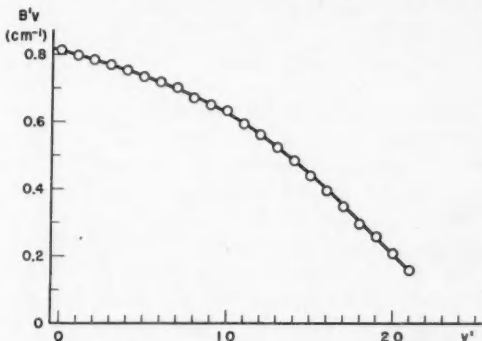
$N'$	$v' = 12$			$v' = 13$			$v' = 14$		
	$F_1 - F_2$ <sup>calc</sup>	$F_2 - F_3$ <sup>calc</sup>	$F_3 - F_2$ <sup>calc</sup>	$F_1 - F_2$ <sup>calc</sup>	$F_2 - F_3$ <sup>calc</sup>	$F_3 - F_2$ <sup>calc</sup>	$F_1 - F_2$ <sup>calc</sup>	$F_2 - F_3$ <sup>calc</sup>	$F_3 - F_2$ <sup>calc</sup>
0	-2.83	—	—	-3.45	—	—	-4.04	—	—
2	-2.56	+0.04†	-1.6†	-3.16	-0.03	-1.69	-3.73	0.00	-1.55
4	-2.56	[+0.04]	-1.84§	-3.25	[+0.10]	-1.85§	-3.82	[+0.14]	-1.72 <sup>b</sup>
6	-2.61	[+0.07]	-1.75§	-3.32	[+0.10]	-1.81 <sup>a</sup>	-3.94	[+0.13]	-1.73§
8	-2.75	[+0.10]	-1.76§	-3.46	[+0.16]	-1.64§	-4.17	[+0.19]	-1.58 <sup>c</sup>
10	-2.91	[+0.15]	-1.62§	-3.63	[+0.22]	-1.60§	-4.43	+0.02 <sup>c</sup>	-1.51 <sup>d</sup>
12	-3.05	[+0.17]	-1.57§	-3.79	+0.02	-1.44	-4.64	0.00	-1.35
14	-3.21	[+0.22]	-1.45§	-3.94	0.00	-1.24	-4.93	-0.03	-1.08
16	-3.34	[+0.30]	-1.27§	-4.18	+0.02	-1.08	-5.28	-0.09	-0.75
18	-3.54	[+0.36]	-1.14§	-4.40	0.00	-0.80	-5.55	-0.08	-0.45
20	-3.76	0.00	-1.05	-4.58	-0.01	-0.56	-5.83	-0.03†	-0.11
22				-4.82	-0.06	-0.37	-6.09	+0.07	+0.16
24				-5.14	+0.06	-0.18	-6.41	+0.16†	+0.61†
26				-5.36	+0.01	+0.17	-6.80	+0.08	+1.07
28							-7.26		
30							-7.90	-0.06	+1.53†
	$a -1.80\%$			$b -1.76\%$			$c [+0.20]$		
	$d -1.55\%$								
$N'$	$v' = 15$			$v' = 16$			$v' = 17$		
	$F_1 - F_2$ <sup>calc</sup>	$F_2 - F_3$ <sup>calc</sup>	$F_3 - F_2$ <sup>calc</sup>	$F_1 - F_2$ <sup>calc</sup>	$F_2 - F_3$ <sup>calc</sup>	$F_3 - F_2$ <sup>calc</sup>	$F_1 - F_2$ <sup>calc</sup>	$F_2 - F_3$ <sup>calc</sup>	$F_3 - F_2$ <sup>calc</sup>
0	-4.98	—	—	-6.57	—	—	-9.02	—	—
2	-4.73	0.00	-1.41	-6.23	0.00	-1.30†	-8.49	0.00	-1.22
4	-4.69	[+0.17]	-1.63 <sup>e</sup>	-6.34	[+0.14]	-1.82§	-8.56	[+0.30]†	-1.85
6	-4.90	[+0.14]	-1.71§	-6.60	[+0.13]	-1.72§	-8.85	[+0.18]	-1.63 <sup>f</sup> <sup>k</sup>
8	-5.22	[+0.26]	-1.44§	-7.08	-0.52 <sup>h</sup>	-1.51†	-9.38	-0.01	-1.30
10	-5.54	[+0.37]†	-1.21 <sup>g</sup>	-7.53	+0.15 <sup>i</sup>	-1.23	-9.90	+0.08†	-0.78
12	-5.93	+0.06	-0.99	-8.08	-0.01	-0.78	-10.45	0.00	-0.10
14	-6.27	0.00	-0.65	-8.59†	-0.02	-0.23	-10.91	+0.08	+0.72
16	-6.73	-0.03	-0.25	-9.16	-0.01	+0.32	-11.35	+0.01	+1.64
18	-7.19	-0.04	+0.15	-9.71	0.00	+0.95			
20	-7.60	-0.02	+0.67	-10.31	+0.02	+1.78			
22	-8.18	+0.03	+1.12	-10.80	+0.14	+2.68			
24	-8.68	(+0.10)	+1.97	-11.30		+2.82 <sup>j</sup>			
26	-9.24	+0.11	+2.08†	-11.73	-0.56	+3.87			
28	-10.00	-0.06	+2.74	-12.21					
30	-10.75	(-0.22)	+2.94	-12.79	-0.37				
32		-0.38	+3.67	-13.47					
34				-14.41					
	$e -1.71\%$			$h F_1^Z - F_2^Z$ <sup>calc</sup> = +0.45†.			$k -1.46†.$		
	$f +0.15†.$			$i F_2^Z - F_3^Z$ <sup>calc</sup> = -1.29.					
	$g -1.18\%.$			$j F_3^Z - F_2^Z$ <sup>calc</sup> = +6.81.					

TABLE IV (Concluded)

N'	v' = 18			v' = 19			v' = 20		
	$F_1 - F_2$ calc			$F_2 - F_3$ calc			$F_1 - F_2$ calc		
	$F_1 - F_2$ calc	$F_2 - F_3$ calc	$F_1 - F_3$ calc	$F_1 - F_2$ calc	$F_2 - F_3$ calc	$F_1 - F_3$ calc	$F_1 - F_2$ calc	$F_2 - F_3$ calc	$F_1 - F_3$ calc
0	-11.87	—	—	-14.80 <sup>†</sup>	—	—	—	—	—
2	-11.45	0.00	-0.97	-14.32	+0.01	-1.02	0.00	-0.86	
4	-11.26	+0.07 <sup>†</sup> <sup>l</sup>	-1.36 <sup>m</sup>	-14.41	0.00 <sup>p</sup>	-1.71 <sup>q</sup>	-0.01	+0.22	
6	-11.11 <sup>n</sup>	+0.01	-1.17	-14.75	[-0.02]	-2.01 <sup>r</sup>	0.00	+0.15	
8	-13.49 <sup>o</sup>	0.00	-0.41	-15.36	+0.05	-2.43 <sup>s</sup>	-0.01 <sup>†</sup>	+0.31	
10	-11.67 <sup>?</sup>	+0.03		-16.01	-0.05	+1.66 <sup>t</sup>	+0.14	+0.69 <sup>†</sup>	
12	-11.27			-16.74	-0.02	+1.52	+0.50 <sup>†</sup>	+1.18	
14				-17.81	+0.01				
16				-18.60					

<sup>l</sup> {+0.34}.  
<sup>m</sup> -1.33<sup>§</sup>.  
<sup>n</sup>  $F_1 - F_2$  calc = -16.23<sup>?</sup>.  
<sup>o</sup>  $F_1 - F_2$  calc = -10.41<sup>†?</sup>.  
<sup>p</sup> {+0.16}.  
<sup>q</sup> -1.69<sup>§</sup>.  
<sup>r</sup> -2.00<sup>§</sup>.  
<sup>s</sup>  $F_2 - F_3$  calc = +3.48<sup>†</sup>.  
<sup>t</sup>  $F_1 - F_3$  calc = -3.30<sup>†</sup>.

included. In Fig. 6, a plot of the  $B_v'$  values against  $v'$  is shown. Instead of presenting the actual term values we give in Table IV, in order to save space, the deviations of the observed term values from the calculated  $F_2$  series, calculated from equation [1] with the final  $B_v$  and  $D_v$  values. The signs attached to some of the numbers of this table are explained in the heading of the table.

FIG. 6.  $B_v'$  curve of the  $B^3\Sigma_u^-$  state of O<sub>2</sub>.

In Fig. 7 the observed energy levels above 56835 cm.<sup>-1</sup> are plotted against  $J$ . This figure gives an idea of the relative magnitude of the vibrational quanta, the rotational energies, and the triplet splittings near the convergence limit. It also shows the perturbations which occur in various places.

### (3) Triplet Splitting

The observed triplet splittings  $F_1 - F_2$  and  $F_3 - F_2$  are readily obtained from Table IV by taking the differences of columns 1 and 2, and 3 and 2, respectively.

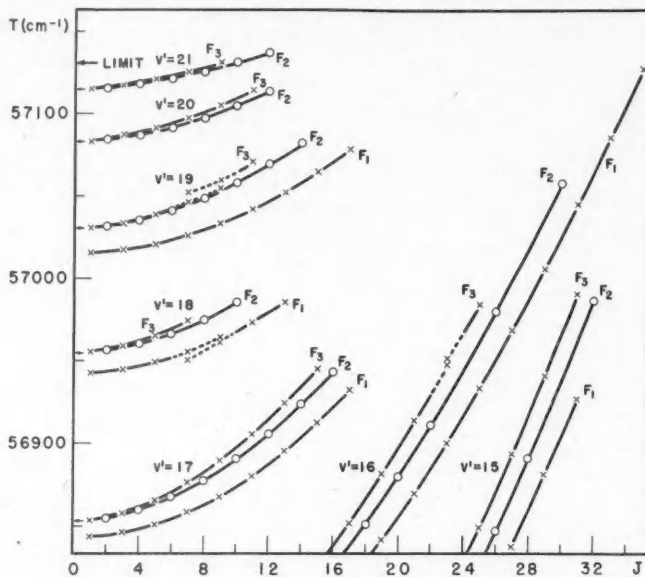


FIG. 7. Observed energy levels of the  $B^3\Sigma_u^-$  state of  $O_2$  close to the convergence limit as a function of  $J$ .

The  $F_2$  components are represented by circles, the  $F_1$  and  $F_3$  components by crosses. Where perturbations and, associated with them, extra levels occur the lines connecting the levels of a given  $v'$  are dashed. The small arrows at  $J = 0$  point to the band origins  $v_0$  (for the  $F_2$  levels); the larger arrow at the top shows the convergence limit (see section D).

A graphical representation of the observed splittings in their dependence on  $N$  is given in Fig. 8 for  $v' = 13, 15, 17, 19$ . It shows the rapid and accelerated increase of the splitting with increasing  $v'$ . The broken line curves give, for comparison, the triplet splitting of the ground state. Extrapolating the splittings of the upper state to smaller  $v'$  values one sees readily that for  $v' \leq 11$  the splittings will be very similar in magnitude to that of the ground state and therefore, since the main branches correspond to  $\Delta J = \Delta N$ , the triplet splitting of the lines in these bands is very small and has not been resolved in spite of the high resolution employed here.

According to Schläpp (18) the three triplet components of a  ${}^3\Sigma$  state, neglecting centrifugal stretching terms, should follow the formulae

$$[3] \quad F_1(N) = B_v N(N+1) + \frac{(2N+3)B_v - \lambda}{-\sqrt{(2N+3)^2 B_v^2 + \lambda^2 - 2\lambda B_v + \gamma(N+1)}},$$

$$[4] \quad F_2(N) = B_v N(N+1),$$

$$[5] \quad F_3(N) = B_v N(N+1) - \frac{(2N-1)B_v - \lambda}{+\sqrt{(2N-1)^2 B_v^2 + \lambda^2 - 2\lambda B_v - \gamma N}},$$

where  $\lambda$  and  $\gamma$  are constants:  $\lambda$  is a measure of the spin-spin interaction of the

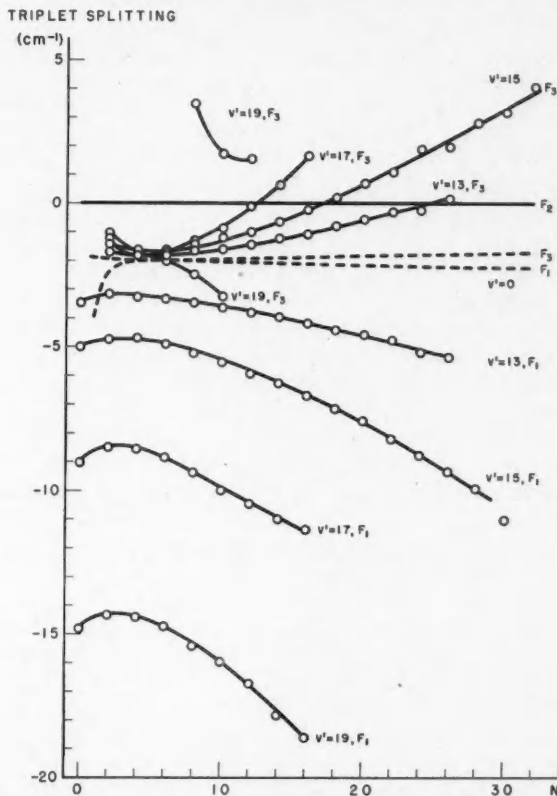


FIG. 8. Triplet splitting in the  $B^3\Sigma_u^-$  state of  $O_2$  as a function of  $N$  for various  $v'$  values. For comparison the triplet splittings in the ground state  $X^3\Sigma_g^-$  ( $v'' = 0$ ) are shown by broken lines. The splittings for  $v' = 12, 14, 16, 18$  have been omitted in order to avoid overcrowding of the diagram. These splittings are entirely similar to, and intermediate between, those shown. A strong perturbation is evident for the  $F_3$  component of the  $v' = 19$  level.

unpaired electrons,  $\gamma$  is a measure of the interaction of the resultant electron spin with the magnetic moment produced by the rotation of the molecule. On the basis of Schlapp's formulae the following sum rule should hold:

$$[6] \quad [F_2(N) - F_1(N)] + [F_2(N + 2) - F_3(N + 2)] = 2\lambda + \gamma,$$

that is, the sum at the left formed from the observed splittings should be independent of  $N$ . This is found to be the case for  $v' = 13, 14, 15$  within the experimental error (compare Fig. 9, see below). For  $v' = 16, 17, 18, 19$  the sums are no longer independent of  $N$ . However, perturbations are present in all these bands and they may well be the only cause for the apparent breakdown of equation [6]. In Table V the average observed values of the sums, i.e., of  $2\lambda + \gamma$ , are listed. For  $v' > 15$  the values given refer to low  $N$  values only; for  $v' = 12$

TABLE V  
SPLITTING CONSTANTS IN THE  $B^3\Sigma_u^-$  STATE

$v'$	12	13	14	15	16	17	18	19	$\text{cm}^{-1}$
$2\lambda + \gamma$	4.5	5.02	5.62	6.48	(8.0 <sub>5</sub> )	(10.2)	(12.8)	(15.8)	

Values in parentheses refer to low  $N$  values only and are very uncertain.

the partially resolved triplet splitting of the 12-0 band has been analyzed under the assumption that the sum rule is valid. In spite of these limitations the table shows clearly the rapid and smooth increase of  $2\lambda + \gamma$  near the convergence limit, very similar to that found for the  $A^3\Sigma_u^+$  state (11). Considerable effort was spent to find assignments for the components  $F_1$  of the 20-0 and 21-0 bands and thus determine  $2\lambda + \gamma$  for the  $v' = 20$  and 21 levels. These  $F_1$  levels are certainly present near the energies expected by extrapolation. However, owing to the presence of strong perturbations no definite assignments could be made.

A further test of the validity of Schlapp's formulae in the present case is obtained by ascertaining whether they represent the observed variation of the splitting with  $N$ . From equations [3], [4], and [5], it follows immediately that

$$[7] \quad F_2(N) - F_1(N) - \frac{1}{2}(2\lambda + \gamma) = F_3(N+2) - F_2(N+2) + \frac{1}{2}(2\lambda + \gamma) \\ = -(2N+3)B_v + \sqrt{(2N+3)^2B_v^2 + \lambda^2 - 2\lambda B_v} - \gamma(N + \frac{3}{2}),$$

that is both  $F_2 - F_1$  and  $F_3 - F_2$  follow the same course if properly combined with  $\frac{1}{2}(2\lambda + \gamma)$ . In Fig. 9 the observed values of the left-hand side of [7] for the  $v' = 15$  level with  $(2\lambda + \gamma) = 6.48 \text{ cm}^{-1}$  are plotted against  $N$ . The validity of the sum rule is equivalent to the fact that the points for  $F_1$  and  $F_3$  follow the same curve. Since the quantity  $2\lambda + \gamma$  has already been determined and used (left-hand side of [7]) only one parameter is left to fit the observed points. The three broken line curves of Fig. 9 represent the right-hand side of equation [7] with  $\gamma = 0$ ,  $\lambda = 3.24$ ;  $\gamma = -0.18$ ,  $\lambda = 3.33$ ; and  $\gamma = 0.23$ ,  $\lambda = 3.35 \text{ cm}^{-1}$  (i.e., in each case,  $2\lambda + \gamma = 6.48$ ). It is evident that the general character of the observed splittings can be represented by [7] with  $\gamma \approx -0.18 \text{ cm}^{-1}$ , but no quantitative agreement can be brought about by varying  $\gamma$  and  $\lambda$  while keeping  $2\lambda + \gamma$  at  $6.48 \text{ cm}^{-1}$ . Similar discrepancies even though somewhat smaller are found for  $v' = 14$  and 13. Because of the perturbations no attempt was made to carry out similar comparisons for  $v' > 15$ .

Schlapp's formulae have been found to hold within the accuracy of optical measurements for the  $X^3\Sigma_g^-$  ground state (2) and the  $A^3\Sigma_u^+$  state (11) of  $\text{O}_2$ . With the very high accuracy possible in the microwave region a slight deviation has been detected for the ground state by Gordy and his collaborators (3). Several attempts (14, 15) have been reported recently to improve the formulae in order to obtain an accurate representation of the microwave data. The modification of Schlapp's formulae published by Miller and Townes (14) gives a slightly better fit for our data than the Schlapp formula (Fig. 9), but none of the formulae available at present gives a satisfactory agreement. This failure

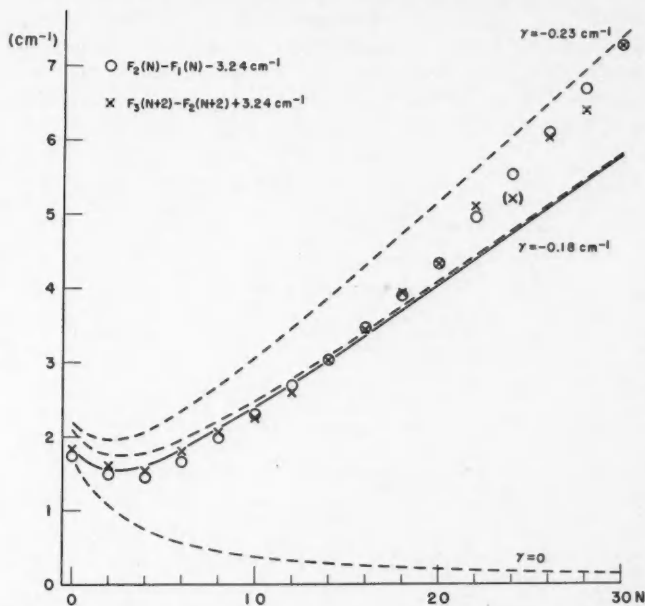


FIG. 9. Test of Schlapp's formulae for the triplet splitting in the  $v' = 15$  level of the  $B^3\Sigma_g^-$  state of  $O_2$ . The observed values of the left-hand side of equation [7] have been plotted as circles ( $F_1$ ) and crosses ( $F_3$ ). The three broken lines correspond to Schlapp's formulae for various values of  $\gamma$ . The full line has been calculated with Schlapp's formulae as modified by Miller and Townes ( $\gamma = -0.18 \text{ cm}^{-1}$ ). The experimental value  $2\lambda + \gamma = 6.48 \text{ cm}^{-1}$  has been used for all curves.

is probably connected with the fact that the coupling parameter  $\gamma$  is very large in the present case, of the order of  $-0.18 \text{ cm}^{-1}$  for  $v' = 15$  of  $B^3\Sigma_g^-$  as compared with only  $-0.00837 \text{ cm}^{-1}$  for  $v'' = 0$  of  $X^3\Sigma_g^-$  and with  $-\gamma \leq 0.016$  for  $A^3\Sigma_u^+$ . With the theoretical discussions still in progress we have not attempted to represent our data by empirical relations, e.g., by adding in Schlapp's formulae correction terms to  $\gamma$  which are proportional to  $N^2$ .

#### D. VIBRATIONAL ANALYSIS AND DISSOCIATION ENERGY

##### (1) Convergence Limit

By the rotational analysis described in the preceding section, six new vibrational levels, with  $v' = 16, 17, \dots, 21$ , have been established beyond those previously known. The last four of these,  $v' = 18, 19, 20, 21$ , are higher than the convergence limit that has until now been generally accepted.<sup>2</sup>

<sup>2</sup>Watanabe, Inn, and Zelikoff (20) have recently measured the absorption coefficients of oxygen in the Schumann region under low resolution. They noticed already that the discrete absorption extended beyond the previously accepted dissociation limit. However, the feature at  $57140 \pm 60 \text{ cm}^{-1}$  is probably not the 20-0 band as they believed since, as may be noted from Fig. 4, none of the heads of the last four bands are conspicuous and there are much stronger accidental groups of lines which will give rise to peaks at low resolution.

In Table III the band origins  $\nu_0$  of all the absorption bands with  $\nu'' = 0$  are given including the older measurements of Knauss and Ballard (12) and Curry and Herzberg (4). The fourth and fifth columns give the vibrational quanta  $\Delta G'(\nu + \frac{1}{2})$  derived from them. These as well as the second differences  $\Delta^2 G'$  are plotted in Fig. 10.

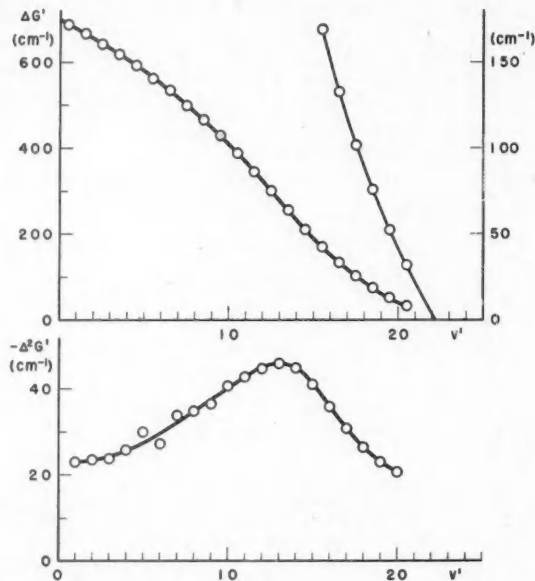


FIG. 10.  $\Delta G'$  and  $\Delta^2 G'$  curves for the  $B^3\Sigma^-$  state of  $O_2$ .

The observed  $\Delta G'(\nu + \frac{1}{2})$  values are plotted with the abscissae  $\nu' + \frac{1}{2}$ , the negative values of  $\Delta^2 G'(\nu) = \Delta G'(\nu + \frac{1}{2}) - \Delta G'(\nu - \frac{1}{2})$  with the abscissae  $\nu'$ . A magnified portion of the  $\Delta G'$  curve with the most probable extrapolation is shown by the light line in the upper part of the diagram (ordinate scale at right).

Since the last vibrational quantum is as small as  $32 \text{ cm}^{-1}$  and the last  $\Delta^2 G'$  values follow accurately a smooth curve (Fig. 10), only a very short extrapolation is necessary to obtain the convergence limit. For this purpose the maximum of the extrapolated  $G(\nu')$  curve was determined where  $G$ , as usual, denotes the total vibrational energy. The continuous function  $G(\nu')$  which we used was a polynomial of degree  $m$  exactly representing the last  $m + 1$  vibrational levels ( $\nu' = 21, 20, 19, \dots, 21 - m$ ). In order to obtain the coefficients of the polynomial a difference table  $\Delta G, \Delta^2 G, \dots, \Delta^m G$  was constructed and extended to higher  $\nu'$  values by keeping constant the last value in the  $\Delta^m G$  column. The maximum of  $G(\nu')$  and the corresponding  $\nu'_{\max}$  were found by interpolation. Table VI shows the results for various values of  $m > 1$  and, at the same time, gives corresponding extrapolations for the upper state ( $A^3\Sigma^+$ ) of the near ultraviolet bands using the recent measurements by one of us (11). In both electronic states these extrapolations indicate the existence of one additional

TABLE VI

CONVERGENCE LIMITS OF THE  $B^3\Sigma_u^-$  AND  $A^3\Sigma_u^+$  STATES EXTRAPOLATED BY USING POLYNOMIALS OF VARIOUS DEGREES  $m$ 

	Last observed level		Extrapolation				
	$v'$	$\nu_0$ (cm <sup>-1</sup> )	$m$	$v'_{\max}$	Last $\Delta G'$ (cm <sup>-1</sup> )	$\delta G$ (cm <sup>-1</sup> )	Limit (cm <sup>-1</sup> )
$B^3\Sigma_u^-$	21	57114.77	2	22.04	11.23	0.02	57126.0
			3	22.32	13.51	0.80	129.1
			4	22.19	12.89	0.35	128.0
			5	22.07	11.86	0.06	126.7
			6	22.17	12.48	0.25	127.5
$A^3\Sigma_u^+$	10	41153.94	2	11.80	131.2	31.3	41316.4
			3	11.29	111.0	6.4	271.3
			4	11.19	105.3	3.0	262.2
			5	11.16	103.6	2.2	259.7
			6	11.15	103.0	2.0	258.9

vibrational level. The "last  $\Delta G'$ " and the difference  $\delta G$  between the extrapolated limit and the extrapolated last level have been listed separately in Table VI.

As long as a smooth extrapolation is assumed to be reasonable at all, the approximation should become better with increasing degree  $m$  of the polynomial. However the influence of the experimental errors of the input data on the differences  $\Delta^m G$  also increases with  $m$ . For this reason from  $m = 6$  on these differences show an irregular variation rather than a definite trend with  $v'$  for both the  $A^3\Sigma_u^+$  and  $B^3\Sigma_u^-$  states. The extrapolations with  $m = 6$  were, therefore, made with a linear (least squares) representation of the  $\Delta^6 G$  values. The limits so obtained are considered to be the most reliable ones of those given in Table VI. The tail of the  $\Delta G'(v' + \frac{1}{2})$  curve of the  $B^3\Sigma_u^-$  state in Fig. 10 is drawn according to the best numerical extrapolation just discussed.

With increasing  $m$  the extrapolated limits of Table VI appear to approach a value which in the case of the  $B^3\Sigma_u^-$  state may be given to  $\pm 1$  cm<sup>-1</sup>. This does not take account of the possible errors of the band origins ( $\pm 0.10$  cm<sup>-1</sup>) which have not been smoothed in the above-described extrapolation method and which may lead to a cumulative error of certainly less than  $\pm 4$  cm<sup>-1</sup>. We, therefore, conclude that the extrapolated convergence limit of the Schumann-Runge absorption bands can be safely given as  $57127.5 \pm 5$  cm<sup>-1</sup>.

According to the extrapolation of the  $B^3\Sigma_u^-$  state the  $v' = 22$  level is just below the limit and may have a few stable rotational levels. The origin  $\nu_0$  of the 22-0 band ( $F_2$  component) is predicted at about 57127 cm<sup>-1</sup>. There is indeed at the very end of the discrete absorption spectrum near 57129.5 cm<sup>-1</sup> a group of three absorption lines (see Table 1b and Fig. 4). Since all bands are strongly degraded to the red, these lines must be assigned to a vibrational quantum number  $v' > 21$ . Assuming that no further lines are hidden by the adjoining continuum the lines of highest wave number must necessarily arise from combinations with  $N'' = 1$  of the ground state. Combinations of the same levels with  $N'' = 3$  should then lie to the red by about 14 cm<sup>-1</sup> (see Fig. 5). A gap of just this

magnitude actually exists between the last three lines and the next group at longer wave lengths. Furthermore, the lines at  $57130.73 \text{ cm}^{-1}$  and  $57128.65 \text{ cm}^{-1}$  show a separation of  $2.08 \text{ cm}^{-1}$  which agrees exactly with the difference between the  $N'' = 1, J'' = 0$  and  $N'' = 1, J'' = 2$  levels of the ground state. If this agreement is real, it would fix the higher one of the two levels with  $J' = 1$ , that is,  $F_1(0)$  or  $F_3(2)$  at  $57129.64 \text{ cm}^{-1}$ . The line intensities favor the  $F_1$  assignment. A  $P$  and an  $R$  branch can be picked out including all three lines mentioned. These branches can be followed up to  $N = 7$ , and they are designated  ${}^nP_i$  and  ${}^nR_i$  in Table 1b (or  ${}^nPX_u$  and  ${}^nRX_u$  for the satellite branches) since neither their assignment to a specific vibrational quantum number nor to a specific triplet component is definitely established with the present data.

Irrespective of the detailed identification of the lines of shortest wave length, it can be seen from Fig. 5 that an upper limit for the energy ( $\nu_0$ ) of the  $F_2$  component of the highest stable vibrational level can be obtained by adding  $1 \text{ cm}^{-1}$  ( $= F_1''(1) - F_2''(0)$ ) to the wave number of the last discrete line. Hence, assuming again that no absorption line has been missed, the last vibrational level must lie below  $57131.7 \text{ cm}^{-1}$ , that is, the last vibrational quantum  $\Delta G'$  must be less than  $16.9 \text{ cm}^{-1}$ . The energy difference between the convergence limit and the last vibrational level must be less than the last vibrational quantum and therefore an upper limit of  $57148 \text{ cm}^{-1}$  can be given for the dissociation limit. This upper limit is independent of any extrapolation.

## (2) Dissociation Energy

The extrapolated convergence limits (see Table VI,  $m = 6$ ) for the  $A^3\Sigma_u^+$  state and the  $B^3\Sigma_u^-$  state differ by  $15868.6 \text{ cm}^{-1}$ . This difference agrees surprisingly well with the term difference  ${}^1D_2 - {}^3P_2$  in atomic oxygen which is  $15867.7 \text{ cm}^{-1}$  (16). Thus there can be no doubt that the convergence limits under discussion represent real dissociation limits (see also below) and that upon dissociation the states of the resulting atoms are  ${}^3P_2 + {}^3P_i$  for the  $A^3\Sigma_u^+$  state and  ${}^1D_2 + {}^3P_i$  for the  $B^3\Sigma_u^-$  state, with  ${}^3P_i$  the same for both states (the closest alternatives  ${}^3P_2 + {}^3P_1$  and  ${}^1D_2 + {}^3P_0$ , or  ${}^3P_2 + {}^3P_0$  and  ${}^1D_2 + {}^3P_1$ , give an energy difference that deviates from the observed by  $\pm 68 \text{ cm}^{-1}$  respectively). According to the non-crossing rule (see the discussion by Herzberg (11))  ${}^3P_i$  can only be  ${}^3P_2$ . We shall from now on make this assumption. The dissociation energy  $D_0^0$  of the oxygen molecule into normal ( ${}^3P_2$ ) atoms is then directly given by the dissociation limit of the  $A^3\Sigma_u^+$  state or by the dissociation limit of the  $B^3\Sigma_u^-$  state less  $15867.7 \text{ cm}^{-1}$ .

In Table VII the various data concerning  $D_0^0$  are summarized. The first three lines give the following information derived from the  $A^3\Sigma_u^+$  state (11):

(a) The last observed vibrational level at zero rotation gives a lower limit for  $D_0^0$ .

(b) The extrapolated convergence limit (Table VI) gives the dissociation energy directly.

(c) There is evidence for predissociation by rotation in the  $v' = 10, N' = 17$  level and therefore an energy between that of the  $N' = 15$  and  $N' = 17$  levels must be an upper limit to the dissociation energy.

TABLE VII  
DATA REFERRING TO THE DISSOCIATION ENERGY OF THE O<sub>2</sub> MOLECULE

	Obtained from	Dissociation limit (cm <sup>-1</sup> )	
		<sup>2</sup> P <sub>2</sub> + <sup>1</sup> D <sub>2</sub>	<sup>3</sup> P <sub>2</sub> + <sup>1</sup> P <sub>2</sub>
(a)	$A^3\Sigma_u^+$ $v' = 10, N' = 0$		$> 41153$
(b)	Extrapolation		$\approx 41259$
(c)	Predisociation ( $v' = 10, N' = 16$ )		$< 41284$
(d)	$B^3\Sigma_u^-$ $v' = 21, N' = 0$	$> 57114.8$	$> 41247$
(e)	Highest level with $J' = 1$	$\geq 57129.6$	$\geq 41262$
(f)	Extrapolation	$57127.5 \pm 5$	$41260 \pm 5$
(g)	Last line and last $\Delta G'$	$< 57148$	$< 41280$

Accepted value:  $41260 \pm 5$  cm<sup>-1</sup>

The following data arise from the present investigation of the  $B^3\Sigma_u^-$  state:

(d) The energy of the well-established  $v' = 21$  level at zero rotation must be lower than the dissociation limit.

(e) The energy of the highest rotational level with  $J' = 1$  as obtained above from the lines of shortest wave length represents a closer lower limit than (d). Conceivably it might even be very slightly above the limit if the possibility of a rotational potential maximum is considered.

(f) The extrapolated convergence limit (Table VI), because of the short distance of extrapolation, may be expected to agree with the true dissociation limit within the inaccuracy of the extrapolation.

(g) An upper limit for the dissociation limit was derived in subsection (1) from the observed line of shortest wave length.

No evidence of predisociation by rotation was found in the Schumann-Runge bands. This is probably due to the presence of perturbations which made it impossible to predict the accurate positions of the high rotational levels for which such a predisociation could be expected.

The data in the last column of Table VII (obtained for  $B^3\Sigma_u^-$  by subtracting 15867.7 cm<sup>-1</sup> from those in the second last column) support each other very well, and they provide narrow limits for  $D_0^0$ . However, the limits (a), (b), (d), (e), (f) are based upon the assumption that the potential curves of the two electronic states  $A^3\Sigma_u^+$  and  $B^3\Sigma_u^-$  have no potential maxima. If there were potential maxima the extrapolations (b) and (f) would merely give upper limits while the data (a), (d), (e) would no longer give lower limits.

It cannot be proved conclusively that there are no potential maxima present. However, the excellent agreement of the limits obtained from the  $A^3\Sigma_u^+$  and the  $B^3\Sigma_u^-$  states can only be understood if either both states have no potential maxima or both states have potential maxima of the same height. It is difficult to believe that the latter coincidence would occur, particularly since the  $\Delta G$  curves and, therefore, the potential curves of the two states are quite different (compare our Fig. 10 with Fig. 8 of Reference 11). In addition it appears that for both states the  $B_e'$  values extrapolate to zero at the convergence limits rather than to some finite value as would be the case if potential maxima existed.

This may be seen from a plot (not shown) of  $(B_{v'})^n$  versus  $G(v')$  where  $n$  is chosen in such a way that a straight line results ( $n = 7$  for the  $A^3\Sigma_u^+$  state,  $n = 4$  for the highest vibrational levels of the  $B^3\Sigma_u^-$  state).

The preceding arguments do not exclude potential maxima that are only a few  $\text{cm}^{-1}$  high. In order to take into account this uncertainty we shall assign a conservative error to our result. As the final value we shall adopt for the dissociation energy of  $\text{O}_2$  (referred to  $N'' = 0, J'' = 0$ ; see section C(2)):

$$D_0^0(\text{O}_2) = 41260 \pm 15 \text{ cm}^{-1}.$$

This value does not depend on any extrapolation since the limit of error given includes a lower limit and almost includes a (conservative) upper limit. Using the conversion factors of DuMond and Cohen (5) the above value corresponds to  $5.114_8 \pm 0.002$  ev. and  $117.96 \pm 0.04$  kcal./mole<sub>chem</sub> (or with the older conversion factors used by Herzberg (10),  $5.113_8$  ev. and  $117.94$  kcal./mole).

The change in  $D(\text{O}_2)$  affects of course all those dissociation energies which have been determined from thermochemical data involving oxygen. A particularly important one is the heat of dissociation of NO. One finds from the above  $D(\text{O}_2)$  value, the dissociation energy of  $\text{N}_2$  (Gaydon (7), Douglas (4a)) and the heat of formation of NO at  $0^\circ\text{K}$ . (Rossini (19))

$$D_0^0(\text{NO}) = 52477 \pm 50 \text{ cm}^{-1}$$

or, again using DuMond and Cohen's conversion factors,  $D_0^0(\text{NO}) = 6.505_2$  ev. =  $150.0_3$  kcal./mole.

*Note added in proof:* Recently DuMond and Cohen (5a) have published a revised adjustment of atomic constants. Using the corresponding conversion factors increases the above values in ev. and kcal. by approximately 1 part in 10,000.

#### E. CONCLUSION

The old value of the dissociation energy of  $\text{O}_2$  was between 40990 and 41009  $\text{cm}^{-1}$  depending on the extrapolation chosen. This extrapolation was considered to be accurate within the stated limits and in fact this case has often been quoted to illustrate safe and precise spectroscopic methods of determining dissociation energies. The new value for  $D_0^0(\text{O}_2)$  is higher by  $260 \text{ cm}^{-1}$ . While this is not a large amount it is far outside the error considered possible previously. The discrepancy is of course due to the fact that the inflection of the  $\Delta G'$  curve and the "toe" of positive curvature (see Fig. 10) could not be detected as long as the vibrational levels were known only to  $v' = 15$ . This example again emphasizes the need for caution in stating the results of such extrapolations.

Like the old value the new  $D_0^0(\text{O}_2)$  value is based on the assumptions (a) that on dissociation at the limit of the  $B^3\Sigma_u^-$  state one O atom is in the  ${}^3P_2$  state (rather than  ${}^3P_1$  or  ${}^3P_0$ ) and (b) that no potential maximum occurs. The first assumption is in agreement with the non-crossing rule while any alternative assumption would contradict it. Arguments against the second assumption have been presented above. We therefore feel that the value for  $D_0^0(\text{O}_2)$  here derived must be considered as definitive.

The analysis of the Schumann-Runge bands at the very end of the discrete absorption is still incomplete and a number of lines remain unclassified. As mentioned before our failure to assign these lines is due to the presence of perturbations. Incidentally, the perturbations establish the presence of another stable electronic state presumably going to the same limit (<sup>3</sup>P<sub>2</sub> + <sup>1</sup>D<sub>2</sub>) as B<sup>3</sup>Σ<sub>u</sub><sup>-</sup>. However, with only a few "extra" levels available, no identification of the new electronic state is possible at present.

#### ACKNOWLEDGMENT

We are greatly indebted to Mr. J. Shoosmith for his expert work in building and putting into operation the vacuum spectrograph and for his efficient help in obtaining the spectrograms on which this paper is based.

#### REFERENCES

1. ANDERSON, R. S., JOHNSON, C. M., and GORDY, W. Phys. Rev. 83: 1060. 1951.
2. BABCOCK, H. D. and HERZBERG, L. Astrophys. J. 108: 167. 1948.
3. BURKHALTER, J. H., ANDERSON, R. S., SMITH, W. V., and GORDY, W. Phys. Rev. 79: 651. 1950.
4. CURRY, J. and HERZBERG, G. Ann. Physik, 19: 800. 1934.
- 4a. DOUGLAS, A. E. Can. J. Phys. 30: 302. 1952.
5. DUMOND, J. W. M. and COHEN, E. R. Phys. Rev. 82: 555. 1951.
- 5a. DUMOND, J. W. M. and COHEN, E. R. Revs. Mod. Phys. 25: 691. 1953.
6. EDELEN, B. J. Opt. Soc. 43: 339. 1953.
7. GAYDON, A. G. Dissociation energies. Chapman and Hall, Ltd., London. 1947. 2nd ed. 1953.
8. HARRISON, G. R. M.I.T. Wavelength Tables. John Wiley & Sons, Inc., New York. 1939.
9. HERZBERG, G. Z. physik. Chem. B, 4: 223. 1929.
10. HERZBERG, G. Molecular spectra and molecular structure. I. Spectra of diatomic molecules. D. Van Nostrand Company, Inc., New York. 1950.
11. HERZBERG, G. Can. J. Phys. 30: 185. 1952.
12. KNAUSS, H. P. and BALLARD, S. S. Phys. Rev. 48: 796. 1935.
13. LOCHTE-HOLTGREVEN, W. and DIEKE, G. H. Ann. Physik, 3: 937. 1929.
14. MILLER, S. L. and TOWNES, C. H. Phys. Rev. 90: 537. 1953.
15. MIZUSHIMA, M. Private communication. 1953.
16. MOORE, C. E. Atomic energy levels. Vol. I. National Bureau of Standards, Washington. 1949.
17. MULLIKEN, R. S. Phys. Rev. 32: 186. 1928.
18. SCHLAPP, R. Phys. Rev. 51: 342. 1937.
19. ROSSINI, F. D. Selected values of chemical thermodynamic properties. Natl. Bur. of Standards, Washington. 1949.
20. WATANABE, K., INN, E. C. Y., and ZELIKOFF, M. J. Chem. Phys. 21: 1026. 1953.

## PHOTONEUTRONS IN A HEAVY WATER PILE<sup>1</sup>

BY M. W. JOHNS<sup>2</sup> AND B. W. SARGENT<sup>3</sup>

### ABSTRACT

Decay curves of the neutron intensity in the low power heavy water pile (ZEEP) at Chalk River as a function of time from shutdown with cadmium rods were obtained with three proportional counters of different sensitivities. The range of counting rates spanned, including operation at 50 w., was  $8 \times 10^6$ . The durations of steady operation before shutdown were 10, 50, and 230 min. The mean lifetimes and absolute yields of delayed and photoneutron groups were found by analyzing each decay curve into a sum of decreasing exponentials and using the theory of pile kinetics. The yields were corrected to infinite irradiation time. These results are compared with data obtained by others. The comparison shows that the energetic  $\gamma$ -rays of fission products which produce photoneutrons in the heavy water are absorbed to the extent of about 26% in the heavy water and 74% in the uranium rods. A table of recommended mean lifetimes and absolute yields of delayed and photoneutrons is given for use in the kinetics of heavy water piles such as ZEEP. Some quantitative data on the effects of the control plates and shutoff rods are included.

### INTRODUCTION

The threshold for the photodisintegration of the deuteron occurs at 2.230 Mev. (2). During steady operation of a heavy water pile, photoneutrons are produced by the prompt  $\gamma$ -rays of fission, by the  $\gamma$ -rays from the radiative capture of neutrons in the various materials in the pile, and by the  $\gamma$ -rays from the accumulated fission products if the energies of the  $\gamma$ -rays are above this threshold. The last-mentioned source depends on the previous history of the pile. On the whole, these contributions are small in comparison with the neutrons from fission. However, after shutdown the neutron intensity decreases with time in a complicated manner owing to the delayed neutrons from fission and the photoneutrons. These sources of neutrons are then dominant in the pile behavior. Information on the delayed and photoneutrons is therefore of practical interest.

The delayed neutrons are evaporated by certain fission fragments after they have undergone  $\beta$ -decay. The intensities and periods have been thoroughly studied with the aid of cyclotrons and later of graphite piles (4, 14, 19, 22). We shall adopt the results given in a paper by Hughes, Dabbs, Cahn, and Hall (14).

The photoneutrons produced by the energetic  $\gamma$ -rays of fission products should possess the half-periods of these products, which may amount to minutes, hours, etc. In 1944 Elliott (5) showed that 75-day and 10-day old irradiated uranium produced photoneutrons in heavy water. The  $\gamma$ -emitting fission product was identified as  $\text{La}^{140}$  by chemistry and the half-period of the parent—300 hr.  $\text{Ba}^{140}$ . The neutron yield was measured in these experiments with the integration apparatus described by Elliott, Hincks, and May (7). Later, Elliott (6) showed directly with a  $\beta$ -ray spectrometer that  $\text{La}^{140}$  emits about 0.05 quanta of energy

<sup>1</sup> Manuscript received October 5, 1953.  
Contribution from the Physics Division, Atomic Energy of Canada, Limited, Chalk River, Ont. Issued as A.E.C.L. No. 90.

<sup>2</sup> This work was reported at the Vancouver Meeting (June, 1948) of the Royal Society of Canada.

<sup>3</sup> Present Address: Department of Physics, McMaster University, Hamilton, Ont.

<sup>3</sup> Present Address: Department of Physics, Queen's University, Kingston, Ont.

2.55 Mev. per disintegration. The cross section for the photodisintegration of deuterium at 2.55 Mev. was found to be  $(1.4 \pm 0.1) 10^{-28}$  cm.<sup>2</sup> per deuterium atom. It is not practicable to isolate short-period fission products and make similar studies of photoneutron yields.

A decay curve for the photoneutron intensity in the Argonne heavy water pile after shutdown was analyzed by May (17). The mean lifetimes reported were 17.3, 78, and 238 min. Fenning (8) measured the photoneutron intensity in ZEEP with a boron trifluoride chamber from 30 min. to 24 hr. after shutdown of a 225-min. operation at 50 watts. The derived mean lifetimes were 30, 128, and 275 min. Hincks (13) has examined these decay curves and found that the disagreement can be removed if certain justifiable changes (allowances for long period background and counting losses) are made. The mean lifetimes obtained by Fenning are then supported by the work at the Argonne Laboratory.

The purpose of the experiments described in this paper was to make careful measurements of the intensities and mean lifetimes of some of the photoneutron groups, especially those that just escape being masked by the delayed neutrons. It was realized that the photoneutron groups might be numerous and that an analysis of a composite decay curve might be empirical only. The experiments were carried out on ZEEP in December 1946 and January 1947. Shortly afterwards, similar work was reported by Bernstein, Preston, Wolfe, and Slattery (3) and by Spatz, Hughes, and Cahn (24). The results of the three experiments will be discussed together in a later section.

#### DETAILS OF ZEEP CONSTRUCTION

The ZEEP (Zero Energy Experimental Pile) was designed and built at Chalk River in 1945 by a group\* headed by L. Kowarski. Since only an incomplete account of its construction has been given (21), further details are given in the present paper.

The aluminum tank that holds the heavy water is cylindrical in shape, has a "dished" bottom, and a flange at the top from which it is suspended. The thickness of the tank wall is  $\frac{1}{8}$  in. and of the bottom  $\frac{1}{4}$  in. The outside diameter is 6 ft.  $9\frac{1}{4}$  in., and the radius of curvature of the bottom is 13 ft. 6 in. The length of the cylinder to the joint with the dished bottom is 8 ft.  $5\frac{1}{4}$  in., and the over-all length is 8 ft.  $11\frac{3}{8}$  in.

The uranium metal is in the form of slugs, 1.285 in. in diameter and 6 in. long. These are jacketed in aluminum "stockings" of inside diameter  $1.295 \pm 0.005$  in., wall thickness  $0.040 \pm 0.003$  in., and length 9 ft.  $6\frac{3}{4}$  in. Each "stocking" contains nine slugs. A total of 148 rods, made up in this way, form the lattice, which is square with a spacing of 6 in. between rod centers. The rods hang vertically by a gimbal arrangement, supported by the steel beams that bridge the top of the tank. The lower ends of the rods lie in the horizontal plane containing the joint of the cylindrical tank with the dished bottom.

The graphite reflector is  $2\frac{1}{2}$  ft. thick under the tank and 3 ft. thick around it. The latter portion extends upwards to within about 1 ft. of the top. There are

\*L. Kowarski, C. W. Gilbert, C. N. Watson-Munro, G. J. Klein, E. P. Hincks, F. W. Fenning, A. H. Allan, G. Ferguson, and D. B. Nasser.

two horizontal tangential channels through the graphite. The control plates are cadmium-plated steel sheets, suspended by wires in the annular gap, about  $1\frac{1}{2}$  in. wide, between the tank and the graphite. The plates are curved to conform to the curvature of the tank, and are spaced around the tank at approximately  $90^\circ$ -intervals. Three are linked to move up and down together and to provide the coarse control, while the fourth can be moved independently and provides the fine control. The dimensions of the coarse control plates are 20 in.  $\times$  12 in., and those of the fine control plate 20 in.  $\times$   $4\frac{1}{2}$  in. The two sets of plates are moved by manually turning handwheels at the main control board, while selsyns indicate their positions.

The shutoff rods are cadmium-plated steel tubes completely enclosed between aluminum tubes, and are suspended on wires inside and near the axis of the tank. The approximate length of the shutoff rods is 1 ft. These are arranged in two rows (A + B) of four each, spaced 8 in. apart within the row, while the two rows are also 8 in. apart. The rods can be raised or lowered manually by handwheels at the control board, and are normally in the "up" position when the pile is operating and in the "down" position when the pile is shut down. Intermediate positions are not used. Either set can be released to descend under gravity into the heavy water in about one second, either by push button or by a "trip" of the amplifier attached to an ionization chamber.

In order to introduce neutron detectors, etc. into the tank for activation, a central aluminum "thimble",  $2\frac{1}{4}$  in. O.D. and 2.17 in. I.D., and 21 aluminum "thimbles", 1 in. O.D. and wall 0.022 in. thick, are provided. These are spaced at 6 in. intervals along two diameters at right angles, and pass through the mid-points of lattice cells. These tubes are usually filled with heavy water of inferior purity. The heavy water in the tank is 99.76 atom % D.

#### EXPERIMENTAL DETAILS

##### (a) *Neutron Counting and Recording Equipment*

It was desired to measure the neutron intensity in ZEEP during steady operation at as high a power as permitted by the radiation hazard, and after shutdown (with all cadmium rods) over a duration of hours. The operating power level was chosen to be 50 watts, as indicated by one of the ion chambers. Since the neutron flux at 50 w. was of the order of  $8 \times 10^6$  times the flux after a long shutdown, three neutron counters of very different sensitivities were arranged at suitably chosen points in the pile to follow the flux changes occurring in these experiments. To obtain the flux as a function of time over the periods of operation and shutdown, an intercalibration of the relative sensitivities of the three counters in their chosen positions was carried out and all counting rates (i.e. relative neutron fluxes) were expressed in terms of that of the most sensitive neutron counter.

The counters used were designed and built by B. H. Flowers (9) and N. Veall for the measurement of slow neutron fluxes in a pile. The construction of a counter is shown in Fig. 1. All the counters had the same physical dimensions, and were operated in the proportional region with a positive potential of above 1400 volts on the central wire. Further details are given in Table I.

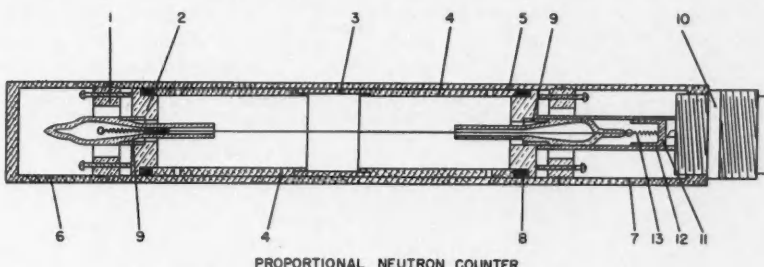


FIG. 1. Neutron counter.

Over-all dimensions: length 7-3/8 in., diameter 1 in. Parts are of aluminum, with the exception of the end plugs and screws 2, which are of brass. 1—Threaded ring for applying pressure to rubber gaskets; 2—end plugs; 3—section of inner sleeve for clamping platinum strip supporting uranium or boron; 4—sections of inner sleeve; 5—outer tube; 6 and 7—end caps; 8—rubber gasket; 9—Koyar seals; 10—Amphenol plug; 11—brass contact plug; 12—glass sleeve; 13—piano wire spring. The central wire is 8 mil tungsten.

TABLE I  
NEUTRON COUNTERS

Lab. No.	Neutron detector	Gas filling	Operating voltage (v.)
C 12	0.14 mgm. U	15 cm. CH <sub>4</sub> 5 cm. A	1320
C 8	1 mgm. U enriched in U <sup>235</sup>	15 cm. CH <sub>4</sub> 5 cm. A	1560
C 2	B-coating	7.5 cm. CH <sub>4</sub> 2.5 cm. A	1320

The least sensitive counter (No. C 12), containing a foil of natural uranium and operating as a fission counter, was located in the central thimble of ZEEP somewhat below the position of maximum flux. It was used during the period of operation at 50 w. and for about two minutes after shutdown, at which time the counting rate became too low to yield significant data. A similar counter (No. C 8), containing a foil of uranium enriched in U<sup>235</sup>, was placed about two feet above the natural uranium counter. It was used chiefly during the first 15 min. after shutdown. The most sensitive counter (No. C 2), containing a boron coating as neutron detector, was placed in one of the tangential channels in the graphite reflector about one foot from the wall of the tank. At this point the neutron flux was roughly one-fifth of that in the central thimble. This counter provided a record of neutron flux from four minutes after shutdown to the end of each run.

The electronic equipment was as shown in the block diagram, Fig. 2. This equipment was duplicated to allow any two of the three counters to be operated simultaneously. The voltage characteristics and bias curves of the counters were essentially the same as those obtained by Flowers (9).

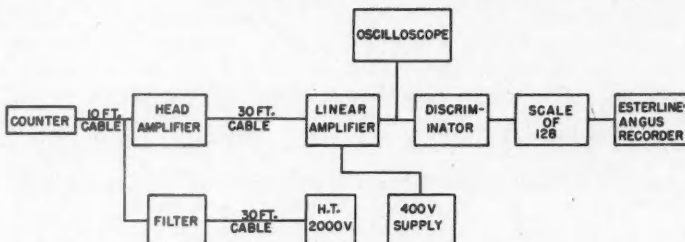


FIG. 2. Block diagram of electronic equipment.

### (b) Method of Recording Data

Two weeks of ZEEP time were allocated to these experiments, one in December 1946 and the other in January 1947. A total of 12 runs were carried out. In addition, counting losses were investigated after each of the two series of runs.

Before the experiments were begun all substances for the production of radio-nuclides for tracer work were removed from the pile. A shutdown period of at least eight hours preceded each series of runs in order to reduce the effect of previous operations. Activation periods of 10, 50, and 230 min. were chosen as suitable for bringing up the activities to various fractions of their saturation values.

In most of the runs the counts in units of 128 were recorded on moving paper by two Esterline-Angus pen recorders. The speeds chosen were 5, 80, and 300 sec. per in.

The power during the steady operation of ZEEP was monitored independently with a quartz-fiber electroscope\* (Type TQQ) located some thirty feet from the side of the pile. Although this measured ionization by  $\gamma$ -rays, it provided a more sensitive indication of flux changes than the power-indicating ion chamber in the graphite reflector. The rates of deflection, when corrected for changes in density of the air in the electroscope, were related to the counting rates in the uranium fission counter.

The fine control plate of the pile was usually kept at a fixed and well-elevated position during operation and shutdown. The power was kept steady with the coarse control plates. A few seconds before shutdown, the coarse control plates were moved slightly to a predetermined position so that, after shutdown, the multiplication constant of the reactor would have the same value in all runs. At zero time for recording the decay of the neutron sources both sets (A + B) of the cadmium shutoff rods were dropped into the pile. The end of recording occurred from 3 to 43 hr. later. Each run provided the background for the next.

### (c) Counting Losses

The observed counting rate  $n'$  (in units of 128 per minute) of a counter and its associated equipment was related to the rate of drift  $P$  of a TQQ electroscope placed between the water shield and the graphite reflector of the pile. The power was varied from 1 to 50 watts. The rate of drift was assumed to be directly pro-

\*Designed by Dr. H. Carmichael, Chalk River Laboratory.

portional to the neutron flux and hence to the true counting rate  $n$  of the neutron counter. This assumption appeared to be valid down to a power of about one watt, below which the effect of long-lived  $\gamma$ -activity from previous runs became noticeable.

The values of  $n'/P$  were plotted against  $P$  to give a curve that could be fitted by an expression of the form

$$n'/P = a - bP + cP^2,$$

where  $a$ ,  $b$ , and  $c$  are constants. Since  $aP$  represented the true counting rate  $n$ , the relation could be rewritten as

$$n' = n - \left(\frac{b}{a^2}\right)n^2 + \left(\frac{c}{a^3}\right)n^3,$$

or

$$n' = n - Bn^2 + Cn^3,$$

from which a graph of  $(n - n')/n'$  as a function of  $n'$  was drawn and used to make the corrections for counting losses. Table II contains the values of the two constants  $B$  and  $C$  so determined.

TABLE II  
CORRECTIONS FOR COUNTING LOSSES

Counter	December 1946		January 1947	
	$B \times 10^3$	$C \times 10^7$	$B \times 10^3$	$C \times 10^7$
Natural U	1.14	5		
Enriched U	0.54	0	1.05	5
Boron	1.07	5	1.22	9

The surprisingly large counting losses were probably caused by an unnecessarily long dead time in the discriminators. For the counting data on which most of the decay analysis depends, the losses were 5% or less.

(d) *Treatment of Recorded Data*

The following procedure was adopted to extract the recorded data from the paper charts. The counting rate of the natural uranium counter, prior to shutdown, was established by tabulating the time on the chart corresponding to every hundredth count of 128. For a few seconds before and for each of the dozen or so counts after shutdown the time for each count (of 128) was determined. The instant of shutdown was thereby established to one second. In the case of the enriched uranium counter, the time corresponding to every tenth count (of 128) was recorded for the first minute following shutdown, the time for every fifth count for the next two minutes, and for every count for an hour thereafter. Beyond this time the counting rate was too low to be useful. In the case of the boron counter, the time corresponding to every hundredth count (of 128) was recorded for the first 90 min., every fiftieth count for the following day, and every tenth count thereafter.

Wherever possible the counting rate was determined from the time for 100 counts (12,800 particles), and the rate correlated with the mean time for the

counting interval. Where the counting rates were low or where the decay period was changing rapidly this procedure was not possible, and the rate was determined from 50, 10, 5, or even 1 count with the concomitant loss in statistical accuracy. For the natural uranium counter prior to shutdown and for the boron counter throughout the run, from 50 to 100 counts were used for each determination of counting rate, which should be accurate to about 1%. Less accuracy was obtained in determining the rates with the enriched uranium counter in the interval from two to six minutes subsequent to shutdown, when the effective half-period of decay was short and changing rapidly and the rates were too small to use time intervals short compared to the half-period. Under these adverse circumstances the rates were based on 5 counts (640 particles) and a decay curve was drawn. This curve was then corrected for errors introduced by measuring the rates over intervals comparable to the half-period.

Counting loss corrections were finally applied to all the rates, and the corrected counting rates were plotted against the times. Fig. 3 shows part of a decay

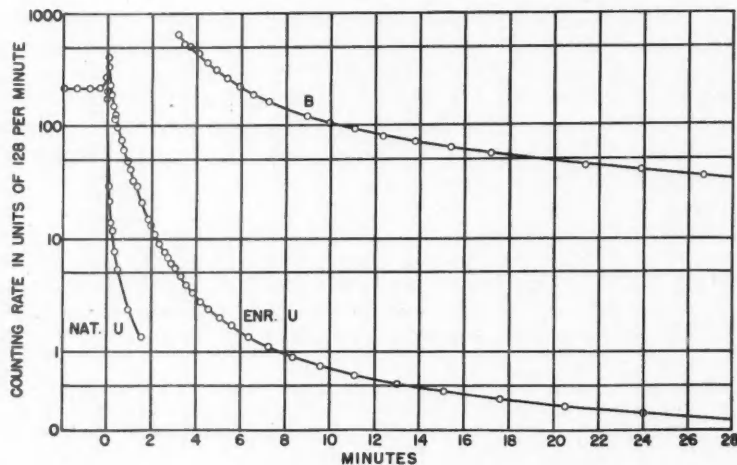


FIG. 3. Observed counting rates as a function of time after a typical 10-min. run (No. 11). Shutdown of the pile occurred at time zero.

curve\* for a typical run (No. 11). By intercalibration of the counters in the manner to be described in the following paragraph, it was then possible to express all counting rates in terms of the rates registered by the boron counter. Fig. 4, drawn from the data of runs No. 8, 9, and 12, shows in a convincing manner that the  $\gamma$ -emitting fission products are built up to various degrees during pile operations of different duration.

\*The slight rise in the power just before shutdown was caused by the small shift in the position of the coarse control plates already referred to. This rise in power has been omitted in drawing Fig. 4.

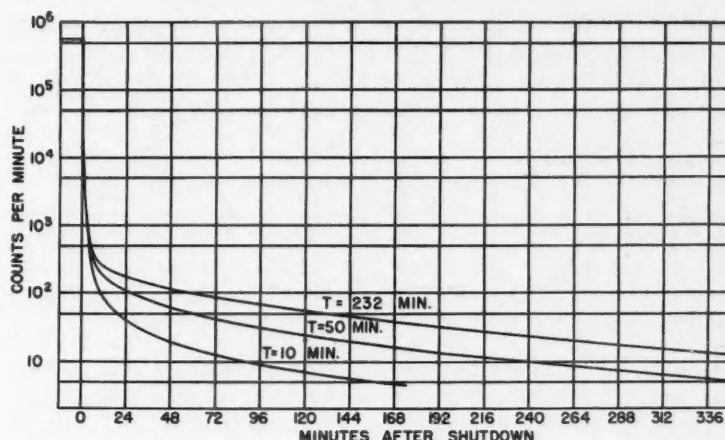


FIG. 4. Counting rates (referred to the boron counter) as a function of time after steady operation of the pile for times of 10, 50, and 232 min. (runs No. 8, 9, and 12).

(e) *Intercalibration of Counters*

From the graph of counting rate against time for a run, such as Fig. 3, the ratios of the rates of the boron and enriched uranium counters and of the enriched and natural uranium counters were directly determined. In addition to the counter sensitivities, these ratios include the normal spatial variation of neutron flux and shadow effects of the control plates and shutoff rods. The ratio of the counting rates of the boron and enriched uranium counters remained constant to 1% while the boron counting rates fell from 600 to 60 counts (of 128) per minute. This result checks the counting loss corrections for the boron counter. No similar check was possible with the uranium counters. Their ratio, obtained from graphs such as Fig. 3 and from some direct comparisons at low power operation, is regarded as known to 3 or 4%.

Table III contains the intercalibration ratios and other information for the various runs. The values of the counting rate  $n_0$  of the boron counter at 50 w. were calculated from the rates of the natural uranium counter using the intercalibration data. These values of  $n_0$  are required in finding the absolute intensities of the delayed and photoneutron groups. We have no satisfactory explanation of the discrepancy in the values of  $n_0$  for the December and January runs. The counters were removed between the two series of runs and then replaced but not exactly in the same positions. Moreover, the control plates were not at the same positions in the two series. Shadows cast either by the shutoff rods on the counters or by the control plates on the ion chamber may have been responsible for the discrepancy. The absolute yields of the delayed and photoneutron groups are therefore rather uncertain; the relative yields should be more accurate.

(f) *Measurement of the Change in  $k_e$  at Shutdown*

The effective multiplication constant,  $k_e$ , of a pile is unity under conditions of steady operation and is less than unity in all shutdown conditions. As will be

TABLE III  
INTERCALIBRATION OF COUNTERS

	December 1946 Runs No. 1 - 7	January 1947 Runs No. 8 - 12
Ratio B/enriched U	83.6 $\pm$ 0.4	148.1 $\pm$ 0.5
Ratio enriched U/natural U	66.1 $\pm$ 1.5	16.4 $\pm$ 0.3
Rate* natural U at 50 w.	83.4 $\pm$ 0.5	227 $\pm$ 2
Rate† TQQ at 50 w.	10.01 $\pm$ 0.03	11.29 $\pm$ 0.08
Calculated rate* B at 50 w. ( $n_0$ )	(461 $\pm$ 3) $\times 10^3$	(551 $\pm$ 5) $\times 10^3$
Ratio B/TQQ at 50 w.	(46.0 $\pm$ 0.4) $\times 10^3$	(48.7 $\pm$ 0.7) $\times 10^3$
$(c + \delta_1)/n_0$	$7.22 \times 10^{-8}$	$6.04 \times 10^{-8}$

\*In units of 128 particles per minute.

†In divisions per minute.

The probable errors shown have been derived from the residuals.

shown in the section on pile theory, the calculation of the fraction of the neutron population represented by delayed or photoneutrons requires a knowledge of  $\delta = 1 - k_e$  for the subcritical condition under which the data following shutdown were recorded. This value of  $\delta$  will be designated  $\delta_1$ . Two independent methods of measuring  $\delta_1$  were used.

The first method requires a measurement of the ratio of the sudden initial drop in power accompanying the release of the shutoff rods after a long period of steady operation to the residual power immediately after shutdown. For this purpose, the power-indicating ion chamber was used to record automatically on an Esterline-Angus recorder. From equation [16] it will be seen that this ratio is  $\delta_1/c$ , where  $c$  is the fraction of neutrons of all types that are delayed. Using the value  $c = 0.0080$  (to be justified later), the results of three trials are presented in Table IV.

TABLE IV  
DETERMINATION OF  $\delta_1$ 

Method 1		Initial drop in power	Residual power	$\delta_1(\%)$	
Trial No.				From $\delta_2$	From $\delta_3$
1		40.6	12.08	2.69	
2		1.47	0.48	2.45	
3		1.48	0.46	2.57	
			Average	2.57	

Method 2

Run No.	$\Delta h_2$ (cm.)	$\Delta h_3$ (cm.)	$\delta_1/\delta_2$	$\delta_1/\delta_3$	$\delta_1(\%)$	
					From $\delta_2$	From $\delta_3$
7	2.62	4.20	6.36	3.71	2.54	2.34
12	2.04	3.64	8.37	4.48	2.62	2.46
						Average 2.49

In run No. 4 the control plates were inadvertently moved after shutdown. For these shutdown conditions  $\delta$  was found to be 3.60%.

The second method of obtaining  $\delta_1$  involves a comparison of the neutron counting rate in the normal shutdown condition with those in other subcritical conditions described by values  $\delta_2$  and  $\delta_3$  (smaller than  $\delta_1$ ). Subsequently,  $\delta_2$  and  $\delta_3$  were obtained from the increases in the depth of the heavy water necessary to bring the reactor to the critical condition ( $\delta = 0$ ).

In the subcritical pile the neutron population is directly proportional to the strength of sources (photoneutrons and spontaneous fission), which are nearly constant several hours after shutdown. The neutron counting rate at a point in the pile is inversely proportional to  $\delta$  for constant sources. Hence, if the counting rates in the two subcritical conditions described by  $\delta_1$  and  $\delta_2$  are  $n_1$  and  $n_2$  respectively, the experimental ratio  $n_1/n_2$  is  $\delta_2/\delta_1$ .

The subcritical condition described by  $\delta_1$  is the normal one with shutoff rods "down" and the control plates in a preselected position very near that for normal operation, while  $\delta_2$  and  $\delta_3$  refer to slightly subcritical conditions where the shutoff rods are "up" and the control plates are moved to more effective positions. With the pile in the conditions described by  $\delta_2$  and  $\delta_3$ , the increments  $\Delta h_2$  and  $\Delta h_3$  in the depth of heavy water necessary to restore the critical condition were measured. Fig. 5 is included to illustrate the relation between the

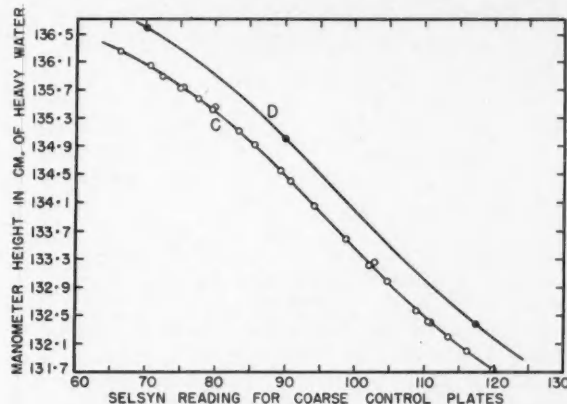


FIG. 5. Manometer height in centimeters of heavy water as a function of the height of the coarse control plates for a self-sustaining chain reaction. Curve C: fine control plates set at 190. Curve D: fine control plate set at 114. The lower ends of the uranium rods are at approximately 17.2 cm. on the manometer scale.

positions of the control plates (as read from the selsyn dials) and the depth of heavy water for a self-sustaining chain reaction in ZEEP. The values of  $\delta_2$  and  $\delta_3$  were calculated, using equation [17], from  $\Delta h_2$  and  $\Delta h_3$  and the known pile constants. Hence, two values of  $\delta_1$  were derived. From the results in Table IV, the mean value of  $\delta_1$  for the shutoff rods ( $A + B$ ) is 2.53%.

#### PILE THEORY

The theory of the kinetics or time behavior of the chain reaction was developed and put on record by Nordheim (18) and others (10, 23).

For each neutron absorbed in the pile,  $k_e$  neutrons are made available to carry on the chain reaction. Of these,  $k_e(1 - c)$  are immediately available and  $k_e c \mu_i$  are stored in nuclei of type  $i$ . The photoneutrons may be included with the delayed neutrons in spite of their different origin. The total number of free neutrons,  $r_1$ , in the pile and the stored neutrons,  $r_i$ , associated with various delays change with time  $t$  according to the following differential equations:

$$[1] \quad \frac{dr_1}{dt} = -\frac{r_1}{\tau} + r_1 \frac{k_e(1 - c)}{\tau} + \sum_{i=2}^n \lambda_i r_i,$$

$$[2] \quad \frac{dr_i}{dt} = \frac{k_e c \mu_i r_1}{\tau} - \lambda_i r_i,$$

where  $i = 2, 3, 4, \dots, n$ .

The following symbols are being used:

$k_e$  = effective multiplication constant of the pile,

$c$  = total fraction of neutrons delayed,

$\mu_i$  = fraction of delayed neutrons of type  $i$ ,

and  $\tau$  = mean lifetime of a neutron in the pile.

The following changes in notation lead to shorter differential equations:

$$[3] \quad \delta = 1 - k_e,$$

$$[4] \quad \lambda_1 = (\delta + c - c\delta)/\tau,$$

$$[5] \quad \text{and} \quad \Lambda_i = (1 - \delta)c\mu_i/\tau.$$

Equations [1] and [2] become

$$[6] \quad \frac{dr_1}{dt} = -\lambda_1 r_1 + \sum_{i=2}^n \lambda_i r_i,$$

$$[7] \quad \frac{dr_i}{dt} = -\lambda_i r_i + \Lambda_i r_1.$$

During the period of activation of duration  $T$  the value of  $r_1$  is kept constant. It may be set equal to  $n_0$  as measured with the neutron counter. The delayed and photoneutrons,  $r_i$ , are built up from negligible values to fractions of their saturation values,  $F_i$ , given by

$$[8] \quad F_i = 1 - e^{-\lambda_i T}.$$

The solutions of equations [6] and [7] under these conditions are

$$[9] \quad r_1 = n_0, \quad r_i = (\Lambda_i F_i / \lambda_i) n_0,$$

which are the initial conditions for the solutions of equations [6] and [7] following shutdown with the cadmium rods. The value of  $\delta$  is changed to  $\delta_1 = 2.53\%$  within one or two seconds of steady operation. During this interval  $\delta$  and  $\lambda_1$  change rapidly and come to their steady values defined above. An exact solution is not possible if the production of further stored neutrons is included. However,  $\lambda_1$  is much larger than any of the  $\lambda_i$ 's, and for this reason a good approximation to the solution can be found for this perturbation problem.

The solution for  $r_1$  may be written

$$[10] \quad r_1 = \sum_{i=1}^n A_i e^{-\alpha_i t}.$$

The values of  $A_i$  and  $\alpha_i$  may be expressed in terms of the  $\mu_i$ 's and  $\lambda_i$ 's through the following equations:

$$[11] \quad \alpha_i = \lambda_i(1 + \epsilon_i),$$

where  $\epsilon_i \ll 1$ ,

$$[12] \quad \lambda_1 \epsilon_1 = \sum_{i=2}^n \frac{\lambda_i \Delta_i}{\lambda_1 - \lambda_i},$$

$$[13] \quad \epsilon_i = -\frac{A_i}{F_i n_0} = -\frac{\Delta_i}{\lambda_1 - \lambda_i},$$

$$[14] \quad \lambda_i = \alpha_i \left(1 + \frac{A_i}{F_i n_0}\right),$$

and

$$[15] \quad c\mu_i = (c + \delta_1) \frac{A_i}{F_i n_0}.$$

The experimental decay curve may be analyzed into a sum of exponentials of the form of equation [10]; and the values of  $A_i$  and  $\alpha_i$  so obtained may be related to the desired neutron yields  $c\mu_i$  and transformation constants  $\lambda_i$  through the use of equations [11] to [15].

Equation [15] may be directly used to determine the sudden relative drop in power that occurs in the first few seconds of shutdown. This ratio is evidently

$$[16] \quad \left[ n_0 - \sum_{i=2}^n A_i \right] / \sum_{i=2}^n A_i = \delta_1/c.$$

Rumsey (20) has considered the modifications to pile theory that are necessary for the interpretation of experiments involving the kinetics of piles with reflectors. The following formula pertaining to ZEEP in a subcritical condition was derived:

$$[17] \quad \delta = \frac{\pi^2 (2h + \Delta h) \Delta h}{h^2 (h + \Delta h)^2} (M^2 + 2K^2 L^2 L_s^2).$$

For ZEEP the square of the slowing-down length,  $L_s^2$ , and the square of the diffusion length,  $L^2$ , for neutrons in the lattice are both approximately  $118.5 \text{ cm.}^2$ . The migration area  $M^2 = L_s^2 + L^2 = 237 \text{ cm.}^2$  From the spatial distribution of slow neutrons in ZEEP, we have found that the Laplacian  $K^2$  is  $794 \times 10^{-6} \text{ cm.}^{-2}$  and the vertical distance  $h$  between the two horizontal planes where the neutron density vanishes is  $148.5 \text{ cm.}$  (15). The value of  $M^2 + 2K^2 L^2 L_s^2$  is therefore approximately  $260 \text{ cm.}^2$  Equation [17] determines the values of  $\delta$  for the various subcritical conditions discussed in the previous section.

#### ANALYSIS OF DECAY CURVES

Each neutron decay curve was analyzed as the sum of a number of decreasing exponentials (equation 10) by the well-known "peeling" process. Figs. 6-8 show

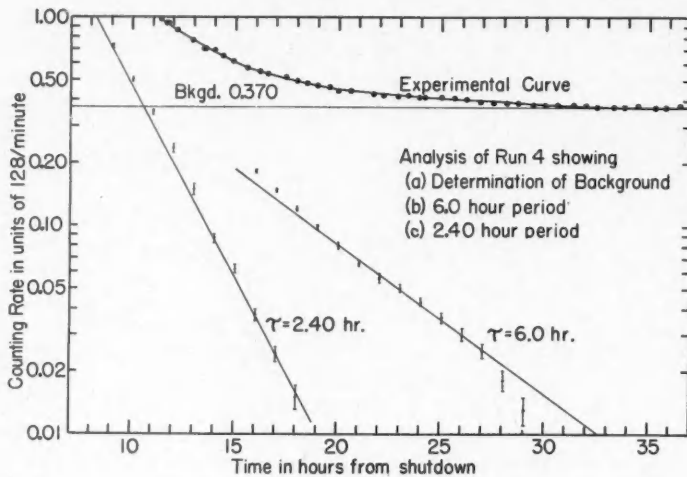


FIG. 6. Part of the analysis of a 50-min. run.

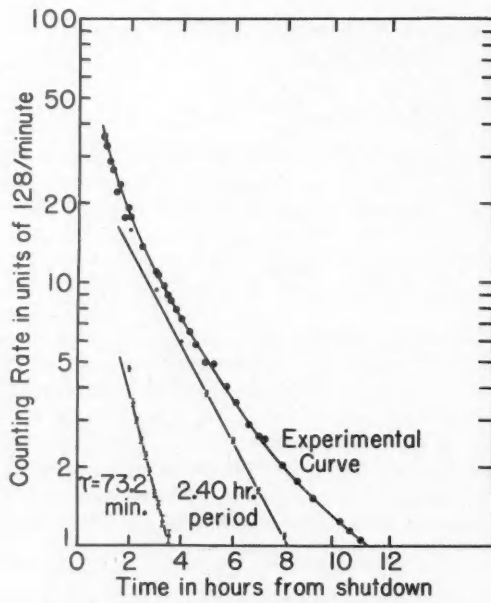


FIG. 7. Part of the analysis of a 50-min. run.

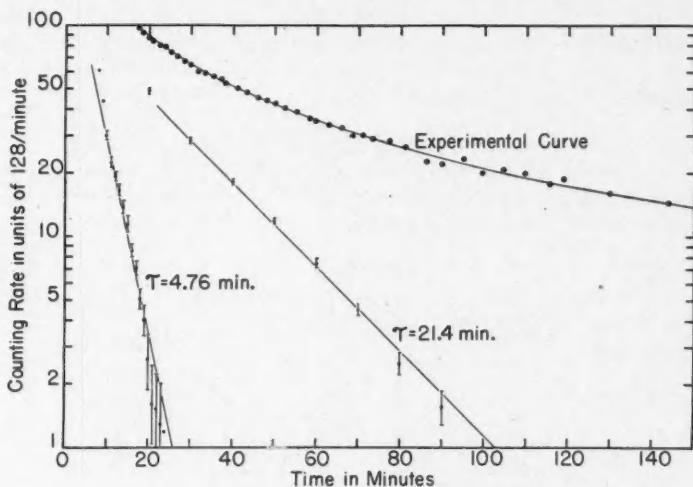


FIG. 8. Part of the analysis of a 50-min. run.

the application of the method. When, as in these cases, there are many components, the method is subject to serious cumulative errors. Attempts to minimize such errors have been made by varying the activation time and by having the curves analyzed independently by two persons.

The limited time allotted to these experiments made it impossible to follow each run until the counting rate reached the apparently steady value determined by long-period sources such as 12.8-day Ba-La<sup>140</sup> and by spontaneous fission. The backgrounds used were based on the values obtained in the two longest runs, Nos. 4 and 12, in which the counting rate had become apparently constant. These values of 0.37 and 0.69 units of 128 per minute (measured at different  $\delta$ 's) are approximately three times those estimated for spontaneous fission alone.

#### THE TOTAL FRACTION OF NEUTRONS DELAYED

Since the analyses could not be extended to give directly the intensities  $c\mu_i$  of the very short lived groups of neutrons, it was necessary to choose  $c$  ( $= \sum c\mu_i$ ) in order to obtain the absolute yields of the various photoneutron groups observed. The value  $c = 0.0080$  was arrived at in the following manner. The total fraction of fission neutrons that are delayed was found to be 0.00755 by Hughes *et al.* (14). Bernstein *et al.* (3) found that the total yield of photoneutrons was 16% of the saturated delayed neutron activity when their measurements were corrected to an infinite volume of heavy water around an irradiated sample of uranium having negligible  $\gamma$ -ray absorption. Evidence to be presented later shows that about 26% of the energetic  $\gamma$ -rays escape from the ZEEP rods. The photoneutron contribution to  $c$  in ZEEP is therefore  $26\% \times 16\% \times 0.00755 = 0.00031$ . Hence  $c = 0.00786$ . If we use a photoneutron yield estimated at 28% of the delayed neutrons by Spatz *et al.* (24) in an experiment similar to that

of Bernstein, the photoneutron contribution to  $c$  is  $26\% \times 28\% \times 0.00755 = 0.00055$ , and hence  $c = 0.00810$ . Gilbert and Fergusson (11) found  $c = 0.0083$  in an experiment in which the ZEEP power was modulated with a rotating cadmium shutter. We have adopted  $c = 0.0080$ .

### EXPERIMENTAL RESULTS

The final values of the mean lifetimes and yields  $c\mu_t$  of the various groups of delayed and photoneutrons are shown in Table V. The probable errors shown have been calculated from the residuals.

TABLE V  
SUMMARY OF MEAN LIFETIMES AND YIELDS  
OF DELAYED AND PHOTONEUTRONS

Mean lifetime	Yield $\times 10^6$
5.8 $\pm$ 0.3 sec.	257 $\pm$ 29
30.0 $\pm$ 0.5 sec.	172 $\pm$ 9
81.9 $\pm$ 0.5 sec.	33 $\pm$ 1
5.45 $\pm$ 0.08 min.	2.32 $\pm$ 0.08
22.8 $\pm$ 0.3 min.	1.07 $\pm$ 0.03
72.4 $\pm$ 1.5 min.	0.50 $\pm$ 0.03
2.48 $\pm$ 0.02 hr.	0.82 $\pm$ 0.04
6.15 $\pm$ 0.06 hr.	(0.13 $\pm$ 0.02)

### DISCUSSION

The first three groups of neutrons listed in Table V are mostly delayed neutrons from fission. The mean lifetimes 5.8, 30.0, and 81.9 sec. agree with 6.5, 31.8, and 80.2 sec. found by Hughes *et al.* (14) in their study of the delayed neutrons. The yields 257, 172, and 33 (relative to  $10^6$  fission neutrons) are also in approximate agreement with 213, 166, and 25 measured by Hughes. The photoneutrons produced by the  $\gamma$ -rays of short-period fission products in ZEEP are therefore strongly masked by the delayed neutron groups.

For the purpose of comparison, Table VI presents a summary of the most detailed investigations of delayed and photoneutrons. The yields of the photoneutron groups have been normalized to  $166 \times 10^{-6}$  for the 31.8-sec. delayed neutron group (14), which is sufficiently prominent for the purpose. The mean lifetimes 6.15 hr. and 2.48 hr. found in the present work agree with 6.3 hr. and 2.4 hr. found by Bernstein *et al.* (3). Marked disagreement in the mean lifetimes occurs at the weak group of photoneutrons with a mean lifetime of 72.4 min. observed in the present work. Since errors in analysis are cumulative, the disagreement in lifetimes persists into the stronger 22.8 min. and 5.45 min. groups. The delayed neutron groups at 80.2, 31.8, and 6.5 sec. are sufficiently strong that even small admixtures of photoneutrons and cumulative errors do not prevent our obtaining agreement with Hughes *et al.* (14).

The photoneutron yields in ZEEP are very much less than those found by either Bernstein or Spatz in their investigations using thin  $\gamma$ -ray sources of irradiated uranium. Since the short-lived groups are strongly masked by the delayed neutrons in our work, an over-all comparison is less likely to be signi-

TABLE VI

A COMPARISON OF VALUES OF MEAN LIFETIMES AND YIELDS OF DELAYED AND PHOTONEUTRONS

Hughes (14) Delayed only	Mean lifetimes			Yields relative to $10^6$ fission neutrons			
	Spatz (24)	Bernstein (3)	Present work Delayed and photo- neutrons	Hughes (14)	Spatz (24)	Bernstein (3)	Present work
0.07 sec.				25			
0.62 sec.				85			
2.19 sec.				241			
6.50 sec.	9.7 sec.	3.6 sec.	5.8 sec.	213	112	78	248
31.8 sec.	43 sec.	59 sec.	30.0 sec.	166	*	*	166*
80.2 sec.			81.9 sec.	25	79	24.4	32
	2.2 min.	3.4 min.	5.45 min.		12.4	8.37	2.24
	9.4 min.	11 min.	22.8 min.		3.6	4.02	1.03
	46 min.	39 min.	72.4 min.		2.0	2.47	0.48
	2.9 hr.	2.4 hr.	2.48 hr.		1.6	2.79	0.80
		6.3 hr.	6.15 hr.			0.385	(0.12)
	33 hr.	76 hr.			0.5		0.123
	Total yields			755	211	120.5	47†
	Total yields			100%	28%	16%	6%

\* Normalized to 166 to agree with Hughes (14).

† This sum represents only photoneutron contributions; the 5.8 sec. and 81.9 sec. yields are assumed to include photoneutron contributions of 248 - 213 = 35 and 32 - 25 = 7 respectively.

ficant than one involving only the longer lifetimes. The total yield for the five longest lifetimes in ZEEP is  $4.67 \times 10^{-5}$  of fission neutrons, which is 26% of Bernstein's value for comparable periods. This reduction of 74% is in agreement with the following calculated absorption of energetic  $\gamma$ -rays in the uranium rods of ZEEP. Since the absorption coefficient for  $\gamma$ -rays in the energy range 2.23 to 3 Mev. changes very slowly with energy, it will be sufficient to select the value  $4.45 \times 10^{-2}$  cm.<sup>2</sup>/gm. obtained by Hatton (12) of this laboratory for the absorption of the 2.62 Mev. thorium C''  $\gamma$ -rays in uranium. Using this coefficient and Kushneruk's graph (16) of the absorption of  $\gamma$ -rays from uniformly distributed sources in a rod, the absorption is found to be 67%. The neighboring rods in the lattice absorb about 12% of the  $\gamma$ -rays that escape from the source rod. The total absorption of  $\gamma$ -rays in the uranium rods of ZEEP is therefore 71%, which is in agreement with the photoneutron reduction of 74%.

For calculations in pile kinetics, we have adopted the mean lifetimes and yields of delayed and photoneutrons measured by Hughes (14) and Bernstein (3). The photoneutron yields were reduced to 26% of the measured values to take account of  $\gamma$ -ray absorption in the ZEEP rods. Table VII contains the recommended information, which has been used at Chalk River. Some confirmation of the essential correctness of these data has been found by Bayly (1), who obtained good agreement between measured and calculated periods of ZEEP when divergent.

TABLE VII  
DELAYED AND PHOTONEUTRONS IN ZEEP. RECOMMENDED DATA

Mean lifetime $\tau_i$ (sec.)	Yield $c\mu_i \times 10^8$	$\mu_i \times 10^8$
Delayed neutrons	0.07	25.5
	0.62	86.7
	2.19	246.5
	6.50	217.6
	31.8	170
	80.2	26.0
Photo- neutrons	3.6	20.73
	59.0	6.50
	204	2.23
	660	1.07
	2340	0.659
	8640	0.743
	22680	0.102
	273600	0.0327

$$c = \sum c\mu_i = 0.8044\%, \quad \sum \mu_i = 1.00.$$

It has not been possible to identify unambiguously the hard  $\gamma$ -ray-emitting fission products responsible for the production of photoneutrons.

#### ACKNOWLEDGMENTS

We should like to express our gratitude to Mr. K. Elston and Misses J. Craig and M. F. Gauthier, who greatly assisted in recording the data and analyzing the decay curves, and to Miss G. E. Marshall for drawing the figures.

#### REFERENCES

1. BAYLY, J. G. Can. J. Phys. 31: 182. 1953.
2. BELL, R. E. and ELLIOTT, L. G. Phys. Rev. 79: 282. 1950.
3. BERNSTEIN, S., PRESTON, W. M., WOLFE, G., and SLATTERY, R. E. Phys. Rev. 71: 573. 1947.
4. DE HOFFMANN, F., FELD, B. T., and STEIN, P. R. Phys. Rev. 74: 1330. 1948.
5. ELLIOTT, L. G. Unpublished work. 1944.
6. ELLIOTT, L. G. Unpublished work. 1945.
7. ELLIOTT, L. G., HINCKS, E. P., and MAY, A. N. Can. J. Research, A, 26: 386. 1948.
8. FENNING, F. W. Unpublished work. 1946.
9. FLOWERS, B. H. Proportional neutron counters. Report CRP-292. 1946.
10. FRIEDMAN, F. L. The science and engineering of nuclear power. Vol. I. Addison-Wesley Press Inc., Cambridge, Mass. 1947. Chap. 5, p. 111.
11. GILBERT, C. W. and FERGUSSON, G. J. An investigation of the delayed neutrons from fission. Report CRP-377. 1948.
12. HATTON, J. Unpublished work. 1946.
13. HINCKS, E. P. Private communication. 1949.
14. HUGHES, D. J., DABBS, J., CAHN, A., and HALL, D. Phys. Rev. 73: 111. 1948.
15. JOHNS, M. W. and SARGENT, B. W. Distribution of neutron density and the derived Laplacian in ZEEP. Report CRP-355. 1947.
16. KUSHNERIK, S. Unpublished work. 1947.
17. MAY, A. N. Unpublished work. 1944.
18. NORDHEIM, L. W. Phys. Rev. 70: 115 (Abstract S1). 1946.
19. REDMAN, W. C. and SAXON, D. Phys. Rev. 72: 570. 1947.
20. RUMSEY, V. H. On the analysis of experiments involving the kinetics of piles with reflectors. Report CRT-372. 1948.
21. SARGENT, B. W. The science and engineering of nuclear power. Vol. II. Addison-Wesley Press Inc., Cambridge, Mass. 1949. Chap. 5, p. 58.
22. SNELL, A. H., NEDZEL, V. A., IBSEN, H. W., LEVINGER, J. S., WILKINSON, R. G., and SAMPSON, M. B. Phys. Rev. 72: 541. 1947.
23. SOODAK, H. The science and engineering of nuclear power. Vol. II. Addison-Wesley Press Inc., Cambridge, Mass. 1949. Chap. 8, p. 89.
24. SPATZ, W. D. B., HUGHES, D. J., and CAHN, A. Phys. Rev. 72: 163 (Abstract G4). 1947; MDDC-871. 1947.

## DISINTEGRATION OF $\text{Au}^{198}$ <sup>1</sup>

BY L. G. ELLIOTT, M. A. PRESTON,<sup>2</sup> AND J. L. WOLFSON

### ABSTRACT

In addition to the 411.77 kev.  $\gamma$ -ray transition, two  $\gamma$ -ray transitions of energies  $676.5 \pm 0.8$  kev. and  $1088.9 \pm 0.9$  kev. have been observed in  $\text{Hg}^{198}$  following the disintegration of  $\text{Au}^{198}$ . The intensities of these transitions were found to be  $(8.20 \pm 0.56) \times 10^{-3}$  and  $(1.63 \pm 0.12) \times 10^{-3}$  per disintegration respectively. The  $K$  conversion coefficient of the 676.5 kev. transition was measured as  $0.0224 \pm 0.0019$ , identifying the radiation as a mixture of magnetic dipole and electric quadrupole. The  $K$  conversion coefficient of the 1088.9 kev. transition was measured as  $0.00450 \pm 0.00034$ , identifying this radiation as electric quadrupole.

A  $\beta$ -transition to the ground state of  $\text{Hg}^{198}$ , of energy 1371 kev. and intensity  $(2.5 \pm 0.5) \times 10^{-4}$  per disintegration, has been observed and identified as a third order forbidden transition. The shape of this spectrum has been studied above the end point of the intense 959 kev.  $\beta$ -transition. Of the four combinations considered for the  $\beta$ -decay interaction form, viz.  $SA$ ,  $VA$ ,  $ST$ ,  $VT$ , it was found that the experimental shape can be fitted by any one of  $VA$ ,  $ST$ , or  $VT$ , but not by  $SA$ . The  $\log f/d$  value for the transition is 11.7.

A disintegration scheme is proposed in which the excited states of  $\text{Hg}^{198}$  at 412 and 1089 kev. are each assigned spin 2 and even parity and the ground state of  $\text{Au}^{198}$  spin 3 and odd parity.

### I. INTRODUCTION

$\text{Au}^{198}$  (2.69 day) decays by  $\beta^-$  emission, the main branch proceeding to the first excited state in  $\text{Hg}^{198}$  at 412 kev., followed by the emission of a  $\gamma$ -ray to the ground state which is partially internally converted. The end point of the main  $\beta$ -spectrum has been measured by many observers (4, 15, 16, 35, 39), the most recent determination being that of Fan (6) who reported a value of 961 kev. Langer and Price (15) have shown the spectrum to be of the "allowed" shape, consistent with the results of Ridgway (27) and Stump and Frankel (40) who find no  $\beta$ - $\gamma$  angular correlation. Renard (26) has shown that  $K$  capture if present occurs in  $<0.4\%$  of the disintegrations, while Mims and Halban (20) have found that  $\beta^+$  emission occurs in  $<3.3 \times 10^{-3}\%$  of the disintegrations.

The most precise determination of the energy of the 412 kev.  $\gamma$ -ray in  $\text{Hg}^{198}$  has been made by Muller *et al.* (22) who reported a value of 411.770  $\pm 0.036$  kev. In addition to this  $\gamma$ -ray, two others of energies about 680 kev. and 1090 kev. have been reported by Cavanagh *et al.* (3), Pringle and Standil (24), Elliott and Wolfson (5), and Hubert (13). Cavanagh (2) has shown that the 412 kev.  $\gamma$ -ray is in cascade with the 680 kev. transition. All workers agree that the 1090 kev.  $\gamma$ -ray is a crossover transition. Elliott and Wolfson (5, 42) have observed a very weak  $\beta^-$  transition to the ground state of  $\text{Hg}^{198}$ , and Brosi *et al.* (1) have observed a third weak  $\beta^-$  transition of energy 290 kev. by counting  $\beta$ -rays in coincidence with the 680 kev.  $\gamma$ -ray. They conclude that this low energy transition proceeds to the 1090 kev. state in  $\text{Hg}^{198}$ .

The  $K$ ,  $L$ , and  $M$  conversion coefficients of the 412 kev. transition have been measured by many observers (6, 12, 13, 32, 35, 36, 39), the most recent mea-

<sup>1</sup> Manuscript received October 2, 1953.

Contribution from Physics Division, Atomic Energy of Canada Limited, Chalk River Laboratory, Chalk River, Ont. Issued as A.E.C.L. No. 91.

<sup>2</sup> Present address: Department of Physics, McMaster University, Hamilton, Ont.

surement being that of Simons (37), who has found the value for the  $K$  conversion coefficient to be in excellent agreement with the calculated value of Rose (28) for electric quadrupole radiation. Measurements of the half life of this transition have also been found to be consistent with assignment of electric quadrupole character. Values of  $<3 \times 10^{-11}$  sec.,  $(2.1 \pm 0.5) \times 10^{-11}$  sec., and  $5.5 \times 10^{-11}$  sec. have been obtained by Graham and Bell (9), Moon and Davey (21), and Malmfors\* (19) respectively.

In the present paper the results of a detailed study of the disintegration of  $\text{Au}^{198}$  are presented. The  $\gamma$ -rays of energies 676.5 and 1088.9 kev. have been observed both in internal and external conversion and their intensities and conversion coefficients measured. The energy and intensity of the weak  $\beta^-$  transition to the ground state of  $\text{Hg}^{198}$  have been measured, and the shape of the spectrum above 975 kev. has been studied. From the data obtained the spins and parities of the states in  $\text{Hg}^{198}$  and the ground state in  $\text{Au}^{198}$  have been deduced. A disintegration scheme incorporating these results is proposed.

## II. APPARATUS

Two magnetic lens spectrometers have been used in the studies. For the examination of  $\beta$ -ray spectra and internal conversion lines, a spectrometer using two coaxial magnetic lenses was employed. The instrument is shown schematically in Fig. 1. The source is mounted on a thin backing and placed

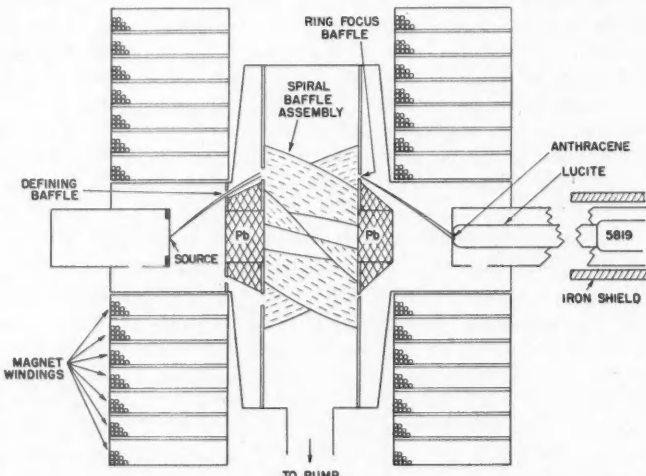


FIG. 1. Double lens  $\beta$ -ray spectrometer used in the study of  $\beta$ -ray spectra and internal conversion lines. In these experiments only the outer three windings on each magnet were used.

at the center of one of the coils. The detector, an anthracene disk  $\frac{5}{8}$  in. in diameter and about 1 mm. thick, is situated at the center of the other magnet

\*We have multiplied Malmfors' value ( $1.6 \times 10^{-11}$  sec. for the mean life) by a factor of 5 to take into account the statistical weight of the 412 kev. state.

coil. A lucite light pipe 30 in. long conducts the light flashes from the anthracene to a magnetically shielded 5819 photomultiplier. Ring focusing is employed, the focus occurring at the annulus in the baffle nearest the detector. The distance from source to detector is 50 cm. A set of spiral baffles made of aluminum coated copper is installed, so that for a given direction of magnetic field the instrument selects electrons of one sign only. However, in the present application these baffles serve the purpose of reducing the transmission of electrons scattered by the annular baffles and walls of the vacuum chamber. Additional quantities of lead, not shown in the figure, are disposed in the chamber so as to reduce the background due to primary and secondary quanta. As adjusted in these studies, the instrument has a measured transmission of about 0.5% and the line width at half maximum intensity is 0.5% in momentum. The momentum measurements are made in terms of the voltage drop across a single manganin resistor, placed in series with the magnet current, and kept at a constant temperature in an oil bath. The magnet current is stabilized to better than one part in 5000. The  $K$  interval conversion line of the  $411.77 \pm 0.036$  kev. (22) transition was used to calibrate the spectrometer.

Because of the low intensity of the high energy  $\beta^-$  transition it was felt necessary to investigate carefully the background due to scattered electrons above the end point of a simple  $\beta$ -spectrum, since an appreciable contribution of scattered electrons from the intense 959 kev. spectrum could easily mask the true shape of the higher energy spectrum. The investigation was carried out by examining the region near and beyond the end point of the  $P^{22}$  spectrum which is known to be simple. It was found that the counting rate in excess of counter background extended for three to four line widths beyond the end point of the spectrum, after allowing for the finite resolution of the spectrometer, and was just detectable above the counter background. The correction applied to the measured high energy  $Au^{198}$  spectrum on account of this effect amounted to less than 1% of the counting rate for the experimental point at 975 kev. For the remainder of the data, the corrections required were completely negligible.

The background due to  $\gamma$ -rays was investigated using a 35 mc. source of  $Au^{198}$  covered with sufficient beryllium absorber to remove all primary  $\beta$ -rays from the beam. The background counting rate which was measured at the same momentum values as used for the high energy  $Au^{198}$   $\beta$ -spectrum was 6 counts per minute, of which 2 counts per minute was the counter background. There was no variation of background over the momentum range of interest. With the 7-mc. sources used in the experiments the  $\gamma$ -ray background was therefore 0.8 counts per minute.

Another subsidiary experiment was performed to determine the amount of magnetic shielding required by the photomultiplier. The front face of the anthracene crystal was covered with thick aluminum and a  $Co^{60}$  source was placed outside the vacuum chamber. The counting rate was then measured over the same range of magnetic fields as used in the study of the high energy  $\beta$ -spectrum. Sufficient shielding was then added until the counting rate became independent of the magnetic field.

For  $\gamma$ -ray studies a single lens spectrometer was employed. The line width of this instrument is 1.5% in momentum at half maximum intensity, and the transmission 0.16%. The detector consisted of an anthracene disk 1 mm. thick and 4 mm. in diameter. A lucite light pipe conducted the light to a magnetically shielded 5819 photomultiplier outside the intense magnetic field. The studies were concerned exclusively with measurements of  $\gamma$ -ray intensities by comparison of the intensities of the corresponding *K* shell photoelectron lines externally converted in an 8 mgm./cm.<sup>2</sup> thorium radiator, 4 mm. in diameter. The end plate of the spectrometer was provided with an aluminum rod which projected about 1½ in. into the vacuum chamber to the end of which the thorium radiator was affixed. A hole 4 mm. in diameter was drilled into the rod to within 1 mm. of the end, and sources enclosed in aluminum containers were inserted into this hole from outside the vacuum chamber so as to occupy a standard position relative to the thorium radiator.

### III. THE $\beta$ -SPECTRUM

The gold sources used were all 1 mm. in diameter mounted on 2.7 mgm./cm.<sup>2</sup> thick aluminum foil. The aluminum foil itself was mounted on a dural ring with an inner hole 1⅓ in. in diameter. After centering, the source was placed in the spectrometer as shown in Fig. 1. Sources of Au<sup>198</sup> of thickness 0.2, 1.0, 2.5, and 5.0 mgm./cm.<sup>2</sup> were used in different trials.

Sources of thickness 0.2 mgm./cm.<sup>2</sup> were used in the study of the 959 kev. spectrum and in observing the internal conversion lines. For the detailed examination of the high energy spectrum above 975 kev., and for measuring the *K/L* ratio of the 1089 kev.  $\gamma$ -transition, sources of thickness 2.5 mgm./cm.<sup>2</sup> were used. An experiment was performed to demonstrate that for these purposes the 2.5 mgm./cm.<sup>2</sup> sources could be considered "thin". Counting rates were measured at 17 energy values from 440 kev. to 1350 kev. using sources of thickness 1, 2.5, and 5 mgm./cm.<sup>2</sup> of known relative activities. From these data it was found that above 850 kev., for a given source strength, the variation of counting rate with source thickness was negligible over the range of thicknesses used.

The spectrum above 2560 gauss-cm. taken with a source of thickness 0.2 mgm./cm.<sup>2</sup> is shown in Fig. 2. Evidence was presented in Section II to show that the continuum above the end point of the 959 kev.  $\beta$ -spectrum was not due to electrons from the lower energy component scattered into the detector. In addition, however, the electrons were demonstrated to be of high energy by a simple absorption experiment in which the anthracene detector was covered with 140 mgm./cm.<sup>2</sup> of aluminum foil, and the counting rates were observed at spectrometer settings of 600 kev., 1005 kev., and 1025 kev. The second point lies at the peak of the *K* internal conversion line of the 1089 kev. transition, so that the electrons counted are known to be of high energy. The point at 1025 kev. lies between the *K* and *L* internal conversion lines of the 1089 kev. transition, and at this energy only those electrons belonging to the high energy continuum are counted. At the 600 kev. setting it was found that

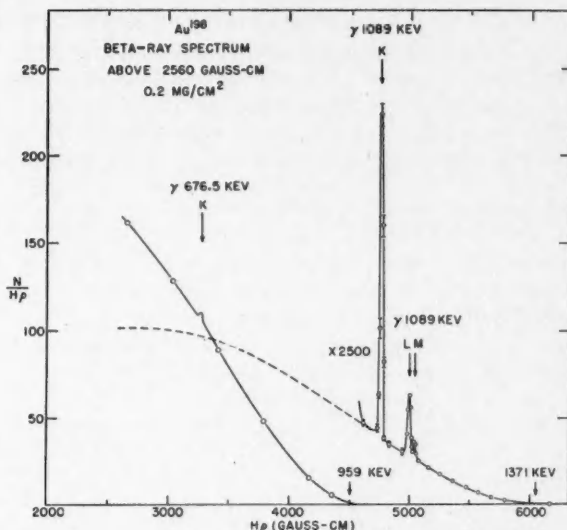


FIG. 2. Plot of the  $\beta$ -spectrum of  $Au^{198}$  above 2560 gauss-cm. The  $L$  internal conversion line of the 676.5 kev. transition, not shown, is about one sixth of the  $K$  line.

the absorber caused the counting rate to be reduced by a factor of  $5.3 \pm 0.5$ , while at the 1005 kev. and 1025 kev. settings the reduction factors were  $2.0 \pm 0.1$  and  $2.0 \pm 0.2$  respectively. Finally, using a more intense source, the high energy continuum was examined over a period of eight days, and it was found to decay at the same rate as the  $K$  internal conversion line of the 412 kev.  $\gamma$ -ray transition. From the results of these experiments it is concluded that the high energy continuum constitutes a genuine  $\beta$ -ray spectrum resulting from the disintegration of  $Au^{198}$ .

The main component of the  $\beta$ -ray distribution, at energies above 412 kev., was found to have the "allowed" shape, in agreement with the results of Langer and Price (15). A Fermi plot of this component yielded an extrapolated end point of  $959 \pm 2.5$  kev. An allowed Fermi plot of the high energy component yielded an extrapolated end point of  $1370 \pm 4$  kev., which agrees with the sum of the energies of the  $411.77 \pm 0.036$  kev.  $\gamma$ -transition and the  $959 \pm 2.5$  kev. main  $\beta$ -ray transition. This  $\beta$ -ray transition is accordingly believed to proceed to the ground state of  $Hg^{198}$ . A discussion of the shape of this spectrum is given in Section VII below. An estimate of the intensity of the 1371 kev. component relative to the 959 kev. component was made by constructing the two spectra from their Fermi plots extrapolated to zero energy, and measuring the ratio of their areas. The intensity of the high energy component was found in this way to be  $(2.5 \pm 0.5) \times 10^{-4}$  of the 959 kev. component. The corresponding  $\log f_0 \ell$  value is 11.7.

## IV. INTERNAL CONVERSION SPECTRUM

Internal conversion lines corresponding to three  $\gamma$ -ray transitions have been observed. In addition to the  $K$ ,  $L$ , and  $M$  lines of the well-known 411.77 kev. transition,  $K$  and  $L$  lines of a  $676.5 \pm 0.8$  kev. transition and  $K$ ,  $L$ , and  $M$  lines of a  $1088.9 \pm 0.9$  kev. transition have been observed. These are shown in detail in Fig. 3. The intensities of the  $K$  lines of each of the transitions have

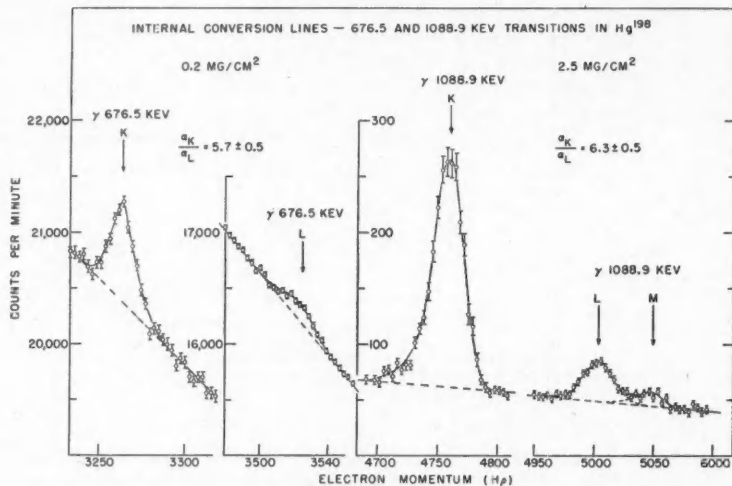


FIG. 3. Internal conversion lines of the 676.5 and 1088.9 kev. transitions in  $\text{Hg}^{198}$ . The vertical bars represent standard deviations. The intensities of the lines are proportional to the line areas divided by their corresponding momenta.

been followed in the spectrometer over a period of three half-lives. The intensities of these lines, relative to the 412 kev.  $K$  internal conversion line, were found to be constant within the statistical errors, indicating that the transitions were associated with  $\text{Au}^{198}$  decay. The  $K-L$  differences of both sets of lines were also measured. The values of  $67.9 \pm 0.6$  kev. and  $68.0 \pm 0.5$  kev., found for the 676 and 1089 kev. transitions respectively, constitute evidence that conversion takes place in the  $\text{Hg}$  atom and, in particular, that the transitions do not follow  $K$ -capture.

The ratios of conversion coefficients  $\alpha_K/\alpha_L$  were found for each transition by comparing the intensities of the  $K$  lines with the intensities of the corresponding  $L$  lines.

The values obtained were:

$\gamma$ -Ray energy	$\alpha_K/\alpha_L$
676.5 kev.	$5.7 \pm 0.5$
1088.9 kev.	$6.3 \pm 0.5$

For the measurements on the lines of the 677 kev. transition a source 0.2 mgm./cm.<sup>2</sup> thick was used, while for measurements on the lines of the 1089 kev. transition, a source 2.5 mgm./cm.<sup>2</sup> thick was used in order to obtain better statistics in the measurement of the *L* line. The results quoted are the means of two separate determinations.

The intensities of the *K* conversion lines of the 677 and 1089 kev. transitions relative to the intensity of the *K* conversion line of the 412 kev. transition were also measured, using a 0.2 mgm./cm.<sup>2</sup> thick source for all measurements. The values found were  $(5.91 \pm 0.24) \times 10^{-3}$  and  $(2.41 \pm 0.03) \times 10^{-4}$  for the 676.5 kev. and 1088.9 kev. transitions respectively. These quantities, which are the means of two determinations made with different sources, are used in the determination of internal conversion coefficients in Section VI.

It is to be noted that the difference of the energies of the 1088.9 kev. and 676.5 kev. transitions, i.e.  $412.4 \pm 1.2$  kev., is in close agreement with the energy of the 411.77 kev. transition. It is accordingly believed that the latter transition is a crossover transition from a state in  $Hg^{198}$  at 1088.9 kev. to the ground state in  $Hg^{198}$ .

#### V. $\gamma$ -RAY INTENSITIES

The intensities of the 676.5 kev. and 1089 kev.  $\gamma$ -rays were measured by observing the *K* photoelectron lines from a thorium radiator, 8 mgm./cm.<sup>2</sup> thick, using the single lens spectrometer described in Section II. The source was made from three disks of pure gold, each 10 mgm./cm.<sup>2</sup> thick, 3 mm. in diameter. The gold foils were separated from each other by two disks of "superpure" aluminum of the same diameter and 0.009 in. thick, and the assembly mounted in a small cup at the end of a "superpure" aluminum rod, and covered with an aluminum disk 0.009 in. thick. The source and mounting were then irradiated in the Chalk River reactor to an activity of about 350 mc. A similar rod of "superpure" aluminum was irradiated along with the source, and examined afterwards to verify that activities were not formed in the rod material which would interfere with measurements made on the  $Au^{198}$  source. A disk of gold 0.2 mgm./cm.<sup>2</sup> thick and 4 mm. in diameter was also irradiated along with the intense source and an absolute determination of its activity made by coincidence counting. The activity of the intense source was then found by comparison with this source of known activity by  $\gamma$ -ray counting with a scintillation counter.

In order to determine the  $\gamma$ -ray intensities accurately from the measured intensities of the *K* photoelectron lines it was necessary to calibrate the spectrometer arrangement for intensities because of the variation of the photo-electron absorption cross section with energy. This was done at  $\gamma$ -ray energies of 412, 602, 794, 1172, 1332, and 1360 kev. by using sources of  $Au^{198}$ ,  $Cs^{134}$ , and  $Co^{60}$  of known activity. The  $Au^{198}$  source was the intense one described above. A  $Co^{60}$  source of the same geometrical size was calibrated against a  $Co^{60}$  standard. The  $\gamma$ -ray flux of energy 1360 kev. from a  $Cs^{134}$  source, also of the same geometrical size, was found by comparing the intensity of its *K* photoelectron line with the intensity of the *K* line due to the 1332 kev.  $\gamma$ -ray

from the  $\text{Co}^{60}$  source. The relative photoelectric absorption cross section for the two quanta was taken to be 1.06, and this value was later checked against the complete curve of effective relative photoelectric absorption cross section vs. quantum energy. The intensities of the 602 and 794 kev.  $\gamma$ -rays from  $\text{Cs}^{134}$ , relative to the 1360 kev.  $\gamma$ -ray, were taken to be  $33.4 \pm 1.7$  and  $32.4 \pm 1.7$  respectively. The latter value was obtained by direct comparison of the 794 and 1360 kev. quantum intensities using a  $\text{NaI}(\text{TI})$  scintillation spectrometer calibrated for intensity. The former value was then deduced assuming the order of emission of the 602 and 794 kev.  $\gamma$ -rays proposed by Waggoner *et al.* (41). These values\* are, however, not sensitive to the details of the disintegration scheme of  $\text{Cs}^{134}$ .

The  $K$  photoelectron lines of the 676.5 kev. and 1088.9 kev.  $\gamma$ -rays from  $\text{Au}^{198}$  are shown in Fig. 4. From the intensities of these lines, the  $\gamma$ -ray inten-

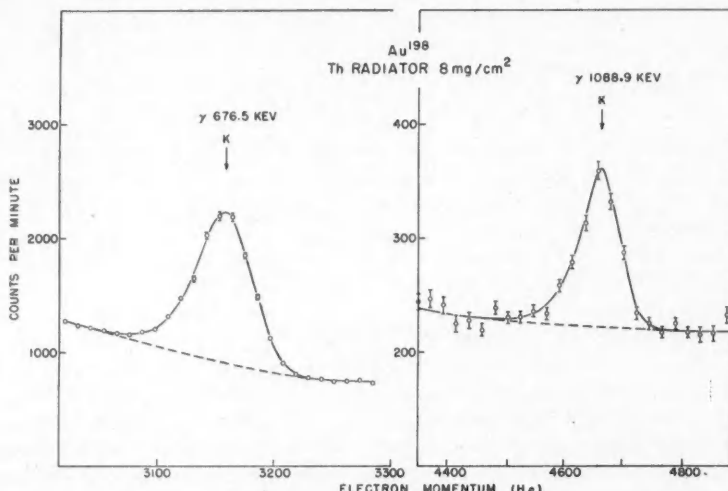


FIG. 4.  $K$  photoelectron lines of the 676.5 and 1088.9 kev.  $\gamma$ -ray transitions. The ordinates are the observed counting rates. The vertical bars represent standard deviations; where no vertical bars are shown, the standard deviations are less than the radii of the circles. The intensities of the photoelectron lines are proportional to the line areas divided by their corresponding momenta. The dashed curves give the shapes of the background under the lines as found by examining the spectrum with the thorium radiator removed.

sities relative to the 412 kev.  $\gamma$ -ray were found to be  $(8.42 \pm 0.56) \times 10^{-3}$  and  $(1.70 \pm 0.12) \times 10^{-3}$  for the 676.5 kev. and 1088.9 kev.  $\gamma$ -rays respectively. When allowance is made for the internal conversion of the 412 kev. transition ( $\alpha = 0.045$ ), the values found for the intensities of the transitions per disintegration,  $I$ , are:

\*In the earlier work (5, 42) the values used were 24.6 and 23.6 respectively. These were deduced from the ratio given by Waggoner *et al.* (41) for the intensity of the 1360 kev.  $\gamma$ -ray to the  $\beta$ -ray intensity, using a  $\beta$  branching ratio of 30/70. Accordingly the quantum intensities of the 676.5 and 1089 kev. transitions in  $\text{Hg}^{198}$  were underestimated by about 25% and 10% respectively, with corresponding overestimates of the conversion coefficients.

Energy of transition	<i>I</i>
676.5 kev.	$(8.20 \pm 0.56) \times 10^{-3}$
1088.9 kev.	$(1.63 \pm 0.12) \times 10^{-3}$

In deriving these values allowance is also made for internal conversion of the transitions as found in Sections IV and VI. The results quoted are the weighted means of three separate determinations using different  $Au^{198}$  sources for each determination.

#### VI. CONVERSION COEFFICIENTS

The  $K$  conversion coefficients,  $\alpha_K$ , have been determined for the 676.5 kev. and 1088.9 kev. transitions, utilizing the data of Sections IV and V along with the theoretical value (28) of  $\alpha_K$ , 0.0317, for the 412 kev. transition which is taken to be  $E2$  in character. There is no doubt as to this assignment for the 412 kev. transition since all experimenters have found this to be the case on the basis of the measured value of  $\alpha_K$  (6, 12, 13, 32, 35, 36, 39), the  $\alpha_K/\alpha_L$  ratio (6, 11, 12, 32, 35, 36, 37, 39), and the lifetime (9, 19, 21) of the transition. The conversion coefficients were found to be:

Energy of transition	$\alpha_K$
676.5 kev.	$0.0224 \pm 0.0019$
1088.9 kev.	$0.00450 \pm 0.00034$

The calculations of Rose (28) give the following values of  $\alpha_K$  for the different orders of multipolarity:

$\gamma$ -Ray energy	<i>E1</i>	<i>M1</i>	<i>E2</i>	<i>M2</i>	<i>E3</i>
676.5 kev.	0.0041	0.047	0.0111	0.103	0.0263
1088.9 kev.	0.00173	0.0148	0.00453	0.030	0.0097

It is seen that the measured value of  $\alpha_K$  for the 1088.9 kev. transition is consistent only with  $E2$  radiation, and since the ground state of  $Hg^{198}$  is almost certainly of even parity and zero spin, it follows that the state in  $Hg^{198}$  at 1088.9 kev. has even parity and spin 2. Because the state at 411.77 kev. also has even parity and spin 2, the 676.5 kev. transition involves no change in parity. It is therefore concluded from the measured value of  $\alpha_K$  that the radiation from the 676.5 kev. transition is a mixture of  $M1$  and  $E2$ , with relative intensities of  $(32 \pm 6)\%$   $M1$  and  $(68 \mp 6)\%$   $E2$ . This finding will be discussed further in Section VIII.

#### VII. SHAPE OF THE 1371 KEV. $\beta$ -SPECTRUM

It has been shown in Section VI that the states in  $Hg^{198}$  at 412 and 1089 kev. are both of even parity and spin 2. The  $\log f_{\text{tot}}$  of the 959 kev.  $\beta$ -transition is 7.4 and the spectrum has the allowed shape. Since the nuclear charge is high, these facts are consistent with a first forbidden  $\beta$ -ray transition (18). The

$\log f_{0\ell}$  value of the 283 kev.  $\beta$ -transition is 7.6 as determined from the measured  $\gamma$ -ray intensities (Section V), so that it too is expected to be a first forbidden transition. The parity of the ground state of  $\text{Au}^{198}$  is accordingly expected to be odd. By assigning the odd proton to a  $d$  state and the odd neutron to a  $p$  state, the same conclusion is reached from nuclear shell structure considerations. The spin of the ground state of  $\text{Au}^{198}$  must be 1, 2, or 3, all other possibilities being inconsistent with the spectral shapes and  $\log f_{0\ell}$  values of the 959 kev. and 283 kev.  $\beta$ -transitions. A spin of 1 would require that the 1371 kev. transition be first forbidden, which is inconsistent with the forbidden shape found for the spectrum and with the  $\log f_{0\ell}$  value of 11.7. A spin of 2 would require that the transition be first forbidden, which is inconsistent with the  $\log f_{0\ell}$  value, and it has also been found that the shape of the spectrum does not conform to the  $a$ -type (43) required by this assignment. A spin of 3 remains the only possibility consistent with all the experimental findings, and leads to the conclusion that the high energy  $\beta$ -spectrum is third forbidden.

The shape of the spectrum might therefore be expected to yield information as to the interaction form governing  $\beta$ -decay, and it has been studied with this end in view. The interaction Hamiltonian is written as  $\lambda_S H_S + \lambda_V H_V + \lambda_T H_T + \lambda_A H_A + \lambda_P H_P$ , where the subscripts  $S$ ,  $V$ ,  $T$ ,  $A$ , and  $P$  stand for scalar, vector, tensor, axial vector, and pseudoscalar. The  $\lambda$ 's are coupling constants and the  $H$ 's are as defined by Konopinski (14). The pseudoscalar term makes no appreciable contribution to a third order transition, and assuming the Fierz conditions (7), only the four interaction combinations  $VA$ ,  $ST$ ,  $SA$ , and  $VT$  are considered. The shape factors are taken from Greuling (10) and Pursey (25). The effect of the finite radius of the nucleus has been taken into account by an extension of the work of Rose and Holmes (29, 30) for  $Z = 83$ .

The nuclear matrix elements are of the form  $Q_{ijk}(\mathbf{a})$  defined by Greuling (10). The matrix elements which appear are those with  $\mathbf{a} = \mathbf{r}$ ,  $\mathbf{d} \times \mathbf{r}$ ,  $\mathbf{a}$ ,  $\beta\mathbf{r}$ ,  $\beta\mathbf{d} \times \mathbf{r}$ ,  $\beta\mathbf{a}$ . If  $\mathbf{a}$  and  $\mathbf{b}$  are any two of these vectors, it is known (17) that the ratio  $Q_{ijk}(\mathbf{a})/Q_{ijk}(\mathbf{b})$  is independent of  $i, j, k$  and is real or pure imaginary. In fact

$$Q_{ijk}(\mathbf{a})/Q_{ijk}(\mathbf{r}) = \rho i, \quad Q_{ijk}(\mathbf{d} \times \mathbf{r})/Q_{ijk}(\mathbf{r}) = \sigma i, \quad Q_{ijk}(\beta\mathbf{a})/Q_{ijk}(\mathbf{a}) = \tau$$

where  $\rho$ ,  $\sigma$ , and  $\tau$  are real. Also

$$Q_{ijk}(\beta\mathbf{r}) = -Q_{ijk}(\mathbf{r}) \quad \text{and} \quad Q_{ijk}(\beta\mathbf{d} \times \mathbf{r}) = -Q_{ijk}(\mathbf{d} \times \mathbf{r})$$

when small components of the wave functions are neglected in comparison with the large components.

Denoting the shape factor by  $C$ , which is proportional to  $(N/\eta^2 F) \cdot (E_0 - E)^{-2}$ , the quantity  $C^{1/2}$  is found from the experimental data at eight energy values. These are plotted in Fig. 5. The calculated values of  $C^{1/2}$  for each of the combinations  $VA$ ,  $ST$ ,  $SA$ , and  $VT$  were then plotted, normalizing all curves to the experimental value of  $C^{1/2}$  at 1200 kev. This procedure required estimates of the pertinent matrix elements and these were made using a special nuclear model based on nuclear shell theories. Since the ground state of  $\text{Au}^{198}$  has a spin of 3, it is indicated that the odd proton is in a  $d_{3/2}$  state and the odd neu-

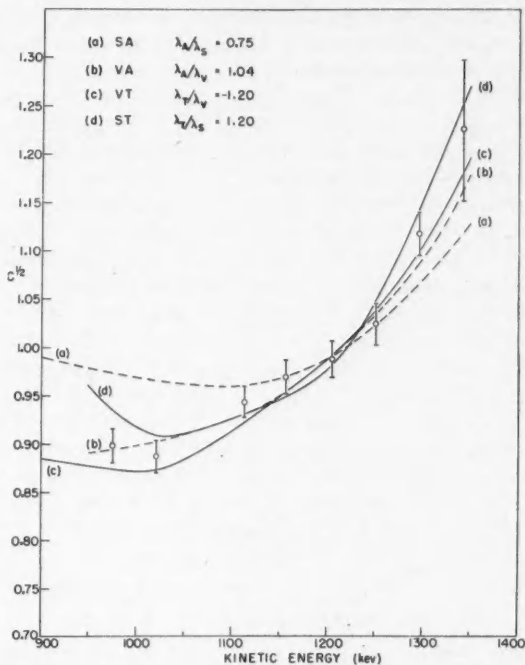


FIG. 5. The square root of the shape factor vs. electron kinetic energy. The circles represent the experimental data. The vertical bars represent standard deviations. Only the best fit for each of the combinations *SA*, *VA*, *VT*, *ST* is shown. For the various curves, the values of the parameters as defined in the text are:

(a) $\sigma = -4/3$ ;	(c) $\sigma = -4/3$ , $\rho = 4.94$ , $\tau = 4/3$ ;
(b) $\sigma = -4/3$ , $\rho = 4.5$ ;	(d) $\sigma = -4/3$ , $\rho = 1.9$ , $\tau = 4/3$ .

tron in a  $p_{3/2}$  state. A reasonable configuration is  $(d_{3/2})^8$  for the protons and  $(i_{13/2})^{12}p_{3/2}$  for the neutrons. It is only necessary to consider the state with  $M_i = 3$  in calculating the matrix elements (38). This requires  $m$  values of  $3/2$ ,  $1/2$ ,  $-1/2$  for the protons and  $3/2$  for the neutron. The one-particle transition is therefore from a  $p_{3/2}$  ( $m = 3/2$ ) state to a  $d_{3/2}$  ( $m = -3/2$ ) state.

The following values of the matrix element ratios were found:

$$\rho \sim 9/2, \quad \sigma = -4/3, \quad \tau = 4/3.$$

The value for  $\rho$  is highly approximate and may well be in error by a factor of two or more. The values of  $\sigma$  and  $\tau$  do not depend on the radial parts of the one-particle wave functions.

Using the above values of  $\sigma$  and  $\tau$  and various values of  $\rho$  in the neighborhood of  $9/2$ , attempts were made to fit the theoretical results to the experimental data. The other parameter in each case,  $\lambda_T/\lambda_S$ ,  $\lambda_A/\lambda_V$ ,  $\lambda_A/\lambda_S$ , or  $\lambda_T/\lambda_V$ , was adjusted to give the best possible fit. From the families of curves obtained only

those giving the best agreement with experiment are shown in Fig. 5, one for each of the interaction combinations *VA*, *ST*, *SA*, and *VT*. A brief discussion of these results is given in Section VIII.

### VIII. DISCUSSION

The measured value of  $\alpha_K$  for the 1089 kev.  $\gamma$ -ray transition is in excellent agreement with the theoretical value for *E2* radiation, and since this transition leads to the ground state, the radiation is identified as pure *E2* with certainty. It follows that the 1089 kev. state in  $\text{Hg}^{198}$  has spin 2 and even parity. The value of  $\alpha_K$  for the 677 kev.  $\gamma$ -ray, identifying this radiation as a mixture of *M1* and *E2*, is also consistent with the assignment of spin 2 and even parity to the 1089 kev. state. Recently, Schrader *et al.* (34) have investigated the angular

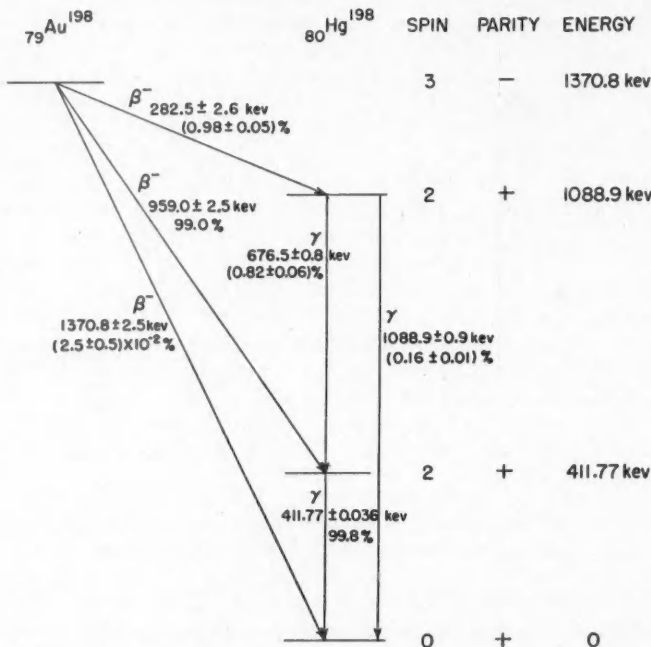


FIG. 6. Proposed disintegration scheme of  $\text{Au}^{198}$ . All energy measurements are based on the energy of  $411.77 \pm 0.036$  kev.  $\gamma$ -ray measured by Muller *et al.* (22).

correlation between the 677 kev. and 412 kev.  $\gamma$ -rays and have also found the 677 kev.  $\gamma$ -ray to be a mixture of *M1* and *E2*. They have found the mixture to be  $(40 \pm 5)\%$  *M1* and  $(60 \pm 5)\%$  *E2* as compared with the results  $(32 \pm 6)\%$  and  $(68 \mp 6)\%$  obtained in this investigation. Schiff and Metzger (33) have also studied the angular correlation and have estimated the mixture to be  $(30-50)\%$  *M1* and  $(70-50)\%$  *E2* radiation. The spin and parity assignments

found from these angular correlation experiments are in agreement with those given above.

The ratios  $\alpha_K/\alpha_L$  found in Section IV provide a further means of checking the multipolarity of the  $\gamma$ -rays. The result of  $6.3 \pm 0.5$  for the 1089 kev.  $\gamma$ -ray is in fair agreement with the extrapolated empirical curve of Goldhaber and Sunyar (8) for  $E2$  radiation which predicts a value of about 6.8. The result of  $5.7 \pm 0.5$  for the 677 kev.  $\gamma$ -ray is however not in agreement with the extrapolated curves for  $M1$  and  $E2$  which predict a value of  $\sim 7.1$  for 32%  $M1$  and 68%  $E2$  mixture. A mixture of 40%  $M1$  and 60%  $E2$  as found in the angular correlation experiments (33, 34) leads to a value of about 7.2. It is to be noted, however, that the extrapolation of the curves is rather uncertain.

The investigation of the shape of the 1371 kev.  $\beta$ -transition suffers from the severe limitation that only that portion of the spectrum above 959 kev. is available for study, owing to the presence of the intense 959 kev. spectrum. It can only be said that the combination  $SA$  is in definite disagreement with experiment. For the other three combinations,  $VA$ ,  $VT$ , and  $ST$ , fairly good fits to the experimental data can be obtained with reasonable values of the parameters. As indicated by other experiments (23, 31), the combination  $VA$  may be rejected since it contains the axial vector rather than the tensor form for the Gamow-Teller part of the interaction, but the present data nevertheless do not provide a clear-cut preference for either one of the remaining two interaction combinations.

#### ACKNOWLEDGMENT

The authors wish to thank Dr. R. E. Bell and Dr. R. L. Graham for the standardization of  $Au^{198}$  sources used in the experiments, and Messrs. R. C. Hawkings and W. F. Merritt for the loan of a standard  $Co^{60}$  source.

#### REFERENCES

1. BROSI, A. R., KETELLE, B. H., ZELDES, H., and FAIRSTEIN, E. Phys. Rev. 84: 586. 1951.
2. CAVANAGH, P. E. Phys. Rev. 82: 791. 1951.
3. CAVANAGH, P. E., TURNER, J. F., BOOKER, D. V., and DUNSTER, H. J. Proc. Phys. Soc. (London), A, 64: 13. 1951.
4. DZHELEJOV, B. S., BASHILOV, A. A., ZOLOTAVIN, A. V., and ANTON'IVA, N. M. U.S.S.R. Acad. Sci. Repts. 64(6). 1949.
5. ELLIOTT, L. G. and WOLFSON, J. L. Phys. Rev. 82: 333. 1951.
6. FAN, C. Y. Phys. Rev. 81: 300A. 1951.
7. FIERZ, M. Z. Physik, 104: 553. 1937.
8. GOLDHABER, M. and SUNYAR, A. W. Phys. Rev. 83: 906. 1951.
9. GRAHAM, R. L. and BELL, R. E. Phys. Rev. 84: 380. 1951.
10. GREULING, E. Phys. Rev. 61: 568. 1942.
11. HILL, R. D. and MIHELICH, J. W. Phys. Rev. 79: 275. 1950.
12. HUBER, O., HUMBEL, F., SCHNEIDER, H., and DE SHALIT, A. Helv. Phys. Acta, 25: 3. 1952.
13. HUBERT, P. Compt. rend. 232: 2201. 1951.
14. KONOPINSKI, E. J. Revs. Mod. Phys. 15: 209. 1943.
15. LANGER, L. M. and PRICE, H. C., JR. Phys. Rev. 76: 186A; 641. 1949.
16. LEVY, P. W. and GREULING, E. Phys. Rev. 75: 819. 1949.
17. LONGMIRE, C. L. and MESSIAH, A. M. L. Phys. Rev. 83: 464. 1951.
18. MAHMOUD, H. M. and KONOPINSKI, E. J. Phys. Rev. 88: 1266. 1952.
19. MALMFORS, K. G. Arkiv Fysik, 6: 49. 1952.
20. MIMS, W. and HALBAN, H. Proc. Phys. Soc. (London), A, 64: 311. 1951.
21. MOON, P. B. and DAVEY, W. Birmingham Conference on Nuclear Physics, Birmingham, England, July 1953.
22. MULLER, D. E., HOYT, H. C., KLEIN, D. J., and DUMOND, J. W. M. Phys. Rev. 88: 775. 1952.

23. PETSCHEK, A. G. and MARSHAK, R. E. *Phys. Rev.* 85: 698. 1952.
24. PRINGLE, R. W. and STANDIL, S. *Phys. Rev.* 80: 762. 1950.
25. PURSEY, D. *Phil. Mag.* 42: 1193. 1951.
26. RENARD, G. A. *Compt. rend.* 228: 387. 1949.
27. RIDGWAY, S. L. *Phys. Rev.* 78: 821. 1950.
28. ROSE, M. E., GOERTZEL, G. H., and PERRY, C. L. ORNL Report 1023. 1951.
29. ROSE, M. E. and HOLMES, D. K. *Phys. Rev.* 83: 190. 1951.
30. ROSE, M. E. and HOLMES, D. K. ORNL Report 1022. 1951.
31. RUSTAD, B. M. and RUBY, S. L. *Phys. Rev.* 89: 880. 1953.
32. SAXON, D. and HELLER, R. *Phys. Rev.* 75: 909. 1949.
33. SCHIFF, D. and METZGER, F. R. *Phys. Rev.* 90: 849. 1953.
34. SCHRADER, C. D., NELSON, E. B., and JACOBS, J. A. *Phys. Rev.* 90: 159. 1953.
35. SHAHTALOV, L. Y. *Zhur. Eksp. i Teoret. Fiz.* 19: 633. 1949.
36. SIEGBAHN, K. and HEDGRAN, A. *Phys. Rev.* 75: 523. 1949.
37. SIMONS, L. *Phys. Rev.* 86: 570. 1952.
38. SMITH, A. M. *Phil. Mag.* 43: 915. 1952.
39. STEFFEN, R. M., HUBER, O., and HUMBEL, F. *Helv. Phys. Acta*, 22: 167. 1949.
40. STUMP, R. and FRANKEL, S. *Phys. Rev.* 79: 243A. 1950.
41. WAGGONER, M. A., MOON, M. L., and ROBERTS, A. *Phys. Rev.* 80: 420. 1950.
42. WOLFSON, J. L. and ELLIOTT, L. G. *Proc. Roy. Soc. Can.* 46: 142. 1952.
43. WU, C. S. *Revs. Mod. Phys.* 22: 386. 1950.

# ON THE NUSSELT MODULUS AS A FUNCTION OF FRICTION FACTOR, REYNOLDS AND PRANDTL MODULI, FOR HEAT TRANSFER TO A FLUID FLOWING TURBULENTLY THROUGH A TUBE OF CIRCULAR SECTION<sup>1</sup>

By A. W. MARRIS<sup>2</sup>

## ABSTRACT

Theoretical expressions for the Nusselt modulus and radial temperature distribution in terms of Reynolds number, Prandtl number, the ratio  $k$  of the eddy diffusivities for heat and momentum, and the friction factor are developed for the case of heat transfer from a tube of circular section to a fluid flowing turbulently through it. The results, appropriate to fluids with Prandtl numbers greater than  $1/2k$ , are derived on the assumption of the constancy of fluid properties and require a linear longitudinal temperature gradient in the tube itself. They enable the effect of the insulating "laminar" and "buffer" layers adjacent to the tube wall to be demonstrated at various Prandtl numbers and are appropriate for correlation with experiment for the investigation of the constancy or otherwise of the ratio of the eddy diffusivities for heat and momentum implicit in the momentum transfer analogy.

A similar result is worked out on the vorticity transfer analogy for the particular case of Prandtl number equal to  $1/k'$  and is found to be invalid for such a configuration. Here  $k'$  is the ratio of the eddy diffusivities for heat and vorticity.

## 1. SUMMARY OF NOMENCLATURE

$\rho$  = mass density of fluid at point  $P$  in fluid.  
 $\bar{P}$  = mean pressure at  $P$ .  
 $z$  = axial distance of  $P$ .  
 $r$  = radial distance of  $P$ .  
 $r_w$  = radius of tube.  
 $u$  = velocity of fluid passing over  $P$ .  
 $\mu$  = viscosity of fluid at  $P$ .  
 $\nu$  =  $\mu/\rho$  = kinematic viscosity of fluid at  $P$ .  
 $t$  = temperature at point  $P$ .  
 $c$  = specific heat of fluid at constant pressure.  
 $s$  = molecular conductivity of fluid.  
 $a$  =  $s/c\rho$  = thermal diffusivity of fluid.  
 $\epsilon_M$  = eddy diffusivity for momentum defined by

$\epsilon_M \partial u / \partial r = - u_r u_z$ ,  $u_r$  and  $u_z$  being the turbulent velocity fluctuations, or by  $\epsilon_M = l_M^{-2} \partial u / \partial r$ ,  $l_M$  being the "mixing length" for momentum transfer.  $\epsilon_M$  may be regarded as the effective increase in kinematic viscosity due to turbulence.

$\epsilon_H$  = eddy diffusivity for heat defined by  $\epsilon_H \partial t / \partial r = - u_r t'$ ,  $t'$  being the turbulent temperature fluctuation, or by  $\epsilon_H = l_H^{-2} \partial u / \partial r$ ,  $l_H$  being the "mixing length" for heat transfer. Again  $\epsilon_H$  may be regarded as the effective increase in thermal diffusivity due to turbulence.

$$k = \epsilon_H / \epsilon_M.$$

<sup>1</sup> Manuscript received September 21, 1953.

Work carried out at the School of Engineering, University College Auckland, Auckland, New Zealand.

<sup>2</sup> Lecturer in Physics, University of British Columbia, Vancouver, B.C.

$\epsilon_v$  = eddy diffusivity for vorticity, the virtual viscosity due to turbulence on vorticity transfer theory, and may be defined by  $\epsilon_v \frac{1}{r} \frac{\partial}{\partial r} \left( r \frac{\partial u}{\partial r} \right) = \bar{u}_r \xi'$

where  $\xi'$  is the turbulent vorticity fluctuation.

$$k' = \epsilon_H / \epsilon_v.$$

$h$  = heat transfer coefficient for inside surface of tube wall.

$q_w$  = heat flow per unit time normal to wall surface.

$A_w$  = area of wall surface across which  $q_w$  flows.

$A$  =  $2\pi r z$  = area of cylindrical surface in fluid across which heat flows.

$t_w$  = temperature of wall surface.

$$t_m = \text{"mixed" temperature of fluid defined by } t_m = \int_0^{r_w} u r t dr / \int_0^{r_w} r dr.$$

$$u_m = \text{mean velocity of flow, defined by } u_m = \int_0^{r_w} u r dr / \int_0^{r_w} r dr.$$

$$f = \text{Fanning friction factor} = - \frac{r_w}{\rho u_m^2} \frac{\partial \bar{P}}{\partial z}.$$

$$\tau_w = \text{shear between wall and fluid defined by } - \frac{1}{\rho} \frac{\partial \bar{P}}{\partial z} = \frac{2\tau_w}{\rho r_w}.$$

$$Re = \text{Reynolds' modulus} = 2r_w u_m / \nu.$$

$$U = \text{nondimensional velocity} = u / \sqrt{\frac{\tau_w}{\rho}} = \frac{u}{u_m} \sqrt{\frac{2}{f}}.$$

$$x = r / r_w = \text{nondimensional distance from axis.}$$

$$Q = Re \sqrt{f/8}.$$

$$y = Q(1 - x) = \text{nondimensional distance from tube wall.}$$

$$\alpha = \text{value of } y \text{ stipulating extremity of laminar layer.}$$

$$\beta = \text{value of } y \text{ stipulating extremity of buffer layer.}$$

$$\gamma = \alpha[1 - \log(\alpha/\beta)].$$

= value of  $y$  stipulating extremity of laminar layer when buffer layer is omitted.

$K, L, M, N$  = constants in equations for velocity distributions.

$Nu = \text{Nusselt modulus} = 2h r_w / s.$

$Pr = \text{Prandtl modulus} = c\rho\nu / s = c\mu / s.$

$P = kPr.$

$P' = k'Pr.$

## 2. INTRODUCTION

Much of the recent theoretical work on the problems of heat transfer by a turbulently flowing stream has been based on the assumption of a formal analogy between heat transfer and momentum transfer. In Reynolds' modification for turbulent flow of the Navier-Stokes equations there arises a quantity  $\epsilon_m$ , the eddy diffusivity for momentum, an additional "turbulent" viscosity; likewise in the equations for heat transfer (equations of similar form), there

arises  $\epsilon_H$ , the eddy diffusivity for heat, an addition to the molecular thermal diffusivity occasioned by turbulence. The solution of the heat transfer problem on the basis of analogy necessarily requires a relationship to be assumed between the quantities  $\epsilon_H$  and  $\epsilon_M$ . If one sets  $\epsilon_H/\epsilon_M = k$  then the constancy of the quantity  $k$  is a measurement of the validity of the analogy. It is remembered that momentum is a vector quantity whereas heat is a scalar.

Previous authors employing the momentum transfer analogy, von Karman (6), Boelter (1), Martinelli (1, 6), Lyon (5), have each set  $k = 1$ , however the theoretical investigation of H. Reichardt (8) of turbulent heat transfer from a flat plate and in a tube indicated that if  $k$  was computed from the measured temperature profiles it would have some value between 1.4 and 1.5. The temperature measurements of Sheppard (9) indicated a value 1.6 for this quantity; meanwhile measurements of heat transfer in wakes yield a value 2. However, it is known that the momentum transfer theory of turbulence does not predict the correct velocity distribution in wakes; but that the vorticity transfer theory propounded by G. I. Taylor (11, 12) yields satisfactory results. So the question arises as to whether vorticity transfer analogy considerations would yield better consistency. It is known however that the vorticity transfer theory breaks down in the neighborhood of solid boundaries.

In this paper, concerned with the heat transfer from a tube to a fluid flowing turbulently through the tube under the prescribed condition that at any point of the fluid the longitudinal temperature gradient is independent of the radial position of the point, i.e.  $\partial t/\partial z = \partial t_w/\partial z$  (see nomenclature), the Nusselt modulus and temperature distribution are expressed in terms of the friction factor  $f$ , a quantity  $Q$  equal to  $Re\sqrt{f/8}$ ,  $Re$  being the Reynolds number, and  $P$ , the product of the Prandtl number and the ratio  $k$ . Expressions are obtained first on the momentum transfer analogy for all  $P$  greater than  $\frac{1}{2}$ , and then on the vorticity transfer analogy for the particular case  $P' = 1$ . Here  $P' = k'Pr$  where  $k'$  is the ratio of the eddy diffusivities for heat and vorticity.

It is found that the requisite integrals admit exact evaluation over the complete velocity distribution consisting of a "laminar" adjacent-to-wall region, a semiturbulent "buffer-layer", and a fully turbulent core. Martinelli's device (6) of taking the velocity at a given point as equal to the mean flow velocity as a first approximation is avoided as is the series approximation to the logarithmic velocity distribution employed by Reichardt (8).

It appears that the vorticity transfer analogy cannot give a reasonable result for the particular configuration considered so that attention is refocused on the momentum transfer analogy.

Assuming constancy of fluid property values throughout the tube, the results are appropriate for correlation with experimental results for infinitely low heat transfer rates, for example with the work of Eagle and Ferguson for water (2), so that the constancy or otherwise of the ratio  $\epsilon_H/\epsilon_M$  may be further studied.

The results yield quantitative information concerning the heat "barrier" effect of von Karman's "buffer-layer" between the laminar surface layer

and the turbulent core, at various values of the Reynolds and Prandtl moduli, and indicate the magnitudes of errors likely to be introduced by uncertainties in the "near-to-wall" velocity distribution.

The temperature distribution formula predicts the zero temperature gradient at the tube axis as found experimentally by Sheppard (9).

### 3. GENERAL INTEGRALS FOR $(t_w - t_s)/(t_w - t_m)$ AND $Nu_f$ DERIVED FROM THE MOMENTUM TRANSFER ANALOGY

On the statistical theory of turbulence of Reynolds for which momentum and temperature are transferable properties the respective hydrodynamical equations representing flow of fluid through a pipe of circular section at a large distance from the end, and for heat transfer through the turbulent fluid can be written

$$[1] \quad \frac{1}{\rho} \frac{\partial \bar{P}}{\partial z} = \frac{1}{r} \frac{\partial}{\partial r} \left[ r(\epsilon_M + \nu) \frac{\partial u}{\partial r} \right],$$

$$[2] \quad u \frac{\partial t}{\partial z} = \frac{1}{r} \frac{\partial}{\partial r} \left[ r(\epsilon_H + a) \frac{\partial t}{\partial r} \right].$$

Equations [1] and [2] indicate the nature of the eddy diffusivities  $\epsilon_H$  and  $\epsilon_M$  as "turbulent additions" to the molecular thermal diffusivity and kinematic viscosity respectively.

Heat is flowing radially into the fluid from the internal wall of the tube and is taken away as the heated fluid moves on down the tube. The heat transfer coefficient  $h$  is defined by the equation

$$[3] \quad h = \frac{q_w}{A_w(t_w - t_m)}$$

so that

$$[4] \quad Nu = \frac{2hr_w}{s} = \frac{2q_w r_w}{A_w s(t_w - t_m)}.$$

Following Lyon (5) the ratio  $(t_w - t)/(t_w - t_m)$  and the Nusselt modulus are expressed as iterated integrals. The suffixes 1, 2, 3 refer to current positions in the fluid.

A heat balance on an annulus of fluid of radius  $r$  gives

$$[5] \quad u_1 A_1 \rho c \frac{\partial t}{\partial z} = \frac{\partial q_1}{\partial r_1} dr_1$$

so that using [2]

$$\frac{1}{A_1 c \rho} \frac{\partial q_1}{\partial r_1} = \frac{1}{r_1} \frac{\partial}{\partial r_1} \left[ r_1(\epsilon_H + a) \frac{\partial t}{\partial r_1} \right]$$

which, since  $q_1 = 0$  at  $r_1 = 0$ , integrates to

$$[6] \quad \frac{q_1}{A_1 c \rho} = \frac{q_1}{A_w c \rho x} = (\epsilon_H + a) \frac{\partial t}{\partial r_1}.$$

Again by [5]

$$q_2 = c \rho \frac{\partial t}{\partial z} \int_0^{r_1} u_1 A_1 dr_1$$

and

$$q_w = c\rho \frac{\partial t}{\partial z} \int_0^{r_w} u_1 A_1 dr_1 = c\rho u_m \frac{\partial t}{\partial z} \int_0^{r_w} A_1 dr_1$$

so that

$$[7] \quad q_2 = q_w \int_0^{r_w} \frac{u_1}{u_m} A_1 dr_1 \Big/ \int_0^{r_w} A_1 dr_1 = 2q_w \int_0^{x_2} \frac{u_1}{u_m} x_1 dx_1.$$

By [6] and [7]

$$\frac{\partial t}{\partial r_2} = \frac{2q_w}{c\rho(\epsilon_H + a) x_2 A_w} \int_0^{x_2} \frac{u_1}{u_m} x_1 dx_1$$

so that

$$[8] \quad t_w - t_2 = \frac{2r_w q_w}{s A_w} \int_{x_2}^1 \frac{a}{(\epsilon_H + a) x_2} \int_0^{x_2} \frac{u_1}{u_m} x_1 dx_1 dx_2,$$

$$[9] \quad t_w - t_m = \frac{4r_w q_w}{A_w} \int_0^1 \frac{u_3}{u_m} x_3 \int_{x_3}^1 \frac{1}{c\rho(\epsilon_H + a) x_2} \int_0^{x_2} \frac{u_1}{u_m} x_1 dx_1 dx_2 dx_3,$$

$$[10] \quad \text{Nu} = \frac{1}{2} \Big/ \left[ \int_0^1 \frac{u_3}{u_m} x_3 \int_{x_3}^1 \frac{a}{(\epsilon_H + a) x_2} \int_0^{x_2} \frac{u_1}{u_m} x_1 dx_1 dx_2 dx_3 \right].$$

Expressing the equations for steady motion of fluid as

$$[11] \quad \tau = x\tau_w,$$

$$[12] \quad \sqrt{(\tau_w/\rho)} = u_m \sqrt{(f/2)},$$

nondimensional velocity and distance from tube wall are defined thus:

$$[13] \quad U = \frac{u}{u_m} \sqrt{\frac{2}{f}},$$

$$[14] \quad y = Q(1 - x)$$

$$[15] \quad \text{where} \quad Q = \text{Re} \sqrt{(f/8)}.$$

Equation [1], which can be written

$$[16] \quad \frac{2\tau_w}{\rho r_w} = - \frac{1}{r} \frac{\partial}{\partial r} \left[ r(\epsilon_M + \nu) \frac{\partial U}{\partial r} \right],$$

yields, on integration and transformation,

$$[17] \quad \frac{\epsilon_M}{\nu} = - \left( Qx + \frac{dU}{dx} \right) \Big/ \frac{dU}{dx}.$$

Writing

$$[18] \quad \frac{a}{\epsilon_H + a} = \left( \frac{\epsilon_H}{a} + 1 \right)^{-1} = \left( P \frac{\epsilon_M}{\nu} + 1 \right)^{-1}$$

where  $\text{Pr} = c\mu/s = \nu/a$ , the Prandtl modulus, and

$$[19] \quad P = k\text{Pr},$$

$$[20] \quad \frac{a}{\epsilon_H + a} = \left[ (1 - P) - \frac{PQx}{dU/dx} \right]^{-1}.$$

Using [13] and [20] the basic equations [8], [9], and [10] now become

$$[21] \quad \frac{t_w - t_3}{t_w - t_m} = \text{Nu} \sqrt{\frac{f}{2}} \int_{x_1}^1 x_2^{-1} \left[ (1 - P) - \frac{PQx_2}{dU/dx_2} \right]^{-1} \int_0^{x_3} U_1 x_1 dx_1 dx_2$$

and

$$[22] \quad \frac{1}{\text{Nu} f} = \int_0^1 U_3 x_3 \int_{x_1}^1 x_2^{-1} \left[ (1 - P) - \frac{PQx_2}{dU/dx_2} \right]^{-1} \int_0^{x_3} U_1 x_1 dx_1 dx_2 dx_3.$$

The integrals [21] and [22] have to be evaluated for the appropriate radial velocity distribution  $U = U(x)$ .

Following the work of Nikuradse (7), Stanton and Pannell (10, 4), and von Karman, the velocity distribution will be considered in the general form

$$[23] \quad \begin{cases} U = U'(x) = Q(1 - x) \text{ for } 1 - \alpha > x > 1 - (\alpha/Q), \\ \quad \text{the "laminar", adjacent-to-wall region;} \\ U = U''(x) = K + L \log Q(1 - x), \text{ for } 1 - (\alpha/Q) > x > 1 - (\beta/Q), \\ \quad \text{the "buffer-layer";} \\ U = U'''(x) = M + N \log Q(1 - x) \text{ for } 1 - (\beta/Q) > x > 0, \\ \quad \text{the turbulent core;} \end{cases}$$

where between the several constants  $\alpha$ ,  $\beta$ ,  $K$ ,  $L$ ,  $M$ , and  $N$  the boundary relations

$$[24] \quad L = \alpha; \quad K = \alpha(1 - \log \alpha); \quad M + N \log \beta = \alpha[1 - \log(\alpha/\beta)] = \gamma$$

hold. They express continuity of  $U$  and  $dU/dy$  at  $y = \alpha$ , the boundary between laminar and buffer layers, and continuity of  $U$  only at  $y = \beta$ , the boundary between the buffer layer and the turbulent core. The relations [24] used in conjunction with experimental results of Nikuradse etc. yield the numerical values  $\alpha = 5$ ,  $\beta = 30$ ,  $K = -3.05$ ,  $L = 5$ ,  $M = 5.5$ ,  $N = 2.5$ ,  $\gamma = 14$ .

#### 4. EVALUATION OF INTEGRALS

Equations [21] and [22] may be written

$$[25] \quad \frac{t_w - t_3}{t_w - t_m} = \text{Nu} \sqrt{\frac{f}{2}} I_3,$$

$$[26] \quad 1/\text{Nu} f = I$$

where

$$[27] \quad I_3 = \int_{x_1}^1 x_2^{-1} \left[ (1 - P) - \frac{PQx_2}{dU/dx_2} \right]^{-1} \int_0^{x_3} U_1 x_1 dx_1 dx_2$$

and

$$[28] \quad I = \int_0^1 U_3 x_3 I_3 dx_3.$$

Before proceeding to the general case the particular case of laminar flow throughout the tube section is considered.

In this case  $\epsilon_H = \epsilon_M = 0$  and  $U = \frac{u}{u_m} \sqrt{\frac{2}{f}} = \sqrt{\frac{8}{f}} (1 - x^2)$  throughout the range  $0 < x < 1$ .  
Thus

$$[29] \quad I_3 = \sqrt{\frac{8}{f}} \int_{x_1}^1 \frac{1}{x_2} \int_0^{x_2} (x_1 - x_2^2) dx_1 dx_2 = \sqrt{\frac{8}{f}} \frac{(3 - 4x_3^2 + x_3^4)}{16}$$

and

$$[30] \quad I = \frac{8}{f} \int_{x_1}^1 \frac{(x_3 - x_3^2)(3 - 4x_3^2 + x_3^4)}{16} dx_3 = \frac{11}{48f}$$

so that

$$[31] \quad \text{Nu} = \frac{48}{11} = 4.364$$

and

$$[32] \quad \frac{t_w - t}{t_w - t_m} = \frac{6}{11} (3 - 4x^2 + x^4).$$

The general results valid for  $P > 1/2[1 - (\beta/Q)] > 1/2[1 - (\alpha/Q)] > \frac{1}{2}$  will now be derived.

The results will involve convergent infinite series of the form  $\sum F_n(PQ)/Q^n$  and the question arises as to the lowest power of  $1/Q$  that can be neglected without causing appreciable error. For the simpler case of buffer layer omitted, a result valid over the restricted range  $\frac{1}{2} < P < 1$  was worked to  $O(1/Q^2)$ . It is found that in this range, that is for  $P \ll O(Q)$ , the error involved in neglecting terms  $O(1/Q^2)$  was about 1% at  $Q = 300$  corresponding to Reynolds' number  $10^4$  and about 0.2% at Reynolds' number  $5 \times 10^4$ .

For the sake of avoiding undue arithmetical complication, the derivation for all three layers is restricted to  $O(1/Q)$ . Inaccuracies may exist in the region  $P = O(Q)$  owing to the fact that certain terms of the form  $P/Q^2$  are neglected, but it is considered that uncertainties in the near-to-wall velocity distribution very effective at the higher Prandtl numbers will have vitiated the results anyhow before these values are reached.

The problem is that of evaluating the integrals [27] and [28] for the velocity distribution given by the equations [23] and [24].

Writing  $I_2(x_2) = \int_0^{x_2} U x_1 dx_1$ , integrating, and using the relations [24], the

following results are obtained.

(a) For  $0 < x_2 < 1 - (\beta/Q)$

$$[33] \quad \begin{aligned} I_2(x_2) &= I_2'''(x_2) = \int_0^{x_2} [M + N \log Q + N \log (1 - x_1)] x_1 dx_1 \\ &= \left( \frac{2\gamma - N}{4} - \frac{N}{2} \log \frac{\beta}{Q} \right) x_2^2 - \frac{N}{2} x_2 - \frac{N}{2} (1 - x_2^2) \log (1 - x_2). \end{aligned}$$

(b) For  $1 - (\beta/Q) < x_2 < 1 - (\alpha/Q)$

$$I_2(x_2) = I_2''(x_2) = \int_0^{1-(\beta/Q)} [M + N \log Q + N \log(1 - x_1)] x_1 dx_1 \\ + \int_{1-(\beta/Q)}^{x_2} [K + L \log Q + L \log(1 - x_1)] x_1 dx_1 \\ [34] \quad = (\frac{1}{4}\alpha - \frac{1}{2}\alpha) x_2^2 - \frac{1}{2}\alpha x_2 - \frac{1}{2}\alpha(1 - x_2^2) \log(1 - x_2) + E(Q)$$

$$[35] \quad \text{where} \quad E(Q) = (\alpha - N) \left[ \frac{1}{2} \log \frac{\beta}{Q} + \frac{3}{4} - \frac{\beta}{Q} \right].$$

(c) For  $1 - (\alpha/Q) < x_2 < 1$

$$I_2(x_2) = I_2'(x_2) = \int_0^{1-(\beta/Q)} [M + N \log Q + N \log(1 - x_1)] x_1 dx_1 \\ + \int_{1-(\beta/Q)}^{1-(\alpha/Q)} [K + L \log Q + L \log(1 - x_1)] x_1 dx_1 + \int_{1-(\alpha/Q)}^{x_2} Q(1 - x_1) x_1 dx_1 \\ [36] \quad = \frac{1}{6} Q(3x_2^2 - 2x_2^3) + F(Q)$$

$$[37] \quad \text{where} \quad F(Q) = -\frac{N}{2} \log \frac{\beta}{Q} - \frac{Q}{6} + \frac{2\gamma - 3N}{4} + \frac{\alpha^2 - 2(\alpha - N)\beta}{2Q}.$$

The function

$$I_3 = \int_{x_2}^1 \left[ x_2(1 - P) - \frac{PQx_2}{dU/dx_2} \right]^{-1} I_2 dx_2$$

may now be evaluated.

Again the range is divided into three intervals.

(d) For  $1 - (\alpha/Q) < x_3 < 1$  where  $dU/dx_2 = -Q$

$$I_3(x_3) = I_3'(x_3) = \int_{x_2}^1 \frac{\frac{1}{6}Q(3x_2^2 - 2x_2^3) + F(Q)}{Px_2^2[1 + (1 - P)/Px_2]} dx_2 \\ [38] \quad \left\{ \begin{array}{l} = \frac{Q}{6P} \left[ (1 - x_3) \left( \frac{2}{P} - x_2 \right) + \frac{(1 - P)(P + 2)}{P^2} \log x_3 \right] \\ \quad + \frac{1}{1 - P} \left[ \frac{2Q - 3PQ}{6P^3} + G(Q) \right] [\log [1 - P(1 - x_3)] - \log x_3] \\ \quad \text{where } G(Q) = F(Q) + \frac{Q}{6} \\ = -\frac{N}{2} \log \frac{\beta}{Q} + \frac{2\gamma - 3N}{4} + \frac{\alpha^2 - 2(\alpha - N)\beta}{2Q} + O\left(\frac{1}{Q^3}\right). \end{array} \right.$$

If  $P$  becomes greater than  $Q/\alpha$ , then the term  $\log [1 - P(1 - x_3)]$  becomes undefined over a certain subinterval of the range  $1 > x_3 > 1 - (\alpha/Q)$  for which it is required. It will be seen below that to  $O(1/Q)$  the term involving  $I_3'(x_3)$  contributes nothing to the value of the Nusselt modulus. So if  $P > Q/\alpha$  but  $< Q/\theta$  say where  $\theta < \alpha$ , one can integrate over the subregion  $1 - (\theta/Q) < x_3 < 1$  of the laminar layer instead of over the whole layer and to  $O(1/Q)$

the result will be unaltered. This is clear also from the physical fact of relatively low heat transfer over regions of laminar flow.

(e) For  $1 - (\beta/Q) < x_3 < 1 - (\alpha/Q)$

$$I_3(x_3) = I_3''(x_3) = \int_{x_2}^1 x_2^{-1} \left[ (1-P) - \frac{PQx_2}{dU/dx_2} \right]^{-1} I_2 dx_2$$

[39] =  $\int_{x_2}^{1-(\alpha/Q)} \frac{E(Q) + \alpha[\frac{1}{4}(1-2 \log(\alpha/Q))x_2^2 - \frac{1}{2}x_2 - \frac{1}{2}(1-x_2^2) \log(1-x_2)]}{x_2[(1-P) - (PQ/\alpha)x_2(1-x_2)]} dx_2$ 
 $+ \int_{1-(\alpha/Q)}^1 \frac{\frac{1}{6}Q(3x_2^2 - 2x_2^3) + F(Q)}{PQx_2^2[1 + (1-P)/Px_2]} dx_2$

by [34] and [36] and since  $dU/dx_2 = -Qx_2$  in the interval  $1 - (\alpha/Q) \leq x_3 \leq 1$  and  $dU/dx_2 = -L/(1-x_2) = -\alpha/(1-x_2)$  in the interval  $1 - (\beta/Q) \leq x_3 \leq 1 - (\alpha/Q)$ .

Putting  $x_3 = 1 - (\alpha/Q)$  in [38] it is found that

$$[40] \quad \int_{1-(\alpha/Q)}^1 \frac{\frac{1}{6}Q(3x_2^2 - 2x_2^3) + F(Q)}{PQx_2^2[1 + (1-P)/Px_2]} dx_2$$
 $= \frac{\alpha}{Q} \left[ -\frac{N}{2} \log \frac{\beta}{Q} + \frac{2\gamma - 3N}{4} \right] + O\left(\frac{1}{Q^2}\right).$

To evaluate

$$\int_{x_2}^{1-(\alpha/Q)} \frac{E(Q) + \alpha[\frac{1}{4}(1-2 \log(\alpha/Q))x_2^2 - \frac{1}{2}x_2 - \frac{1}{2}(1-x_2^2) \log(1-x_2)]}{x_2[(1-P) + (PQ/\alpha)x_2(1-x_2)]} dx_2$$

the denominator should be factorized, thus

$$x_2 \left[ (1-P) + \frac{PQ}{\alpha} x_2 (1-x_2) \right] = \frac{PQ}{\alpha} (\lambda - x_2)(\mu + x_2)$$

where  $\lambda = 1 + \frac{\alpha(1-P)}{PQ} + O\left(\frac{1}{Q^2}\right)$ ,

$$\mu = \frac{\alpha(1-P)}{PQ} + O\left(\frac{1}{Q^2}\right),$$

and the integral resolved into partial fractions.

However, since  $P \gg 1/Q$ , it is clear that a close approximation to the answer will be obtained by writing the denominator  $x_2[(1-P) + (PQ/\alpha)x_2 \times (1-x_2)]$  as  $(PQ/\alpha)x_2^2(1-x_2)$ , a device which simplifies the analysis considerably. The outline of the more exact reduction is given in the appendix, and it is found that the result obtained by the above device is correct to  $O(1/Q)$  except for two inconsequential terms.

Writing the integral then in this form, one has

$$\frac{\alpha}{PQ} \int_{x_2}^{1-(\alpha/Q)} \frac{E(Q) + \alpha[\frac{1}{4}(1-2 \log(\alpha/Q))x_2^2 - \frac{1}{2}x_2 - \frac{1}{2}(1-x_2^2) \log(1-x_2)]}{x_2^2(1-x_2)} dx_2$$
 $= \frac{\alpha}{PQ} E(Q) \int_{x_2}^{1-(\alpha/Q)} \left[ \frac{1}{x_2^2} + \frac{1}{x_2} + \frac{1}{1-x_2} \right] dx_2 + \frac{\alpha^2}{4PQ} \left( 1 - 2 \log \frac{\alpha}{Q} \right) \int_{x_2}^{1-(\alpha/Q)} \frac{dx_2}{1-x_2}$ 
 $- \frac{\alpha^2}{2PQ} \int_{x_2}^{1-(\alpha/Q)} \left[ \frac{1}{x_2} + \frac{1}{1-x_2} \right] dx_2 - \frac{\alpha^2}{2PQ} \int_{x_2}^{1-(\alpha/Q)} \left[ \frac{1}{x_2^2} + \frac{1}{x_2} \right] \log(1-x_2) dx_2$ 

[41]  $= \frac{\alpha(\alpha - N)}{PQ} \left[ \frac{1}{2} \log \frac{\beta}{Q} + \frac{3}{4} \right] \times$

$$\begin{aligned}
& \times \left[ \left( \frac{1}{x_3} - \frac{1}{1 - (\alpha/Q)} \right) + \log \left( 1 - \frac{\alpha}{Q} \right) - \log x_3 + \log (1 - x_3) - \log \frac{\alpha}{Q} \right] \\
& + \frac{\alpha^2}{4PQ} \left( 1 - 2 \log \frac{\alpha}{Q} \right) \left[ \log (1 - x_3) - \log \frac{\alpha}{Q} \right] \\
& + \frac{\alpha^2}{2PQ} \left[ \frac{\log (\alpha/Q)}{1 - (\alpha/Q)} - \frac{\log (1 - x_3)}{x_3} \right] + \frac{c_1^2}{2PQ} \sum_1^{\infty} \frac{[1 - (\alpha/Q)]^n - x_3^n}{n^2}
\end{aligned}$$

where, since

$$[42] \quad \Phi(x) = \log x \log (1 - x) + \sum_1^{\infty} \frac{x^n}{n^2} + \sum_1^{\infty} \frac{(1 - x)^n}{n^2} = \text{const.} = \Phi(1) = \frac{\pi^2}{6},$$

one has

$$\begin{aligned}
[43] \quad \sum_1^{\infty} \frac{[1 - (\alpha/Q)]^n - x_3^n}{n^2} &= \log x_3 \log (1 - x_3) - \log \frac{\alpha}{Q} \log \left( 1 - \frac{\alpha}{Q} \right) \\
&+ \sum_1^{\infty} \frac{(1 - x_3)^n - (\alpha/Q)^n}{n^2}.
\end{aligned}$$

(f) For  $0 < x_3 < 1 - (\beta/Q)$

$$\begin{aligned}
I_3(x_3) &= I_3'''(x_3) = \int_{x_3}^1 x_2^{-1} \left[ (1 - P) - \frac{PQx_2}{dU/dx_2} \right]^{-1} I_2 dx_2 \\
[44] &= \int_{x_3}^{1-(\beta/Q)} \frac{[\frac{1}{4}(2\gamma - N) - \frac{1}{2}N \log(\beta/Q)]x_2^2 - \frac{1}{2}Nx_2 - \frac{1}{2}N(1 - x_2^2) \log(1 - x_2)}{x_2[(1 - P) + (PQ/N)x_2(1 - x_2)]} dx_2 \\
&+ \int_{1-(\beta/Q)}^{1-(\alpha/Q)} \frac{E(Q) + \alpha[\frac{1}{4}[1 - 2 \log(\alpha/Q)]x_2^2 - \frac{1}{2}x_2 - \frac{1}{2}(1 - x_2^2) \log(1 - x_2)]}{x_2[(1 - P) + (PQ/\alpha)x_2(1 - x_2)]} dx_2 \\
&+ \int_{1-(\alpha/Q)}^1 \frac{\frac{1}{6}Q(3x_2^2 - 2x_2^3) + F(Q)}{Px_2^2[1 + (1 - P)/Px_2]} dx_2
\end{aligned}$$

by [33], [34], and [36] and since  $dU/dx_2 = -Qx_2$  in the interval  $1 - (\alpha/Q) < x_3 < 1$ ,  $dU/dx_2 = -L/(1 - x_2) = -\alpha/(1 - x_2)$  in the interval  $1 - (\beta/Q) < x_3 < 1 - (\alpha/Q)$ , and  $dU/dx_2 = -N/(1 - x_2)$  in the interval  $0 < x_3 < 1 - (\beta/Q)$ .

Putting  $x_3 = 1 - (\beta/Q)$  in [41] and reducing to  $O(1/Q)$ , and adding the integral [40], the last two integrals of [44] have the value

$$[45] \quad H(PQ) = \left( \alpha - \frac{\alpha - \gamma}{P} \right) \left( \frac{2\gamma - 3N}{4} - \frac{N}{2} \log \frac{\beta}{Q} \right) \frac{1}{Q} + O\left(\frac{1}{Q^2}\right)$$

where

$$\gamma = \alpha(1 - \log(\alpha/\beta)).$$

If the exact analysis is carried out, one obtains the small additional term  $[\frac{1}{4}(2\gamma - 3N) - \frac{1}{2}N \log(\beta/Q)](\alpha/PQ) \log[P + (\alpha/\beta)(1 - P)]$ , see Appendix, giving the true value to  $O(1/Q)$  as

$$[46] \quad H(PQ) = \left[ \left( \alpha - \frac{\alpha - \gamma}{P} \right) + \frac{\alpha}{P} \log \left[ P + \frac{\alpha}{\beta}(1 - P) \right] \right] \left( \frac{2\gamma - 3N}{4} - \frac{N}{2} \log \frac{\beta}{Q} \right) \frac{1}{Q} + O\left(\frac{1}{Q^2}\right).$$

We thus have, approximating as before,

$$\begin{aligned}
 I_3'''(x_3) &= H(PQ) \\
 &+ \frac{N}{PQ} \int_{x_3}^{1-(\beta/Q)} \frac{[\frac{1}{4}(2\gamma-N) - \frac{1}{2}N\log(\beta/Q)] - \frac{1}{2}Nx_2 - \frac{1}{2}N(1-x_2^2)\log(1-x_2)}{x_2^2(1-x_2)} dx_2 \\
 &= H(PQ) + \frac{N}{2PQ} \left( \frac{2\gamma-N}{2} - \frac{N}{2} \log \frac{\beta}{Q} \right) \int_{x_3}^{1-(\beta/Q)} \frac{dx_2}{1-x_2} \\
 &- \frac{N^2}{2PQ} \int_{x_3}^{1-(\beta/Q)} \left[ \frac{1}{x_2} + \frac{1}{1-x_2} \right] dx_2 - \frac{N^2}{2PQ} \int_{x_3}^{1-(\beta/Q)} \left[ \frac{1}{x_2^2} + \frac{1}{x_2} \right] \log(1-x_2) dx_2 \\
 [47] \quad &= H(PQ) + \frac{N}{2PQ} \left( \frac{2\gamma-N}{2} - \frac{N}{2} \log \frac{\beta}{Q} \right) \left[ \log(1-x_3) - \log \frac{\beta}{Q} \right] \\
 &- \frac{N^2}{2PQ} \left[ \frac{\log(1-x_3)}{x_3} - \frac{\log(\beta/Q)}{1-(\beta/Q)} \right] + \frac{N^2}{2PQ} \sum_1^{\infty} \frac{[1-(\beta/Q)]^n - x_3^n}{n^2}
 \end{aligned}$$

which, using the approximate value [45] for  $H(PQ)$  and reducing, gives

$$\begin{aligned}
 I_3(x_3) &= \frac{N^2}{2PQ} \left[ \log \frac{\beta}{Q} \right]^2 + \left[ -\frac{\alpha N}{2Q} + \frac{(2\alpha - 4\gamma + 3N)N}{4PQ} \right] \log \frac{\beta}{Q} + \frac{\alpha(2\gamma - 3N)}{4Q} \\
 &- \left[ \frac{(\alpha - \gamma)(2\gamma - 3N)}{4} - \frac{N^2 \pi^2}{12} \right] \frac{1}{PQ} + \frac{N}{2PQ} \left[ \frac{2\gamma - N}{2} - N \log \frac{\beta}{Q} \right] \log(1-x_3) \\
 [48] \quad &- \frac{N^2}{2PQ} \frac{\log(1-x_3)}{x_3} - \frac{N^2}{2PQ} \sum_1^{\infty} \frac{x^n}{n^2}.
 \end{aligned}$$

If the unapproximated form of  $H(PQ)$  is used, and the denominator of the first integral of [44] is factorized according to

$$x_2 \left[ (1-P) + \frac{PQ}{N} x_2(1-x_2) \right] = \frac{PQ}{N} (\xi - x_2)(\eta + x_2)$$

and the integral evaluated by resolving into partial fractions, then, as in the appendix, the right-hand side of [48] will contain the additional small term

$$\left( \frac{2\gamma - 3N}{4} - \frac{N}{2} \log \frac{\beta}{Q} \right) \left[ \alpha \log \left[ P + \frac{\alpha}{\beta}(1-P) \right] - N \log \left[ 1 + \frac{N(1-P)}{\beta P} \right] \right] \frac{1}{PQ}.$$

The substitution of equation [48] in

$$[25] \quad \frac{t_w - t_3}{t_w - t_m} = \text{Nu} \sqrt{\frac{f}{2}} I_3$$

now gives the requisite temperature distribution in the turbulent core once  $\text{Nu}$  is determined.

Proceeding now to the Nusselt modulus one has

$$\begin{aligned}
 \frac{1}{\text{Nuf}} &= I = \int_0^{1-(\beta/Q)} [M + N \log Q + N \log(1-x_3)] x_3 I_3'''(x_3) dx_3 \\
 [49] \quad &+ \int_{1-(\beta/Q)}^{1-(\alpha/Q)} [K + L \log Q + L \log(1-x_3)] x_3 I_3''(x_3) dx_3 \\
 &+ Q \int_{1-(\alpha/Q)}^1 (1-x_3) x_3 I_3'(x_3) dx_3
 \end{aligned}$$

where  $I_3'''(x_3)$  is the value of  $I_3(x_3)$  in the interval  $0 \leq x_3 \leq 1 - (\beta/Q)$ ,  
 $I_3''(x_3)$  its value in the interval  $1 - (\beta/Q) \leq x_3 \leq 1 - (\alpha/Q)$ ,  
and  $I_3'(x_3)$  its value in the interval  $1 - (\alpha/Q) \leq x_3 < 1$ .

By equation [47]

$$\begin{aligned}
[50] \quad & \int_0^{1-(\beta/Q)} [M + N \log Q + N \log(1 - x_3)] x_3 I_3'''(x_3) dx_3 \\
& = H(PQ) \int_0^{1-(\beta/Q)} [M + N \log Q + N \log(1 - x_3)] x_3 dx_3 \\
& + \frac{N}{2PQ} \left( \frac{2\gamma - N}{2} - \frac{N}{2} \log \frac{\beta}{Q} \right) \\
& \times \int_0^{1-(\beta/Q)} [M + N \log Q + N \log(1 - x_3)] x_3 \left[ \log(1 - x_3) - \log \frac{\beta}{Q} \right] dx_3 \\
& + \frac{N^2}{2PQ} \int_0^{1-(\beta/Q)} [M + N \log Q + N \log(1 - x_3)] x_3 \\
& \quad \times \left[ \frac{\log(\beta/Q)}{1 - (\beta/Q)} - \frac{\log(1 - x_3)}{x_3} \right] dx_3 \\
& + \frac{N^2}{2PQ} \int_0^{1-(\beta/Q)} [M + N \log Q + N \log(1 - x_3)] x_3 \\
& \times \left[ \log x_3 \log(1 - x_3) - \log \frac{\beta}{Q} \log \left( 1 - \frac{\beta}{Q} \right) + \sum_1^\infty \frac{(1 - x_3)^n - (\beta/Q)^n}{n^2} \right] dx_3,
\end{aligned}$$

the last term following from the identity [43].

Substituting for  $H(PQ)$  from [45], integrating, and simplifying, one obtains

$$\begin{aligned}
[51] \quad & \int_0^{1-(\beta/Q)} [M + N \log Q + N \log(1 - x_3)] x_3 I_3'''(x_3) dx_3 \\
& = -\frac{N^3}{4PQ} \left( \log \frac{\beta}{Q} \right)^3 + \frac{1}{4} \left[ \frac{\alpha N^2}{Q} + \frac{N^2(4\gamma - 9N) - 2N^2(\alpha - \gamma)}{2PQ} \right] \left( \log \frac{\beta}{Q} \right)^2 \\
& + \left[ \frac{-\alpha N(2\gamma - 3N)}{4Q} + \frac{N[(\alpha - \gamma)(2\gamma - 3N) - (\gamma^2 - 6\gamma N + \frac{37}{4}N^2)]}{4PQ} \right] \log \frac{\beta}{Q} \\
& \quad + \left( \frac{2\gamma - 3N}{4} \right)^2 \frac{\alpha}{Q} \\
& + \left[ \frac{7N^2\gamma}{4} - \frac{71N^3}{32} + \frac{N^3}{2} \sum_1^\infty \frac{1}{n^3} - \frac{3\gamma^2 N}{8} - (\alpha - \gamma) \left( \frac{2\gamma - 3N}{4} \right)^2 \right] \frac{1}{PQ} + O \left( \frac{1}{Q^2} \right).
\end{aligned}$$

If the more exact expression for  $I_3''(x_3)$  is used, then a term

$$\begin{aligned}
[52] \quad & \left( \frac{2\gamma - 3N}{4} - \frac{N}{2} \log \frac{\beta}{Q} \right) \left[ \alpha \log \left( P + \frac{\alpha}{\beta} (1 - P) \right) - N \log \left( 1 + \frac{N(1 - P)}{\beta P} \right) \right] \\
& \quad \times \frac{1}{PQ} \int_0^{1-(\beta/Q)} [M + N \log Q + N \log(1 - x_3)] x_3 dx_3 \\
& = \left( \frac{2\gamma - 3N}{4} - \frac{N}{2} \log \frac{\beta}{Q} \right)^2 \\
& \quad \times \left[ \alpha \log \left( P + \frac{\alpha}{\beta} (1 - P) \right) - N \log \left( 1 + \frac{N(1 - P)}{\beta P} \right) \right] \frac{1}{PQ}
\end{aligned}$$

must be added.

Using equations [40] and [41] for  $I_3''(x_3)$ , and equations [38] for  $I_3'(x_3)$ , it is found that neither of the last two integrals of [49] yields terms to  $O(1/Q)$ ; that is, to this order, in the third integration, the laminar and buffer layers contribute nothing to the value of the Nusselt modulus.

It follows finally that

[53]

$$\begin{aligned} \frac{1}{Nuf} = & - \frac{N^3}{4PQ} \left( \log \frac{\beta}{Q} \right)^3 + \frac{1}{4} \left[ \frac{\alpha N^2}{Q} + \frac{N^2(4\gamma - 9N) - 2N^2(\alpha - \gamma)}{2PQ} \right] \left( \log \frac{\beta}{Q} \right)^2 \\ & + \left[ \frac{-\alpha N(2\gamma - 3N)}{4Q} + \frac{N[(\alpha - \gamma)(2\gamma - 3N) - (\gamma^2 - 6\gamma N + \frac{37}{4}N^2)]}{4PQ} \right] \log \frac{\beta}{Q} \\ & + \left( \frac{2\gamma - 3N}{4} \right)^2 \frac{\alpha}{Q} \\ & + \left[ \frac{7N^2\gamma}{4} - \frac{71N^3}{32} + \frac{N^3}{2} \sum_1^{\infty} \frac{1}{n^3} - \frac{3\gamma^2 N}{8} - (\alpha - \gamma) \left( \frac{2\gamma - 3N}{4} \right)^2 \right] \frac{1}{PQ} \\ & + \epsilon + O\left(\frac{1}{Q^2}\right), \end{aligned}$$

where

$$\epsilon = \left[ \frac{N}{2} \log \frac{\beta}{Q} - \frac{2\gamma - 3N}{4} \right]^2 \left[ \alpha \log \left[ P + \frac{\alpha}{\beta} (1-P) \right] - N \log \left[ 1 + \frac{N(1-P)}{\beta P} \right] \right] \frac{1}{PQ}$$

and is small.

##### 5. ATTEMPT TO OBTAIN SIMILAR RESULTS ON THE BASIS OF THE VORTICITY TRANSFER ANALOGY

Before analyzing the above results obtained on the basis of the momentum transfer analogy, an attempt will be made to obtain corresponding results on the "vorticity transfer" theory.

The vorticity transfer theory was propounded by G. I. Taylor (11, 12) who pointed out that a statistical theory of turbulence with momentum conserved as the transferable property, as originally proposed by Prandtl, required that the fluctuating turbulent pressures do not influence the mean transport of momentum, and who further proved that this condition only holds when momentum in a given direction  $z$  say is transferred in a plane  $xy$  by turbulent motion in which lines of particles once parallel to the motion remain so throughout the motion. He suggested, having shown that the momentum transfer theory cannot hold for purely two-dimensional motion, that if the whole motion is confined to a plane,  $xy$  say, then by Kelvin's circulation theorem, vorticity in the direction  $z$  is conserved and is the transferable property. The theory was subsequently generalized to three dimensions, and a modified vorticity transfer theory set up, one of the main assumptions of which is that components of vorticity are transferable in the sense that heat is transferable (3).

The modified vorticity transfer theory yields a turbulent velocity distribution for pipe flow in as good agreement with experiment as that derived from the momentum transfer theory. The theory seems to hold for wakes

(where the turbulence might well be approximately two-dimensional as in the case of a von Karman vortex street) but it appears to break down in the neighborhood of solid boundaries.

The equation representing fluid flow through the pipe is now written

$$[54] \quad \frac{1}{\rho} \frac{\partial \bar{P}}{\partial z} = (\epsilon_V + \nu) \left[ \frac{1}{r} \frac{\partial}{\partial r} \left( r \frac{\partial u}{\partial r} \right) \right]$$

so that in analogy with equation [17] one now has

$$[55] \quad \frac{\epsilon_V}{\nu} = - \left\{ 2Qx + \frac{d}{dx} \left[ x \frac{dU}{dx} \right] \right\} \Big/ \frac{d}{dx} \left[ x \frac{dU}{dx} \right].$$

Also

$$[56] \quad \frac{a}{\epsilon_H + a} = \frac{1}{P'(\epsilon_V/\nu) + 1}$$

$$[57] \quad = \left[ (1 - P') - \frac{2P'Qx}{d[x \frac{dU}{dx}] / dx} \right]^{-1}$$

so that one now has

$$[58] \quad \frac{t_w - t_3}{t_w - t_m} = \text{Nu} \sqrt{\frac{f}{2}} J_3,$$

$$[59] \quad 1/\text{Nu}f = J,$$

where

$$[60] \quad J_3 = \int_{x_2}^1 x_2^{-1} \left[ (1 - P') - \frac{2P'Qx_2}{d[x_2 \frac{dU}{dx_2}] / dx_2} \right]^{-1} \int_0^{x_2} U_1 x_1 dx_1 dx_2$$

and

$$[61] \quad J = \int_0^1 U_3 x_3 J_3 dx_3.$$

Owing to the complicated nature of the second integration only the case  $P' = 1$  will be considered. Also the buffer layer will be omitted.

The integrals  $J_3$  and  $J$  have thus to be evaluated for

$$[62] \quad \begin{cases} U = U'(x) = Q(1 - x) \text{ for } 1 > x > 1 - (\delta/Q), \\ U = U''(x) = M + N \log Q(1 - x) \text{ for } 1 - (\delta/Q) > x > 0 \end{cases}$$

where from continuity of velocity at  $y = Q(1 - x) = \delta$ ,

$$[63] \quad \delta = M + N \log \delta.$$

Writing  $J_2(x_2) = \int_0^{x_2} U x_1 dx_1$ , one has:

(a) For  $0 < x_2 < 1 - (\delta/Q)$

$$[64] \quad \begin{aligned} J_2(x_2) &= J_2''(x_2) = \int_0^{x_2} [M + N \log Q + N \log (1 - x_1)] x_1 dx_1 \\ &= \left( \frac{2\delta - N}{Q} - \frac{N}{2} \log \frac{\delta}{Q} \right) x_2^2 - \frac{N}{2} x_2 - \frac{N}{2} (1 - x_2^2) \log (1 - x_2). \end{aligned}$$

(b) For  $1 - (\delta/Q) < x_2 < 1$

$$J_2(x_2) = J_2'(x_2) = \int_0^{1-(\delta/Q)} [M + N \log Q + N \log (1 - x_1)] x_1 dx_1$$

$$+ Q \int_{1-(\delta/Q)}^{x_2} (x_1 - x_1^2) dx_1$$

[65]

$$= \frac{1}{6} Q (3x_2^2 - 2x_2^3) + F(Q)$$

where

$$[66] \quad F(Q) = -\frac{N}{2} \log \frac{\delta}{Q} - \frac{Q}{6} + \frac{2\delta - 3N}{4} + \frac{\delta^2 - 2(\delta - N)\delta}{2Q} + O\left(\frac{1}{Q^2}\right).$$

$$[67] \quad \text{For } P' = 1; J_3(x_3) = -\frac{1}{2Q} \int_{x_3}^1 x_2^{-2} \left( \frac{dU}{dx_2} + x_2 \frac{d^2U}{dx_2^2} \right) J_2(x_2) dx_2$$

so that:

$$(c) \quad \text{For } 1 - \frac{\delta}{Q} < x_3 < 1 \text{ where } \frac{dU}{dx_2} + x_2 \frac{d^2U}{dx_2^2} = -Q$$

$$J_3(x_3) = J_3'(x_3) = \int_{x_3}^1 \frac{J_2' dx_2}{2x_2^2}$$

$$= \frac{Q}{12} \int_{x_3}^1 (3 - 2x_2) dx_2 + \frac{1}{2} \int_{x_3}^1 \frac{F(Q)}{x_2^2} dx_2 \text{ by [65]}$$

[68]

$$= \frac{Q}{12} (x_3^2 - 3x_3) + \frac{1}{2} \left( \frac{Q}{3} - F(Q) \right) + \frac{F(Q)}{2x_3}$$

and

$$(d) \quad \text{for } 0 < x_2 < 1 - \frac{\delta}{Q} \text{ where } \frac{dU}{dx_2} + x_2 \frac{d^2U}{dx_2^2} = -\frac{N}{(1 - x_2)^2}$$

$$[69] \quad J_3(x_3) = J_3''(x_3) = \frac{N}{2Q} \int_{x_3}^{1-(\delta/Q)} \frac{J_2''(x_2) dx_2}{x_2(1 - x_2)^2} + \int_{1-(\delta/Q)}^1 \frac{J_2'(x_2)}{2x_2^2} dx_2$$

$$= \frac{N}{2Q} \left( \frac{2\delta - N}{4} - \frac{N}{2} \log \frac{\delta}{Q} \right) \int_{x_3}^{1-(\delta/Q)} \frac{dx_2}{(1 - x_2)^2} - \frac{N^2}{4Q} \int_{x_3}^{1-(\delta/Q)} \frac{dx_2}{x_2(1 - x_2)^2}$$

$$- \frac{N^2}{4Q} \int_{x_3}^{1-(\delta/Q)} \frac{(1 + x_2) \log (1 - x_2) dx_2}{x_2^2(1 - x_2)} + \frac{1}{2} \left( \frac{2\delta - 3N}{4} - \frac{N}{2} \log \frac{\delta}{Q} \right) \frac{\delta}{Q} + O\left(\frac{1}{Q^2}\right)$$

by [64] and by putting  $x_3 = 1 - (\delta/Q)$  in [68]

$$[70] \quad = \frac{1}{2} \left( \frac{2\delta - 3N}{4} - \frac{N}{2} \log \frac{\delta}{Q} \right) \left( \frac{\delta}{Q} + \frac{N}{\delta} \right) + \frac{N^2}{4Q} \left[ \left( \log \frac{\delta}{Q} \right)^2 + \left( \log \frac{\delta}{Q} \right) \right]$$

$$- \frac{N}{2Q} \left( \frac{2\delta - 3N}{4} - \frac{N}{2} \log \frac{\delta}{Q} \right) \frac{1}{1 - x_3}$$

$$- \frac{N^2}{4Q} \left[ \frac{\log (1 - x_3)}{x_3} + [\log (1 - x_3)]^2 + 2 \sum_1^{\infty} \frac{x_3^n}{n^2} - \frac{\pi^2}{3} \right] + O\left(\frac{1}{Q^2}\right).$$

Equation [70] substituted in equation [58] gives the temperature distribution throughout the turbulent core once  $\text{Nu}$  is determined.

The Nusselt modulus is now given by

$$\begin{aligned}
 \frac{1}{\text{Nuf}} = J &= \int_0^{1-(\delta/Q)} U_3'' x_3 J_3'' dx_3 + \int_{1-(\delta/Q)}^1 U_3' x_3 J_3' dx_3 \\
 &= \int_0^{1-(\delta/Q)} U_3'' x_3 J_3'' dx_3 + O\left(\frac{1}{Q^2}\right) \\
 &= \left[ \frac{1}{2} \left( \frac{2\delta - 3N}{4} - \frac{N}{2} \log \frac{\delta}{Q} \right) \left( \frac{\delta}{Q} + \frac{N}{\delta} \right) + \left[ \left( \log \frac{\delta}{Q} \right)^2 + \left( \log \frac{\delta}{Q} \right) \right] \frac{N^2}{4Q} \right] \\
 &\quad \times \int_0^{1-(\delta/Q)} [M + N \log Q + N \log (1 - x_3)] x_3 dx_3 \\
 &- \frac{N}{2Q} \left( \frac{2\delta - 3N}{4} - \frac{N}{2} \log \frac{\delta}{Q} \right) \int_0^{1-(\delta/Q)} [M + N \log Q + N \log (1 - x_3)] \frac{x_3}{1 - x_3} dx_3 \\
 &- \frac{N^2}{4Q} \int_0^{1-(\delta/Q)} [M + N \log Q + N \log (1 - x_3)] \log (1 - x_3) dx_3 \\
 [71] \quad &= \frac{1}{2} \left( \frac{2\delta - 3N}{4} - \frac{N}{2} \log \frac{\delta}{Q} \right)^2 \left( \frac{\delta}{Q} + \frac{N}{\delta} \right) \\
 &\quad + \left( \frac{2\delta - 3N}{4} - \frac{N}{2} \log \frac{\delta}{Q} \right) \frac{N(2\delta - N)}{4Q} \log \frac{\delta}{Q} + \left( \frac{1}{4} - \sum_1^{\infty} \frac{1}{n^3} \right) \frac{N^3}{2Q}.
 \end{aligned}$$

In equations [70] and [71] the results are vitiated by the respective terms  $[\frac{1}{4}(2\delta - 3N) - \frac{1}{2}N \log(\delta/Q)]N/\delta$  and  $[\frac{1}{4}(2\delta - 3N) - \frac{1}{2}N \log(\delta/Q)]^2N/\delta$  which are not  $O(1/Q)$ . For any sort of a result at all these must vanish.  $N$  being fixed at about 2.5 from the experimentally well defined velocity distribution for fully developed turbulence, the only possibility is to alter  $\delta$ . This could reasonably be done since the velocity distribution adjacent to the wall is uncertain.

Of the two possibilities however, it is seen

(a) that  $\frac{1}{4}(2\delta - 3N) - \frac{1}{2}N \log(\delta/Q) = 0$ , giving the impossible result  $\text{Nuf} = Q/11.34$ , requires that  $\log_{10}(Q/\delta) = 0.6514 - 0.1737\delta$ , which is equally impossible,

(b) that  $(\delta/Q) + (N/\delta) = 0$  requires  $\delta$  to be imaginary, which is also impossible.

It thus seems that vorticity transfer will not give a reasonable answer to this problem, at least until definite modifications are made.

#### 6. FORMULAE OBTAINED ON MOMENTUM TRANSFER ANALOGY: NUMERICAL RESULTS

Inserting the numerical values  $\alpha = 5$ ,  $\beta = 30$ ,  $\gamma = 14$ ,  $N = 2.5$ , equation [53] for the Nusselt modulus with all three layers becomes

$$\begin{aligned}
 \frac{1}{\text{Nuf}} &= -\frac{47.69}{PQ} \left( \log_{10} \frac{30}{Q} \right)^3 + \left( \frac{41.42}{Q} + \frac{212.3}{PQ} \right) \left( \log_{10} \frac{30}{Q} \right)^2 \\
 [53a] \quad &- \left( \frac{146.9}{Q} + \frac{325.5}{PQ} \right) \log_{10} \frac{30}{Q} + \frac{130.3}{Q} + \frac{178.1}{PQ} + \epsilon_1
 \end{aligned}$$

TABLE I

P	a <sub>1</sub>	a <sub>2</sub>	a <sub>3</sub>	a <sub>4</sub>	a <sub>5</sub>	a <sub>6</sub>	a <sub>7</sub>
0.55	04.67152	-101.53660	30.12436	66.50672	-30.12436	-13.08284	-5.681818
0.65	89.38037	-91.14486	25.48984	56.27492	-25.48984	-11.07009	-4.80769
0.75	85.05109	-84.43781	22.09120	48.77146	-22.09120	-9.59408	-4.16667
0.85	81.14096	-76.01162	19.49223	43.03376	-19.49223	-8.46536	-3.67647
1.00	76.39111	-69.55950	16.56836	36.57865	-16.56836	-7.19556	-3.12500
1.50	65.59984	-54.64644	11.04560	24.38580	-11.04560	-4.79704	-2.08333
2.00	58.96282	-46.48987	8.28420	18.28933	-8.28420	-3.59778	-1.56250
4.00	46.43836	-32.80651	4.14209	9.14466	-4.14209	-1.79889	-0.78125
6.00	41.13861	-27.61109	2.76140	6.09644	-2.76140	-1.19926	-0.52083
8.00	38.13233	-24.81241	2.07105	4.57234	-2.07105	-0.89945	-0.39063
10.00	36.17014	-23.04387	1.65684	3.65787	-1.65684	-0.71956	-0.31250
14.00	33.73328	-20.91309	1.18346	2.61276	-1.18346	-0.51397	-0.22321

TABLE II

VALUES OF Q, RE, AND f, AS TAKEN FROM VON KARMAN'S LAW:  
 $1/f = (4.0 \log_{10} Q + 1.4062)^2$

Q (= Re $\sqrt{(f/8)}$ )	Re	1/f	f
300	9,600.73	127.939	0.007816
1,150	44,997.8	186.295	0.005368
3,000	129,948	234.540	0.004264
4,000	178,918	250.095	0.003998
5,000	229,130	262.507	0.003809
6,000	280,331	272.858	0.003665
7,000	332,355	281.790	0.003549
8,000	385,082	289.633	0.003453
9,000	438,426	296.637	0.003371
10,000	492,317	302.976	0.003301
20,000	1,052,749	346.343	0.002887

TABLE III  
NUSSELT MODULUS

Q	Re	kPr									
		0.55	0.65	0.75	0.85	1.00	1.05	1.10	1.50	2.00	
300	9,600.73	27.1115	29.2176	31.1608	32.9671	35.4647	36.2482	37.0078	42.4263	47.9544	
1,150	44,997.8	81.9849	90.1662	97.3867	104.279	113.833	116.838	119.755	140.667	162.203	
3,000	129,948	185.375	205.378	223.958	241.341	261.553	273.192	280.623	334.183	389.875	
4,000	178,918	237.606	263.868	288.301	311.195	343.125	359.125	375.125	431.278	443.532	531.563
5,000	229,130	288.343	320.768	356.199	379.297	418.824	431.278	443.532	531.563	623.585	
6,000	280,331	331.928	376.430	412.331	446.034	493.057	506.298	583.601	600.455	726.194	850.368
7,000	332,355	386.924	431.418	472.890	511.225	566.298	583.601	600.455	726.194	850.368	
8,000	385,082	434.569	485.052	532.197	576.517	638.542					
9,000	438,426	481.866	538.265	590.970	640.545	709.998					
10,000	492,317	528.013	590.882	649.104	703.901	780.667	805.012	828.729	1000.97	1182.31	
20,000	1,052,749	975.523	1084.95	1206.99	1312.77	1461.46	1508.71	1554.82	1891.00	2247.40	

Q	Re	kPr									
		4.00	6.00	8.00	10.00	12.00	14.00	50	100	500	
300	9,600.73	62.7278	71.7416	77.9940	82.6479	86.2756	89.1965	107.2234	112.7315	118.4401	
1,150	44,997.8	220.740	257.125	282.629	301.740	316.703	328.793				
3,000	129,948	543.662	640.785	709.478	761.254	801.961	834.947	1041.5667	1105.2780	1170.5929	
4,000	178,918										
5,000	229,130	879.892	1043.19	1159.28	1247.07	1316.25	1372.41	1725.8842	1834.5586	1946.9480	
6,000	280,331										
7,000	332,355	1208.82	1438.49	1602.33	1726.49	1824.49	1904.15	2406.8158	2561.9601	2722.0826	
8,000	385,082										
9,000	438,426										
10,000	492,317	1693.29	2022.81	2258.67	2437.85	2579.51	2694.80	3425.005	3650.797	3883.859	
20,000	1,052,749	3262.14	3925.99	4403.79	4768.46	5057.71	5293.72				

TABLE IV  
VALUES OF  $\Delta Nu$  = NUSSELT MODULUS CALCULATED WITHOUT BUFFER LAYER MINUS  
NUSSELT MODULUS CALCULATED WITH ALL THREE LAYERS

Q	Re	kPr							
		0.55	0.65	0.75	0.85	1.00	1.05	1.10	1.50
300	9,600.73	2.3257	2.0345	1.6468	1.1865	0.3964	0.1154	-0.1712	-2.6040
1,150	44,997.8	5.5120	4.8440	4.193	3.097	1.055	0.296	-0.514	-7.630
3,000	129,948	10.803	10.037	8.522	6.387	2.216	0.627	-1.043	-16.675
4,000	178,918	13.308	12.410	10.600	7.970	2.777			
5,000	229,130	15.674	14.690	12.565	9.473	3.307	1.011	-1.576	-25.446
6,000	280,331	17.937	16.860	14.456	10.921	3.904			
7,000	332,355	20.142	18.979	16.309	12.346	4.366	1.238	-2.069	-37.428
8,000	385,082	22.247	20.999	18.071	13.696	4.822			
9,000	438,426	24.304	22.976	19.936	15.015	5.243			
10,000	492,317	26.321	24.923	21.505	16.328	5.753	1.605	-2.783	-45.406
20,000	1,052,749	44.807	42.78	37.19	28.42	10.08	2.81	-4.93	-81.46

Q	Re	kPr						
		2.00	4.00	6.00	8.00	10.00	12.00	14.00
300	9,600.73	-5.7166	-15.9189	-23.1329	-28.4183	-32.4630	-35.6852	-38.3065
1,150	44,997.8	-17.358	-52.920	-79.703	-99.931	-115.711	-128.376	-138.784
3,000	129,948	-38.961	-125.234	-193.112	-245.471	-286.825	-320.302	-347.976
4,000	178,918							
5,000	229,130	-60.194	-198.518	-309.762	-396.526	-465.504	-521.591	-568.11
6,000	280,331							
7,000	332,355	-80.246	-269.063	-423.00	-543.94	-640.48	-719.21	-784.66
8,000	385,082							
9,000	438,426							
10,000	492,317	-109.07	-371.61	-588.86	-760.72	-898.57	-1011.33	-1105.26
20,000	1,052,749	-198.46	-696.97	-1120.66	-1460.62	-1735.63	-1961.91	-2151.23

where  $\epsilon_1$  is small and given by

$$\epsilon_1 = \frac{[5.1 - 2.9 \log_{10} (30/Q)]^2}{PQ} \times \left\{ 11.5 \log_{10} [P + 0.17(1 - P)] - 5.8 \log_{10} \left[ 1 + 0.083 \left( \frac{1 - P}{P} \right) \right] \right\}.$$

Numerical values for  $\text{Nu}$  are given in Table III.

The corresponding equation for buffer layer omitted, obtained by substituting  $\alpha = \beta = 11.5$ ,  $\gamma = 0$ ,  $N = 2.5$  in equation [53], becomes

$$[53b] \quad \frac{1}{\text{Nuf}} = -\frac{47.69}{PQ} \left( \log_{10} \frac{11.5}{Q} \right)^3 + \left( \frac{95.27}{Q} + \frac{97.34}{PQ} \right) \left( \log_{10} \frac{11.5}{Q} \right) - \left( \frac{256.5}{Q} + \frac{25.27}{PQ} \right) \log_{10} \frac{11.5}{Q} + \frac{172.7}{Q} - \frac{23.48}{PQ} + \epsilon_2$$

where  $\epsilon_2$  is small and given by

$$\epsilon_2 = -\frac{[7.75 - 5.8 \log_{10} (11.5/Q)]^2}{PQ} 1.4 \log_{10} \left[ 1 + 0.22 \left( \frac{1 - P}{P} \right) \right].$$

Equations [53a] and [53b] enable  $\Delta \text{Nu}$ , the effect of the buffer layer and in fact the order of the error caused through uncertainty in the adjacent-to-wall velocity distribution, to be investigated. In particular it is found that  $\Delta \text{Nu} = 0$  for  $P = 1.07$ . See Table IV.

When  $P$  and  $Q$  are large such that  $P/Q^2$  tends to zero, equations [53a] and [53b] take the respective forms

$$[53c] \quad \frac{1}{\text{Nu}_f} = \frac{41.42}{Q} \left( \log_{10} \frac{30}{Q} \right)^2 - \frac{146.9}{Q} \log_{10} \frac{30}{Q} - \frac{130.3}{Q}$$

and

$$[53d] \quad \frac{1}{\text{Nu}_f} = \frac{95.27}{Q} \left( \log_{10} \frac{11.5}{Q} \right)^2 - \frac{256.5}{Q} \log_{10} \frac{11.5}{Q} + \frac{172.7}{Q}.$$

Putting  $Q = 2 \times 10^4$  corresponding to  $\text{Re} \approx 10^6$ , it is found that at this value the heat barrier introduced by omitting the buffer layer more than halves the Nusselt modulus.

For the temperature distribution equations [25] and [48] give

$$[72] \quad \frac{Q}{\text{Nu} \sqrt{f/2}} \frac{t_w - t_3}{t_w - t_m} = a_1 + a_2 \log_{10} \frac{30}{Q} + a_3 \left( \log_{10} \frac{30}{Q} \right)^2 + \left( a_4 + a_5 \log_{10} \frac{30}{Q} \right) \log_{10} (1 - x_3) + a_6 \frac{\log_{10} (1 - x_3)}{x_3} + a_7 \sum_1^{\infty} \frac{x^n}{n^2}$$

where  $a_1, \dots, a_7$  are functions of  $P$  whose values are given in Table I.

Writing

$$\Theta(x) = \sum_1^{\infty} \frac{x^n}{n^2} = - \int_0^x \frac{\log_e (1 - x)}{x} dx$$

it may be shown that

$$[73] \quad \left\{ \begin{array}{l} \Theta(1) = \frac{\pi^2}{6}, \\ \Theta\left(2 \sin \frac{\pi}{10}\right) = \frac{\pi^2}{10} - \left[ \log_e \left(2 \sin \frac{\pi}{10}\right) \right]^2, \\ \Theta\left[\left(2 \sin \frac{\pi}{10}\right)^2\right] = \frac{\pi^2}{15} - \left[ \log_e \left(2 \sin \frac{\pi}{10}\right) \right]^2, \\ \Theta\left(\frac{1}{2}\right) = \frac{\pi^2}{12} - \frac{1}{2} [\log_e \frac{1}{2}]^2, \\ \Theta(0) = 0. \end{array} \right.$$

Values of  $(t_w - t_3)/(t_w - t_m)$  are given in Table V.

Equations [25] and [48] prophesy a zero temperature gradient on the tube axis.

Thus in the region  $0 < x_3 < 1 - (\beta/Q)$

$$\begin{aligned} \frac{\partial}{\partial x_3} \left[ \frac{t_w - t_3}{t_w - t_m} \right] &= \text{Nu} \sqrt{\frac{f}{2}} \frac{\partial I_3}{\partial x_3} = - \text{Nu} \sqrt{\frac{f}{2}} \left[ \frac{I_2}{x_2[(1-P) + (PQ/N)(1-x_2)x_2]} \right] \\ &= - \text{Nu} \sqrt{\frac{f}{2}} \\ &\times \left[ \frac{\frac{1}{2}(2\gamma - N) - \frac{1}{2}N \log(\beta/Q)x_2 + \frac{1}{2}Nx_2 \log(1-x_2) - \frac{1}{2}N[1 + \log(1-x_2)/x_2]}{(1-P) + (PQ/N)x_2(1-x_2)} \right] \end{aligned}$$

TABLE V

VALUES OF  $\frac{t_w - t_0}{t_w - t_m}$

$t_w$  = wall temperature,  $t_m$  = mean temperature of fluid,  $t_0$  = local temperature at  $x_0 = r_0/r_0$ .  
( $P = kPr$ ).

$\frac{P}{Q}$	0.55	0.75	1.00	1.50	2.00	4.00	6.00	8.00	10.00
I. $x_0 = r/r_0 = 0$									
300	1.31072	1.27100	1.22409	1.17910	1.15211	1.10014	1.07681	1.06297	1.05367
1,150	1.24342	1.22101	1.18563						
5,000	1.19467	1.18215	1.15479	1.13039	1.12069	1.07953	1.06208	1.05112	1.04348
10,000	1.17739	1.16781	1.14321	1.12179	1.10734	1.07555	1.05923	1.04884	1.04154
20,000	1.16257	1.15527	1.13297	1.11396	1.10099	1.07180	1.05650	1.04667	1.03969
II. $x_0 = r/r_0 = [2 \sin (\pi/10)]^2 = 0.38197$									
300	1.19129	1.17033	1.13890	1.11057	1.09402	1.06215	1.04783	1.03935	1.03365
1,150	1.15178	1.14117	1.11564						
5,000	1.12210	1.11737	1.09681	1.08124	1.07112	1.04908	1.03801	1.03106	1.02622
10,000	1.11401	1.10839	1.08961	1.07597	1.06675	1.04648	1.03608	1.02946	1.02481
20,000	1.10210	1.10042	1.08316	1.07093	1.06268	1.04399	1.03419	1.02790	1.02343
III. $x_0 = r/r_0 = 0.50$									
300	1.14010	1.12719	1.10141	1.08120	1.06912	1.04586	1.03542	1.02923	1.02506
1,150	1.11234	1.10688	1.08553						
5,000	1.09076	1.08940	1.07178	1.00016	1.05248	1.03594	1.02762	1.02240	1.01877
10,000	1.08287	1.08270	1.06643	1.05617	1.04920	1.03391	1.02607	1.02108	1.01757
20,000	1.07594	1.07667	1.06160	1.05238	1.04611	1.03196	1.02454	1.01978	1.01640
IV. $x_0 = r/r_0 = 2 \sin (\pi/10) = 0.61804$									
300	1.07618	1.07331	1.05535	1.04452	1.03803	1.02552	1.01991	1.01658	1.01434
1,150	1.06296	1.06381	1.04781						
5,000	1.05145	1.05431	1.04037	1.03359	1.02910	1.01944	1.01458	1.01154	1.00942
10,000	1.04705	1.05044	1.03734	1.03130	1.02717	1.01814	1.01350	1.01056	1.00849
20,000	1.04306	1.04684	1.03451	1.02902	1.02528	1.01683	1.01241	1.00957	1.00756

which vanishes at  $x_2 = 0$  since  $\lim_{x_2 \rightarrow 0} \frac{\log (1 - x_2)}{x_2} = -1$ .

## APPENDIX

The integral

$$\int_{x_0}^{1-(\alpha/Q)} \frac{E(Q) + \alpha[\frac{1}{4}[1 - 2 \log (\alpha/Q)]x_2^2 - \frac{1}{2}x_2 - \frac{1}{2}(1 - x_2^2) \log (1 - x_2)]}{x_2[(1 - P) - (PQ/\alpha)x_2(1 - x_2)]} dx_2$$

of equation [39], required for the range  $1 - (\beta/Q) \leq x_0 \leq 1 - (\alpha/Q)$  is expressible in partial fractions as

$$\begin{aligned} \frac{\alpha E(Q)}{PQ} \frac{1}{\lambda \mu} \int_{x_0}^{1-(\alpha/Q)} \frac{dx_2}{x_2} + \frac{\alpha E(Q)}{PQ} \frac{1}{\lambda(\lambda + \mu)} \int_{x_0}^{1-(\alpha/Q)} \frac{dx_2}{\lambda - x_2} \\ - \frac{\alpha E(Q)}{PQ} \frac{1}{\mu(\lambda + \mu)} \int_{x_0}^{1-(\alpha/Q)} \frac{dx_2}{\mu + x_2} \\ + \frac{\alpha^2 [1 - 2 \log (\alpha/Q)]}{4PQ(\lambda + \mu)} \int_{x_0}^{1-(\alpha/Q)} \left[ \frac{\lambda}{\lambda - x_2} - \frac{\mu}{\mu + x_2} \right] dx_2 \\ - \frac{\alpha^2}{2PQ(\lambda + \mu)} \int_{x_0}^{1-(\alpha/Q)} \left[ \frac{1}{\lambda - x_2} + \frac{1}{\mu + x_2} \right] dx_2 \\ - \frac{\alpha^2}{2PQ} \int_{x_0}^{1-(\alpha/Q)} \left[ \frac{1}{\lambda \mu x_2} + \frac{1 - \lambda^2}{\lambda(\lambda + \mu)} \frac{1}{\lambda - x_2} + \frac{\mu^2 - 1}{\mu(\lambda + \mu)} \frac{1}{\mu + x_2} \right] \log(1 - x_2) dx_2 \end{aligned}$$

where

$$PQ(\lambda - x_2)(\mu + x_2) = \alpha(1 - P) + PQx_2 - PQx_2^2$$

so that

$$\lambda = 1 + \frac{\alpha(1 - P)}{PQ} + O\left(\frac{1}{Q^2}\right),$$

$$\mu = \frac{\alpha(1 - P)}{PQ} + O\left(\frac{1}{Q^2}\right),$$

$$\lambda = 1 + \mu,$$

$$\lambda\mu = \frac{\alpha(1 - P)}{PQ},$$

$$\frac{1}{\lambda} = 1 - \frac{\alpha(1 - P)}{PQ} + O\left(\frac{1}{Q^2}\right),$$

$$\frac{1}{\mu} = \frac{PQ}{\alpha(1 - P)} + 1 - \frac{\alpha(1 - P)}{PQ} + O\left(\frac{1}{Q^2}\right),$$

$$\frac{1}{\lambda + \mu} = 1 - \frac{2\alpha(1 - P)}{PQ} + O\left(\frac{1}{Q^2}\right),$$

$$\frac{1}{\lambda(\lambda + \mu)} = 1 + O\left(\frac{1}{Q}\right),$$

$$\frac{1}{\mu(\lambda + \mu)} = \frac{PQ}{\alpha(1 - P)} - 1 + O\left(\frac{1}{Q}\right),$$

$$\frac{1 - \lambda^2}{\lambda(\lambda + \mu)} = - \frac{2\alpha(1 - P)}{PQ} + O\left(\frac{1}{Q^2}\right),$$

$$\frac{\mu^2 - 1}{\mu(\lambda + \mu)} = 1 - \frac{PQ}{\alpha(1 - P)} + O\left(\frac{1}{Q}\right).$$

Evaluating the integral and using equation [40], one obtains the result

$$\begin{aligned}
 I_3''(x_3) = & \frac{\alpha}{Q} \left[ -\frac{N}{2} \log \frac{\beta}{Q} + \frac{2\gamma - 3N}{4} \right] \\
 & + \frac{(\alpha - N)}{(1 - P)} \left[ \frac{1}{2} \log \frac{\beta}{Q} + \frac{3}{4} - \frac{\beta}{Q} \right] \left[ \log \left( 1 - \frac{\alpha}{Q} \right) - \log x_3 \right] \\
 & + \frac{\alpha}{PQ} \left[ \frac{2\gamma - 3N}{4} - \frac{N}{2} \log \frac{\beta}{Q} \right] \\
 & \times \left[ \log (1 - x_3) + \log \left( 1 + \frac{\mu}{1 - x_3} \right) - \log \frac{\alpha}{Q} - \log \left( 1 + \frac{\mu Q}{\alpha} \right) \right] \\
 & + \frac{(\alpha - N)}{(1 - P)} \left[ \frac{1}{2} \log \frac{\beta}{Q} + \frac{3}{4} - \frac{\beta}{Q} \right] \left[ \log \left( 1 - \frac{1 - x_3}{\lambda} \right) - \log \left( 1 - \frac{\alpha}{\lambda Q} \right) \right] \\
 & - \frac{\alpha}{2PQ} \left[ \frac{\alpha - 3N}{2} + (\alpha - N) \log \frac{\beta}{Q} \right] \left[ \log \left( 1 - \frac{1 - x_3}{\lambda} \right) - \log \left( 1 - \frac{\alpha}{\lambda Q} \right) \right] \\
 & + \frac{\alpha}{2(1 - P)} \left[ \log (1 - x_3) \log x_3 - \log \left( 1 - \frac{\alpha}{Q} \right) \log \frac{\alpha}{Q} \right. \\
 & \quad \left. + \sum_1^{\infty} \frac{(1 - x_3)^n - (\alpha/Q)^n}{n^2} \right]
 \end{aligned}$$

$$+ \left[ \frac{\alpha^2}{2PQ} - \frac{\alpha}{2(1-P)} \right] \left[ \log \left( 1 - \frac{1-x_3}{\lambda} \right) \log (1-x_3) \right. \\ \left. - \log \left( 1 - \frac{\alpha}{\lambda Q} \right) \log \frac{\alpha}{Q} + \sum_1^{\infty} \frac{[(1-x_3)/\lambda]^n - (\alpha/\lambda Q)^n}{n^2} \right] + O\left(\frac{1}{Q^2}\right)$$

and provided  $P < Q/\beta < Q/\alpha$  all the logs are defined throughout the range. If  $P$  becomes higher than this value, an "incision" in the range of integration would leave the result to  $O(1/Q)$  unaltered.

The additional  $O(1/Q)$  term in  $H(PQ)$ , the value of  $I_3(x_3)$  for  $x_3 = 1 - (\beta/Q)$ , arises from the terms containing  $\log [1 + \mu/(1-x_3)]$  and  $\log [1 + (\mu Q/\alpha)]$  in the second line of the above expression. Thus while  $\log [1 - (\alpha/\lambda Q)]$  and  $\log [1 - (\beta/\lambda Q)]$  are both  $O(1/Q)$ ,  $\log [1 + (\mu Q/\alpha)] = -\log P + O(1/Q)$  and  $\log [1 + (\mu Q/\beta)] = \log [1 + \alpha(1-P)/\beta P] + O(1/Q)$ .

Again the integral

$$\int_{x_3}^{1-(\beta/Q)} \frac{[\frac{1}{4}(2\gamma - N) - \frac{1}{2}N \log (\beta/Q)] x_2^2 - \frac{1}{2}N x_2 - \frac{1}{2}N(1-x_2^2) \log (1-x_2)}{x_2[(1-P) + (PQ/N)x_2(1-x_2)]} dx_2$$

of equation [44] required for the range  $0 < x_3 < 1 - (\beta/Q)$  is expressed as

$$\frac{N}{PQ(\xi + \eta)} \left( \frac{2\gamma - N}{4} - \frac{N}{2} \log \frac{\beta}{Q} \right) \int_{x_3}^{1-(\beta/Q)} \left[ \frac{\xi}{\xi - x_2} - \frac{\eta}{\eta + x_2} \right] dx_2 \\ - \frac{N^2}{2PQ(\xi + \eta)} \int_{x_3}^{1-(\beta/Q)} \left[ \frac{1}{\xi - x_2} + \frac{1}{\eta + x_2} \right] dx_2 \\ - \frac{N^2}{2PQ} \int_{x_3}^{1-(\beta/Q)} \left[ \frac{1}{\xi \eta} \frac{1}{x_2} + \frac{1 - \xi^2}{\xi(\xi + \eta)} \frac{1}{\xi - x_2} + \frac{\eta^2 - 1}{\eta(\xi + \eta)} \frac{1}{\eta + x_2} \right] \log (1-x_2) dx_2$$

$$\text{where } PQ(\xi - x_2)(\eta + x_2) = N(1-P) + PQx_2 - PQx_2^2,$$

so that similar relations hold between  $\xi$  and  $\eta$ ,  $\alpha$  now being replaced by  $N$ .

In place of equation [47] one now has

$$I_3'''(x_3) = H(PQ) + \frac{N}{PQ} \left[ \frac{2\gamma - 3N}{4} - \frac{N}{2} \log \frac{\beta}{Q} \right] \\ \times \left[ \log (1-x_3) + \log \left( 1 + \frac{\eta}{1-x_3} \right) - \log \frac{\beta}{Q} - \log \left( 1 + \frac{\eta Q}{\beta} \right) \right] \\ + \frac{N^2}{2PQ} \left[ \log \left( 1 - \frac{1-x_3}{\xi} \right) - \log \left( 1 - \frac{\beta}{\xi Q} \right) \right] \\ + \frac{N}{2(1-P)} \left[ \log (1-x_3) \log x_3 - \log \left( 1 - \frac{\beta}{Q} \right) \log \frac{\beta}{Q} \right. \\ \left. + \sum_1^{\infty} \frac{(1-x_3)^n - (\beta/Q)^n}{n^2} \right] \\ [47a] \quad + \left[ \frac{N^2}{2PQ} - \frac{N}{2(1-P)} \right] \left[ \log \left( 1 - \frac{1-x_3}{\xi} \right) \log (1-x_3) \right. \\ \left. - \log \left( 1 - \frac{\beta}{\xi Q} \right) \log \frac{\beta}{Q} + \sum_1^{\infty} \frac{[(1-x_3)/\xi]^n - (\beta/\xi Q)^n}{n^2} \right] + O\left(\frac{1}{Q^2}\right)$$

and the term  $\log [1 + N(1 - P)/\beta P]$  arises from the fact that  $\log [1 + (\eta Q/\beta)] = \log [1 + N(1 - P)/\beta P] + O(1/Q)$ .

It is noticed that if  $P > 1$ , the terms  $\log [1 - (1 - x_3)/\xi]$  although required for the range  $0 \leq x_3 \leq 1 - (\beta/Q)$  cease to exist for  $x_3 < \frac{N(P-1)}{Q}$ , and that  $\sum_1^{\infty} \frac{[(1 - x_3)/\xi]^n}{n^2}$  becomes divergent over this subinterval of the range.

It follows then that, strictly speaking, equation [47a] cannot be applied for  $x_3 = 0$ , that is to give the important ratio  $(t_{\text{wall}} - t_{\text{axis}})/(t_{\text{wall}} - t_{\text{mean}})$ .

It can be shown however that the "device" of putting  $x_3 = 0$  in the expression [48] does in fact give this ratio to  $O(1/Q)$ .

Calling  $\bar{I}_3(0)$  the value of  $I_3(x_3)$  at  $x_3 = 0$ , then, since

$$\left[ \frac{\log(1 - x_3)}{x_3} \right]_{x_3=N(P-1)/PQ} = \lim_{x_3 \rightarrow 0} \frac{\log(1 - x_3)}{x_3} + O\left(\frac{1}{Q}\right),$$

it is seen that the result valid for the point  $x_3 = N(P - 1)/PQ$  is obtained to  $O(1/Q)$  by substituting  $\bar{I}_3(0)$  in equation [25].

It remains to show that  $(t_{\text{wall}} - t_{x_3=0})/(t_{\text{wall}} - t_{\text{mean}})$  differs from  $(t_{\text{wall}} - t_{x_3=N(P-1)/PQ})/(t_{\text{wall}} - t_{\text{mean}})$  by  $O(1/Q^2)$ .

From equation [44], for  $x_3 < 1 - (\beta/Q)$ , one has

$$x_3 \frac{\partial I_3}{\partial x_3} = \frac{[\frac{1}{4}(2\gamma - N) - \frac{1}{2}N \log(\beta/Q)]x_3^2 - \frac{1}{2}Nx_3 - \frac{1}{2}N(1 - x_3^2)\log(1 - x_3)}{[(P - 1) - (PQ/N)x_3(1 - x_3)]}$$

$$\text{so that } \left[ x_3 \frac{\partial I_3}{\partial x_3} \right]_{x_3=N(P-1)/PQ} = O\left(\frac{1}{Q^2}\right).$$

The application of Taylor's theorem to the function  $I_3$  about the point  $x_3 = N(P - 1)/PQ$  proves the result.

Again, in the final integration for the Nusselt modulus, the result to  $O(1/Q)$  is clearly unaffected if the subinterval  $0 \leq x_3 \leq N(P - 1)/PQ$  of length  $O(1/Q)$  is omitted from the range of integration.

#### REFERENCES

1. BOELTER, L. M. K., MARTINELLI, R. C., and JONASSEN, F. Trans. Am. Soc. Mech. Engrs. 447. 1941.
2. EAGLE, A. and FERGUSON, R. M. Proc. Roy. Soc. (London), A, 127: 540. 1930.
3. GOLDSTEIN, G. Modern developments in fluid dynamics. Oxford at the Clarendon Press. 1938. p. 210.
4. GOLDSTEIN, G. Modern developments in fluid dynamics. Oxford at the Clarendon Press. 1938. p. 331.
5. LYON, R. N. A.E.C.D. 1992. Oak Ridge National Laboratory. 1948.
6. MARTINELLI, R. C. Trans. Am. Soc. Mech. Engrs. 947. 1947.
7. NIKURADSE VER DEUTSCH ING FORSCHUNGSHEFT, 356. 1932.
8. REICHARDT, H. Z. angew. Math. u. Mech. 297. 1940.
9. SHEPPARD, W. A. M.S. Thesis, University of California at Berkeley. 1948.
10. STANTON, T. E. and PANNELL, J. R. Trans. Roy. Soc. (London), A, 214: 199. 1914.
11. TAYLOR, G. I. Trans. Roy. Soc. (London), A, 215: 1. 1915.
12. TAYLOR, G. I. Proc. Roy. Soc. (London), A, 135: 685. 1932.

# AN EXPERIMENTAL INVESTIGATION OF THE HEAT TRANSFER TO TURBULENTLY FLOWING PRESSURIZED AIR<sup>1</sup>

By A. W. MARRIS<sup>2</sup>

## ABSTRACT

Employing a counter-flow figure-of-eight heat exchanger, direct measurements are made of the Nusselt modulus for radial heat transfer to air pressurized up to 20 atmospheres for Reynolds numbers up to  $1.20 \times 10^6$ . For each heat transfer determination a simultaneous friction factor measurement is made and it is found that the latter is independent of heat transfer.

Results in reasonable agreement with the momentum transfer theory are obtained for Reynolds numbers less than  $0.75 \times 10^6$ , provided the ratio of the eddy diffusivities for heat and momentum is taken as unity. For such values of the Reynolds number, the same value of the heat transfer coefficient was obtained irrespective of whether the Reynolds number was obtained by having high pressure (density) and low velocity, or high velocity and low pressure. For higher values of the Reynolds number, however, the value of the heat transfer coefficient appeared to become dependent on the over-all heat transfer rate.

## 1. INTRODUCTION

In this study, using a figure-of-eight counter-flow heat exchanger of circular section, an attempt is made to determine directly the heat transfer coefficient for Reynolds moduli up to  $1.20 \times 10^6$  by the device of increasing density rather than speed of flow. The work was undertaken to investigate the constancy or otherwise of the ratio of the eddy diffusivities for heat and momentum of the momentum transfer analogy. As pressurized air is used as a coolant it is also of interest to know whether the heat transfer coefficient is in fact independent of the heat transfer rate.

It has been shown by Saunders (5) that the Prandtl modulus of air is sensibly independent of pressure and that the device of pressurization reduces errors caused by local heating due to compressibility.

Since the theory expresses the Nusselt modulus in terms of the tube friction factor as well as Reynolds and Prandtl moduli, the former was measured directly for each heat transfer determination.

## 2. PRINCIPAL NOMENCLATURE AND VALUES OF CONSTANTS OF APPARATUS

$L$  = length of stainless steel tube across which heat transfer takes place  
= 402.9 cm.

$r_t$  = internal radius of s.s. tube = 0.850 cm.

$A_t = \pi r_t^2$ .

$v_t$  = fluid velocity in s.s. tube in cm. per sec.

$S = 2\pi r_t L$ .

$k_{s.s.}$  = thermal conductivity of stainless steel tube = 0.038 c.g.s. units at  
15° C.

$b$  = thickness of wall of s.s. tube = 0.1025 cm.

<sup>1</sup> Manuscript received September 21, 1953.

Work carried out at the School of Engineering, University College Auckland, Auckland, New Zealand.

<sup>2</sup> Present address: Physics Department, University of British Columbia, Vancouver, B.C.

$Q$  = quantity of heat transferred to center stream per second  
 $= \text{Re Pr} (\frac{1}{2}\pi r_t) S \Delta T.$

$\text{Re}$  = Reynolds modulus  $= 2v_t r_t / \nu_t$ .

$\nu_t$  = kinematic viscosity of air at mid-point of s.s. tube.

$\text{Pr}$  = Prandtl modulus.

$s$  = molecular conductivity of air.

$T'$  = mean mixed inlet temperature.

$T''$  = mean mixed outlet temperature.

$\Delta T = T'' - T'$ .

$T_m = \frac{1}{2}(T' + T'') = T' + \frac{1}{2}\Delta T$  = temperature at which property values are taken.

$\delta T$  = (temperature of inside wall of s.s. tube) - (mean mixed temperature of stream).

$\delta T_x$  = (temperature of inside wall of s.s. tube at point a distance  $x$  from entrance) -  $(T' + (x/L)\Delta T)$ .

$\delta T'_x = \delta T_x + \epsilon$ .

$\epsilon$  = temperature drop across wall of s.s. tube  $= Qb/k_{s.s.}S$ .

$\delta p$  = pressure drop across orifice gauge in dynes per sq. cm.

$\delta q$  = pressure drop down stainless steel tube in dynes per sq. cm.

$f$  = Fanning friction factor for s.s. tube, defined by  $\delta q = f(L/r_t) \rho_t v_t^2$ .

$A_0$  = area of orifice in sq. cm.

$v_0$  = fluid velocity in orifice in cm./sec.

$A_p$  = area of pipe in which orifice plate is inserted.

$v_p$  = fluid velocity in pipe in cm./sec.

$m = A_p/A_0 = 2.6405$ .

$M = A_p/A_t = 2.3026$ .

$\rho_p$  = density of air in pipe at orifice.

$\rho_t$  = mean density of air in s.s. tube = density at temperature  $T_m$ .

$\lambda = \rho_p/\rho_t$ .

$\Pi$  = over-all pressure in apparatus in dynes per sq. cm.

$n = (\delta p + \frac{1}{2}\delta q)/\Pi$ .

$N$  = number of normal atmospheres pressure existing at mid-point of s.s. tube  $= (\Pi + \delta p + \frac{1}{2}\delta q)/76.00 = \Pi(1 + n)/76.00$ .

$\text{Nu} = \text{Nusselt modulus} = \frac{Q}{S\delta T} \left( \frac{2r_t}{s} \right) = \frac{r_t}{2L} \text{Re Pr} \frac{\Delta T}{\delta T}$ .

$Q = \text{Re} \sqrt{(f/8)}$ .

$\epsilon_H$  = eddy diffusivity for heat, the effective increase in thermal diffusivity due to turbulence.

$\epsilon_M$  = eddy diffusivity for momentum, the effective increase in kinematic viscosity due to turbulence.

$P = (\epsilon_H/\epsilon_M)\text{Pr}$ .

### 3. THE COUNTER-FLOW HEAT EXCHANGER

The mechanism of the counter-flow heat exchanger is shown schematically in Fig. 1. The cold fluid enters the long center tube from the left-hand mixing tank

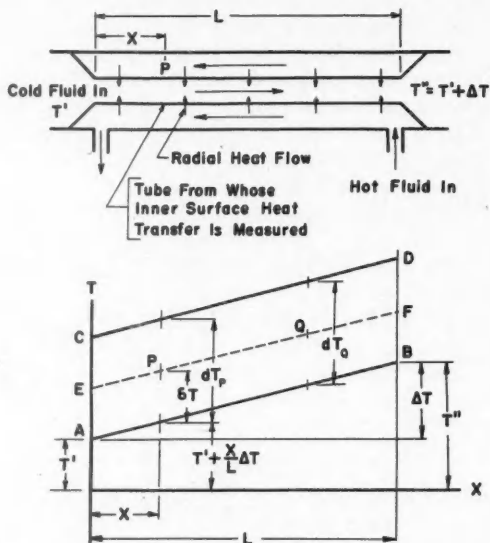


FIG. 1. Schematic representation of counter-flow heat exchanger.

at temperature  $T'$ . The hot fluid enters the annulus at the right and heat is transferred radially inwards across the center tube wall, so that the annulus fluid loses heat and the fluid under test in the center tube gains heat. This latter fluid leaves at a mixed temperature  $T''$  on the right,

$$[1] \quad T'' = T' + \Delta T.$$

By considering the heat flow across an element of surface area  $dS$  of the center tube it is easy to show (3) that if  $(dT)_P$  is the difference of the mean mixed temperatures of the streams at any point  $P$  then

$$[2] \quad (dT)_P / (dT)_Q = e^{-\mu U S}$$

where  $S$  is the surface area of the section  $PQ$  of the tube,  $U$  is the over-all heat transfer coefficient defined by

$$[3] \quad dQ = U dS dT,$$

$dQ$  being the quantity of heat flowing across  $dS$  in unit time, and  $\mu$  is the difference of the reciprocals of the thermal capacities of the fluids in the two streams, which is assumed constant along the tube length.

When  $U$  is assumed constant along the length of the tube it follows that if the thermal capacities of the two streams are equal, that is  $\mu$  is zero, then  $dT$  is constant along the tube length. Such a state of affairs is of course only realizable in practice when the temperature differences are infinitesimally small.

In the ideal case considered here, the mean temperature gradients of the two flows are parallel lines. In the diagram,  $AB$  represents that for inner stream and  $CD$  that for annulus stream. The temperature gradient along the inner tube  $EF$  must lie between these lines.

Writing  $\delta T$  = (temperature of inside wall of inner tube) - (mean mixed flow temperature of center stream fluid), then

$$[4] \quad \text{Nu} = \frac{r}{2L} \text{ Re Pr} \frac{\Delta T}{\delta T}.$$

#### 4. DESCRIPTION OF APPARATUS

The apparatus, built of mild steel except for the tube across which heat transfer was to take place and the orifice plate for measuring the flow velocity, was constructed for use with a compressor which, with appropriate adjustment of inlet and outlet valves, would simultaneously compress the air overall and drive it through the figure-of-eight circuit.

Air from the compressor, which had passed through a moisture separator and filter tank, was led through 1-1/64 in. internal diameter mild steel tubing; through a vertical 2 ft. long temperature stabilizing water jacket; horizontally through an over-all pressure measuring unit comprising two Bourdon gauges set in a turned section contained between two flanges, the gauges graduated to read 0-100 lb. per sq. in. and 0-300 lb. per sq. in. respectively; through a second horizontal water jacket; through the orifice gauge, the latter of the type German Standard Orifice 1930 (2), comprising a 1/8 in. thick stainless steel plate containing a 5/8 in. diameter orifice set between flanges in the 1-1/64 in. internal diameter tube; and thence to the left-hand "entrance" mixing tank of the heat exchanger.

This cylindrical tank 4-7/8 in. in length by 2-7/8 in. internal diameter contained first a three-bladed propeller mounted to revolve freely in the stream, and then equally spaced about the circumference of the tank, three thermocouple pyrometers. These, of length 1/2 in., 1 in., and 1-1/2 in., were 1/8 in. diameter mild steel tubes of 1/16 in. bore flanged at one end. The thermocouple wires had been threaded through the tubes and the head of the thermocouple soldered to the tube end to seal the 1/16 in. bore. This pyrometer could then be inserted into its "saddle", and the flange screwed down hard against a rubber ring, rendering the whole pressure tight.

From the left-hand mixing tank the stream entered a section which converged it into the 13 ft. long internally commercially polished 3/4 in. O.D., 17.00 mm. (average) I.D., Staybrite F.D.P. stainless steel tube from the inside surface of which the heat transfer to the center stream was to take place. The s.s. tube fitted into this converging unit, and in the slot encircling the tube was set a 3/4 in. "O" ring to prevent flow between the center and annulus streams. Also in this section was the first pressure tapping for measuring the pressure drop down the s.s. tube, and thence its friction factor.

A third unit was flanged to this converging unit, which comprised the exit for the annulus flow.

After it had left the s.s. tube the fluid passed through an identical unit which gripped the right end of the s.s. tube, took the second friction factor pressure tapping, and diverged the flow into the right-hand "exit" mixing tank which, like the "entry" mixing tank, contained a second free propeller and three more thermocouples arranged in the same way.

The flow continued horizontally for a few feet and was then led down and around and back into the annulus, having been heated by means of six (and later eight) 65-ohm coils wound on the tube. These heating coils, capable of being connected in series or parallel as required, were wound from resistance wire ribbon of 6.10 ohms per foot, and of cross-sectional dimension 0.312 in.  $\times$  0.0035 in. The wire was insulated from the tube with asbestos, and then the coils were covered with more asbestos to minimize external heat losses. The maximum voltage employed for the heaters was 270 volts.

After it had left the annulus tube the stream was then led downwards away from the working section (disturbances caused by the sudden expansion at the outlet could cause serious errors if the outlet were too close to the working section); through an open-shut valve (used in pressurizing the air prior to starting its bodily flow through the circuit); through a second Saunders diaphragm valve placed so that it could be adjusted simultaneously with the valve on the branch pipe near the inlet; past a needle valve for fine adjustment; and finally let out into the atmosphere.

The s.s. tube wall temperature was measured by three thermocouples soldered to the steel at distances  $\frac{1}{4}L$ ,  $\frac{1}{2}L$ , and  $\frac{3}{4}L$ . The temperature of the outside wall was thus measured, and the required inside wall temperature was then obtained by extrapolation, since the wall thickness, the thermal conductivity of the stainless steel, and the heat flowing radially inwards through the tube wall were known quantities.

To facilitate the affixing and inspection of these tube wall couples the outer tube of the working section was made up of four sections, which were flanged at the ends and connected to the annulus exit and entry units and the three tube wall thermocouple units by means of caps, which slid over the tube and screwed on to the appropriate unit, thereby squeezing the flanges against hard rubber pads.

The three tube wall thermocouple units also contained three legs with feet of lignum vitae—these were turned and collared and affixed to the steel legs with "Heldite"—to support the s.s. tube.

It was essential that both the junction itself and the leads to it, which necessarily crossed the annulus stream, be shielded from the stream. For this purpose a tube of bakelite impregnated paper was turned. The top end of the tube, which was drilled axially to take the thermocouple leads, was flanged and the lower end collared to take a soft rubber pad shaped to fit over the s.s. tube and surround the junction. The pad was attached to the tube with "Heldite". The flange end was screwed down against a hard rubber ring so that the lower end squeezed the softer pad against the s.s. tube, fulfilling the fourfold purpose of holding the s.s. tube rigidly against its supports; of rendering the installation pressure tight (in fact the thermocouple was not in the pressurized region); of making the soft rubber close over and clutch against the thermocouple wire immediately above the head, thus holding the thermocouple rigid and providing proof against inadvertent jerks; and finally of keeping the thermojunction and its leads free from extraneous heating or cooling created by the impingement of the annulus stream.

In this apparatus all the pipe and tank flanges, etc., were screwed to the pipes and tank sections, the pipe ends abutting against shoulders. Heldite was used as packing, and in cases where this gave leaks the threads were sweated together with solder. Again the corners and T-pieces were cut from blocks of metal, into which the pipes were similarly screwed.

Rings of cork impregnated paper, gaskets smeared on both faces with Heldite, were used as sealings at the spigots of all the flanges.

The working section of the apparatus, including the mixing tanks, was contained in a 20 ft. long pinex-lined wooden box, complete with lid. The box was built up of sections fitted together by tongue and slot joints.

The nine thermocouples, three for the determination of the center stream inlet temperature  $T'$ , three for the longitudinal gradient down the stainless steel tube, and three for the center stream outlet temperature, were constructed from gauge 21 (Imperial Standard) copper and constantan wires. No joints were made in the wires until they reached either the cold junction or the mercury switch. Since the cold junction was adjacent to the middle of the working section, the copper and constantan leads of the first and last three couples were 8 ft. long, while those of the three wall couples were 5 ft. long.

While it was necessary that all the nine cold junctions be at the same temperature to within  $1/50^{\circ}\text{C}$ ., it was only necessary that the cold junction temperature, giving the temperature level in the apparatus, be known to within say  $1/4^{\circ}\text{C}$ . It was thus decided that a cold junction consisting of distilled water contained in a vacuum flask, which was contained in a second larger flask, would be adequate.

The nine junctions were coated with "araldite" wire insulating material (made by Ciba products) and bound together so that the heads were in the closest possible proximity. After the wires and a mercury-in-glass thermometer graduated to read to  $1/20^{\circ}\text{C}$ . had been threaded through the corks and set in place, the cork holes were filled up with paraffin-wax.

The switch consisted simply of 24 mercury wells, bridged in pairs as required by the thick-tinned copper wires.

A Cambridge Vernier Potentiometer reading to  $\frac{1}{10}\text{ } \mu\text{v}$ . (about  $1/400^{\circ}\text{C}$ .) was employed for the measurement of the thermocouple e.m.f.'s.

The six mixing-tank thermocouples were removable and were calibrated at frequent intervals throughout the experiment. A facsimile of a tube-wall thermocouple was constructed with a short length of the stainless steel tube and calibrated. Likewise the orifice gauge was calibrated by timing the delivery of 250 lb. of water, and so also the pressure gauges.

##### 5. FORMULAE EMPLOYED

The Fanning friction factor for the s.s. tube defined by

$$[5] \quad \delta q = f \frac{L}{r_t} \rho_t v_t^2$$

may be expressed as

$$[6] \quad \frac{1}{f} = C^2 x^2 \frac{M^2}{m^2 - 1} \frac{2L}{r_t} \lambda \frac{\delta p}{\delta q}$$

where  $C$  is the compressibility factor of orifice gauge defined by

$$[7] \quad C = 1 - 0.346 \frac{\delta p}{\Pi}$$

and  $\chi$  is the orifice coefficient determined as a function of Reynolds number from the calibration.

Neglecting pressure head loss and temperature difference between orifice gauge and entry mixing tank, one has

$$[8] \quad \lambda = (1 + \frac{1}{2}\alpha\Delta T)(1 + n) = 1 + n + \frac{1}{2}\alpha\Delta T$$

and taking the appropriate value of the density variation coefficient from the Critical tables,

$$[9] \quad \lambda = 1 + n + 1.9 \times 10^{-3}\Delta T.$$

When the numerical values of the apparatus constants are inserted, the friction factor is given by

$$[10] \quad \frac{1}{f} = 841.58 \left( 1 - 0.692 \frac{\delta p}{\Pi} \right) \chi^2 (1 + n + 1.9 \times 10^{-3}\Delta T) \frac{\delta p}{\delta q}.$$

For the Reynolds modulus one has the result

$$[11] \quad \text{Re}^2 = 8 \left[ \frac{M^2}{m^2 - 1} \right] r_t^2 [C^2 \chi^2 \lambda] \frac{\delta p}{\nu_t^2 \rho_t}$$

where, utilizing Boyd's (1) result of a 4% linear increase in viscosity for 25 atm. pressure,

$$[12] \quad \nu_t^2 \rho_t = \frac{2.2854 \times 10^{-5}}{N} (1 + 3.2 \times 10^{-3}N + 9.42 \times 10^{-3}T_m)$$

so that finally, on substituting the requisite numerical values,

$$[13] \quad \text{Re}^2 = 2.2452 (1 - 0.692 \frac{\delta p}{\Pi}) \chi^2 \{ 1 + \frac{1}{2} (1.9\Delta T - 3.2N - 9.42T_m) \times 10^{-3} \} N \delta p \times 10^5.$$

The Nusselt modulus is given by

$$[4] \quad \text{Nu} = \frac{r_t}{2L} \text{Re} \text{Pr} \frac{\Delta T}{\delta T}.$$

The Prandtl modulus of air is independent of pressure but depends on the temperature according to

$$[14] \quad (\text{Pr})_{T_m} = 0.712 (1 - 3.09 \times 10^{-4}T_m).$$

In the experiment,  $\delta T$ , required to be the difference between the inside wall temperature of the heat transfer tube and the mean mixed flow temperature, is taken as the arithmetic mean of the three values of  $\delta T_x$  corresponding to  $x = \frac{1}{4}L$ ,  $x = \frac{1}{2}L$ ,  $x = \frac{3}{4}L$ , where  $\delta T_x$  is defined as (temperature of inside wall of tube) - ( $T' + (x/L) \Delta T$ ).

After the temperature of the outside wall of the s.s. tube was measured it was necessary to correct for the temperature drop across the wall of the tube.

One has

$$[15] \quad \delta T_x = \delta T'_x - \epsilon_x,$$

where  $\delta T_x'$  = measured quantity, (temperature of *outside* wall of s.s. tube)  $- (T' + (x/L) \Delta T)$ ,  
and  $\epsilon_x$  = temperature drop across the tube wall at the point  $x$ .

An average value  $\epsilon$  of  $\epsilon_x$  is given by

$$[16] \quad \epsilon = \frac{Qb}{k_{s.s.} S} = \text{Re} \text{Pr} \Delta T \frac{b}{4L} \frac{s}{k_{s.s.}}$$

and for the Nusselt modulus one has

$$[17] \quad \text{Nu} = 0.7511 \text{Re} \frac{\Delta T}{\delta T} (1 - 3.09 \times 10^{-4} T_m) \left( 1 + 7.78 \text{Re} \frac{\Delta T}{\delta T} \times 10^{-8} \right) \times 10^{-3}$$

where  $\delta T$  refers to the outside wall temperature as measured and is the mean of the three values.

## 6. RESULTS

The values of the reciprocals of the friction factor obtained for the stainless steel heat transfer tube are plotted in Fig. 2. To each point there corresponds a

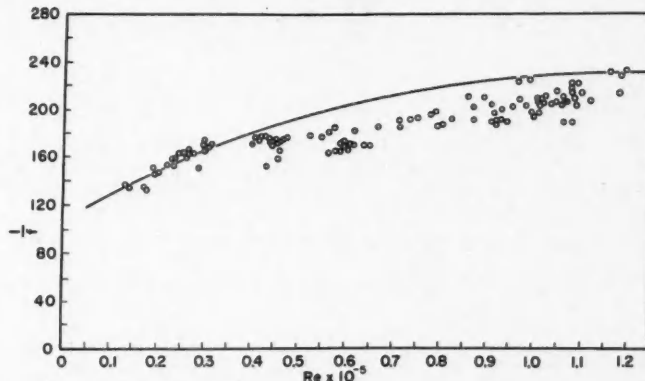


FIG. 2. Experimental values of Fanning friction factor. Continuous curve is von Karman's law for a smooth tube.

Nusselt modulus determination, see below. The continuous line is von Karman's curve

$$[18] \quad 1/f = (4.0 \log_{10} Q + 1.4062)^2$$

where  $Q = \text{Re} \sqrt{f/8}$

appropriate to a smooth tube.

No variation in  $f$  with heat transfer rate could be detected.

Fig. 3 shows the totality of values of the product  $\text{Nu}f$  for Reynolds numbers less than  $0.75 \times 10^5$ , and the continuous lines give the theoretical values (4) appropriate to Prandtl moduli of 0.55 and 0.75, these calculated on the basis of a linear temperature gradient along the tube length.

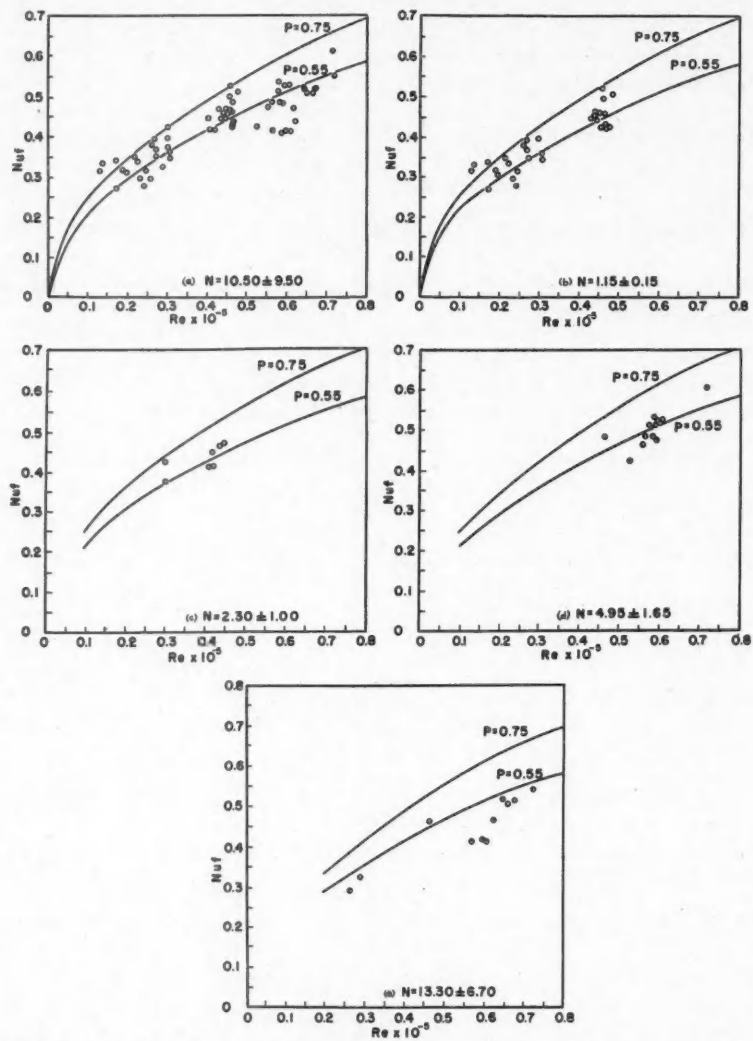


FIG. 3. (a) Totality of values of  $N_{uf}$  obtained for Reynolds numbers less than  $0.75 \times 10^5$  and over-all pressure between 1 and 20 atmospheres. Continuous lines are theoretical curves for  $P = 0.55$  and  $P = 0.75$  where  $P = kPr$  and  $k$  is the ratio of the eddy diffusivities for heat and momentum.

- (b) Subset from Fig. 3 (a) for over-all pressure between 1.00 and 1.30 atmospheres.
- (c) Subset from Fig. 3 (a) for over-all pressure between 1.30 and 3.30 atmospheres.
- (d) Subset from Fig. 3 (a) for over-all pressure between 3.30 and 6.60 atmospheres.
- (e) Subset from Fig. 3 (a) for over-all pressure between 6.60 and 20.00 atmospheres.

It is seen that up to  $Re = 0.75 \times 10^5$ , approximately the same value of  $Nuf$  is obtained irrespective of whether the value of the Reynolds number is obtained by velocity or by pressure (density), and that if the Prandtl modulus for air is taken as 0.70, then the value of the ratio  $\epsilon_H/\epsilon_M$  is unity.

For Reynolds numbers above  $0.75 \times 10^5$  it was found that, whether the turbulence be obtained by pressure or velocity, the value of  $Nuf$  was governed by another parameter,  $\Delta T$ , the excess of the outlet mixing tank temperature over the inlet mixing tank temperature, a quantity which for a given Reynolds number is directly proportional to the heat transfer rate.

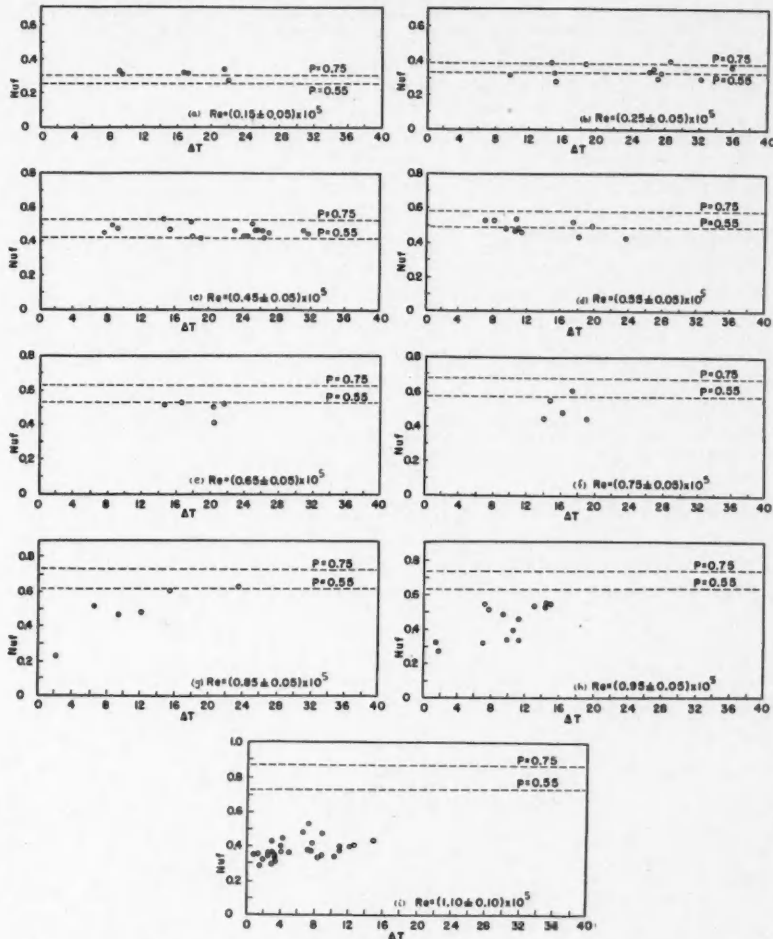


FIG. 4.  $Nuf$  against  $\Delta T$ , representing heat transfer rate, for Reynolds numbers confined between given limits.

The graphs of Fig. 4 now indicate  $Nu_f$  as a function of  $\Delta T$  (of heat transfer rate) for Reynolds numbers confined in each case between definite limits, the variation in its value through Reynolds numbers varying between these limits being sufficiently small not to obscure the  $\Delta T$  variation. On each of these graphs, for comparison, are given the corresponding theoretical values of  $Nu_f$  (4) for  $Pr = 0.55$  and  $Pr = 0.75$  appropriate to the mean value of  $Re$  for the range considered.

## REFERENCES

1. BOYD, J. H. Phys. Rev. (2), 35: 1284. 1930.
2. British Standard 1042. Code for flow measurement. 1943.
3. ECKERT, E. Introduction to the transfer of heat and mass. McGraw-Hill Book Company, Inc., New York. 1950. p. 262.
4. MARRIS, A. W. Can. J. Phys. 32: 167. 1954.
5. SAUNDERS, O. A. Proc. Roy. Soc. (London), A, 157: 278. 1936.

## NOTE

VIBRATIONAL TRANSITION PROBABILITIES TO HIGH QUANTUM NUMBERS  
FOR THE NITROGEN FIRST AND SECOND POSITIVE BAND SYSTEMS

BY W. R. JARMAIN AND R. W. NICHOLLS

As part of a study of the vibrational transition probability arrays for molecular band systems of specific astrophysical interest, an analytical method of computing the overlap integrals of the vibrational wave functions involved has been developed (2, 4, 8). Depending upon the way in which the method is applied, reliable results may be obtained without undue tedium either for bands the sum of whose quantum numbers does not exceed about 6, or for any band one of whose quantum numbers does not exceed about 3, the other quantum number remaining unrestricted. These bands usually include the vertex of the Condon parabola of the system concerned, and are also often just those bands which are of astrophysical interest.

Prior to the development of this method, however, extensive tables had been obtained for certain band systems by the straightforward, though extremely tedious method of numerical integration of accurately computed Morse wave functions, over a much larger range of vibrational quantum numbers than has been previously reported (3, 5). These more extensive data have been found

TABLE I

VIBRATIONAL TRANSITION PROBABILITIES FOR THE FIRST POSITIVE ( $B^3\Pi_g \rightarrow A^3\Sigma_u^+$ ) BAND SYSTEM OF NITROGEN

$v'$	$v''$	0	1	2	3	4	5	6	7	8	9	10	11	12
0		.34 <sub>0</sub>	.32 <sub>3</sub>	.19 <sub>0</sub>	.08 <sub>8</sub>	.03 <sub>6</sub>	.01 <sub>4</sub>	.00 <sub>5</sub>	.00 <sub>2</sub>					
1		.40 <sub>6</sub>	.00 <sub>2</sub>	.10 <sub>3</sub>	.17 <sub>7</sub>	.14 <sub>8</sub>	.08 <sub>9</sub>	.04 <sub>2</sub>	.01 <sub>5</sub>	.00 <sub>9</sub>	.00 <sub>4</sub>	.00 <sub>2</sub>		
2		.20 <sub>0</sub>	.21 <sub>2</sub>	.11 <sub>3</sub>	.00 <sub>2</sub>	.07 <sub>4</sub>	.12 <sub>6</sub>	.11 <sub>9</sub>	.07 <sub>8</sub>	.04 <sub>3</sub>	.02 <sub>1</sub>	.00 <sub>8</sub>	.00 <sub>5</sub>	.00 <sub>2</sub>
3		.05 <sub>0</sub>	.30 <sub>1</sub>	.03 <sub>8</sub>	.16 <sub>1</sub>	.03 <sub>1</sub>	.00 <sub>9</sub>	.06 <sub>9</sub>	.09 <sub>7</sub>	.08 <sub>9</sub>	.07 <sub>6</sub>	.04 <sub>1</sub>	.02 <sub>1</sub>	.01 <sub>2</sub>
4		.00 <sub>6</sub>	.13 <sub>4</sub>	.27 <sub>3</sub>	.00 <sub>1</sub>	.11 <sub>3</sub>	.08 <sub>6</sub>	.00 <sub>4</sub>	.01 <sub>8</sub>	.06 <sub>3</sub>	.08 <sub>4</sub>	.08 <sub>6</sub>	.05 <sub>5</sub>	.03 <sub>6</sub>
5			.02 <sub>7</sub>	.21 <sub>0</sub>	.18 <sub>4</sub>	.04 <sub>6</sub>	.04 <sub>4</sub>	.10 <sub>4</sub>	.03 <sub>7</sub>	.00 <sub>0</sub>	.02 <sub>3</sub>	.05 <sub>7</sub>	.07 <sub>3</sub>	.06 <sub>3</sub>
6			.00 <sub>3</sub>	.05 <sub>9</sub>	.25 <sub>9</sub>	.08 <sub>3</sub>	.10 <sub>7</sub>	.00 <sub>3</sub>	.08 <sub>4</sub>	.07 <sub>4</sub>	.01 <sub>4</sub>	.00 <sub>2</sub>	.02 <sub>8</sub>	.05 <sub>1</sub>
7				.00 <sub>8</sub>	.10 <sub>3</sub>	.26 <sub>9</sub>	.02 <sub>0</sub>	.12 <sub>8</sub>	.00 <sub>6</sub>	.04 <sub>0</sub>	.07 <sub>6</sub>	.03 <sub>6</sub>	.00 <sub>3</sub>	.00 <sub>6</sub>
8					.01 <sub>8</sub>	.16 <sub>1</sub>	.24 <sub>0</sub>	.00 <sub>0</sub>	.11 <sub>8</sub>	.03 <sub>5</sub>	.01 <sub>0</sub>	.06 <sub>8</sub>	.06 <sub>1</sub>	.01 <sub>7</sub>
9						.00 <sub>2</sub>	.03 <sub>5</sub>	.20 <sub>1</sub>	.18 <sub>8</sub>	.01 <sub>6</sub>	.07 <sub>7</sub>	.06 <sub>8</sub>	.00 <sub>0</sub>	.03 <sub>3</sub>
10							.00 <sub>4</sub>	.05 <sub>4</sub>	.22 <sub>8</sub>	.13 <sub>0</sub>	.05 <sub>6</sub>	.03 <sub>7</sub>	.08 <sub>1</sub>	.01 <sub>4</sub>
11								.00 <sub>4</sub>	.08 <sub>6</sub>	.26 <sub>7</sub>	.06 <sub>0</sub>	.08 <sub>0</sub>	.01 <sub>0</sub>	.07 <sub>3</sub>
12									.01 <sub>2</sub>	.11 <sub>6</sub>	.26 <sub>7</sub>	.03 <sub>0</sub>	.10 <sub>7</sub>	.00 <sub>0</sub>

useful in the interpretation of laboratory spectra where large vibrational quantum numbers are often encountered. They are therefore reported below. The entries in Tables I and II represent  $p(v', v'') = |\int \psi(v') \psi(v'') dr|^2$  where  $\psi(v')$  is the wave function of the upper vibrational level  $v'$ , and  $\psi(v'')$  is the wave function of the lower vibrational level  $v''$ .  $r$  is the internuclear separation. Table III shows the basic molecular data employed.

TABLE II  
VIBRATIONAL TRANSITION PROBABILITIES FOR THE SECOND POSITIVE ( $C^3\Pi_u \rightarrow B^3\Pi_g$ ) BAND SYSTEM OF NITROGEN

$v'$	$v''$	0	1	2	3	4	5	6	7	8	9	10	11	12
0	0	.44 <sub>8</sub>	.32 <sub>8</sub>	.14 <sub>6</sub>	.05 <sub>2</sub>	.01 <sub>6</sub>	.00 <sub>5</sub>	.00 <sub>1</sub>						
1	1	.39 <sub>3</sub>	.01 <sub>9</sub>	.20 <sub>3</sub>	.19 <sub>5</sub>	.11 <sub>5</sub>	.04 <sub>7</sub>	.02 <sub>0</sub>	.00 <sub>6</sub>	.00 <sub>1</sub>	.00 <sub>1</sub>			
2	2	.13 <sub>5</sub>	.32 <sub>3</sub>	.03 <sub>2</sub>	.06 <sub>2</sub>	.15 <sub>8</sub>	.14 <sub>2</sub>	.08 <sub>2</sub>	.03 <sub>9</sub>	.01 <sub>6</sub>	.00 <sub>6</sub>	.00 <sub>2</sub>	.00 <sub>1</sub>	
3	3	.02 <sub>2</sub>	.25 <sub>8</sub>	.16 <sub>3</sub>	.11 <sub>6</sub>	.00 <sub>2</sub>	.09 <sub>2</sub>	.14 <sub>1</sub>	.10 <sub>7</sub>	.05 <sub>7</sub>	.02 <sub>4</sub>	.01 <sub>5</sub>	.00 <sub>2</sub>	.00 <sub>2</sub>
4	4	.00 <sub>2</sub>	.07 <sub>0</sub>	.30 <sub>3</sub>	.04 <sub>8</sub>	.15 <sub>6</sub>	.01 <sub>8</sub>	.03 <sub>2</sub>	.09 <sub>8</sub>	.11 <sub>8</sub>	.07 <sub>7</sub>	.04 <sub>0</sub>	.01 <sub>7</sub>	.01 <sub>0</sub>

TABLE III  
MOLECULAR CONSTANTS  
(The notation is the same as that used in Reference 8)

State	$\omega_e$ (cm. <sup>-1</sup> )	$\omega_e x_e$ (cm. <sup>-1</sup> )	$\mu$ (at. wt. units)	$r_e$ (Å)	$\alpha$ (cm. <sup>-1</sup> )	$K$
$C^3\Pi$	2035.1	17.08	7.00377	1.1482	$2.6636 \times 10^8$	119.15
$B^3\Pi$	1734.11	14.47	7.00377	1.2123	$2.4517 \times 10^8$	119.84
$A^3\Sigma$	1460.37	13.891	7.00377	1.293	$2.4021 \times 10^8$	105.13

Table I contains results for the First Positive System ( $B^3\Pi \rightarrow A^3\Sigma$ ) of  $N_2$  over the ranges of vibrational quantum numbers  $0 \leq v' \leq 12$ ,  $0 \leq v'' \leq 12$ .

Table II contains results for the Second Positive System ( $C^3\Pi \rightarrow B^3\Pi$ ) of  $N_2$  over the ranges of vibrational quantum numbers  $0 \leq v' \leq 4$ ,  $0 \leq v'' \leq 12$ . These values, of course, supersede earlier provisional results (6, 7), which were computed under simplifying approximations upon the form of vibrational wave functions.

Figs. 1 and 2 plot these numerical data diagrammatically to indicate main and subsidiary Condon parabolae and also to show how the oscillator strength for the electronic transition is shared among the bands. The trends suggested by similar figures for the dependence of the overlap integrals in  $v'$  or  $v''$  progressions upon the varying quantum number have prompted some analytical examination of the situation. A more detailed discussion of this work will be reported later.

It should be realized that the numbers in Tables I and II are accurately computed values of an approximation to the 'true' vibrational transition

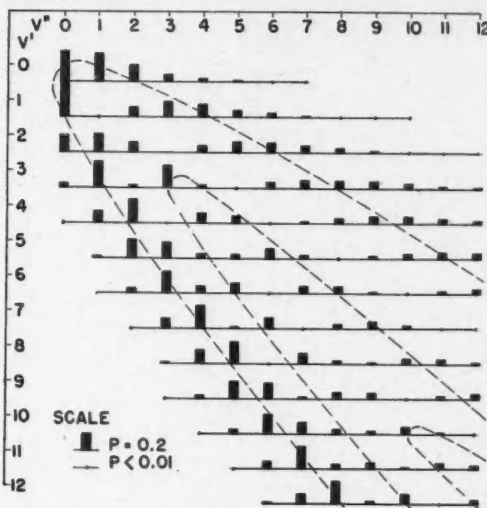


FIG. 1. Block diagram of the vibrational transition probability array, together with Condon parabolae, for the First Positive band system of nitrogen.

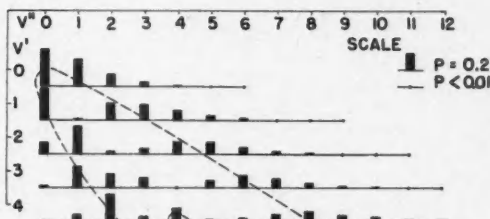


FIG. 2. Block diagram of the vibrational transition probability array, together with Condon parabolae, for the Second Positive band system of nitrogen.

probabilities because the electronic transition moment  $R_e(r)$  has been assumed independent of  $r$  in the familiar transition integral  $\int \psi(v') R_e(r) \psi(v'') dr$ . However, it may be briefly reported here that Turner and Nicholls have recently used the data of Table I together with computed values of the integrals  $\int \psi(v') \psi(v'') r dr$ ,  $\int \psi(v') \psi(v'') r^2 dr$  for the same bands and experimentally measured values of their intensities to determine the dependence of  $R_e(r)$  upon  $r$  by a method suggested by Fraser (1). Further details of this work will be published soon.

In the interests of brevity, references to the work of other investigators on comparable problems in molecular transition probabilities have not been made here, but will be found elsewhere in more complete discussions (2, 4, 5).

The studies reported in this note are part of a project supported by the Air Force Cambridge Research Centre with Contract AF 19(122)-470.

1. FRASER, P. A. Private communication.
2. FRASER, P. A. and JARMAIN, W. R. Proc. Phys. Soc. (London), A, 66: 1145. 1953.
3. FRASER, P. A., JARMAIN, W. R., and NICHOLLS, R. W. Astrophys. J. January, 1954.
4. JARMAIN, W. R. and FRASER, P. A. Proc. Phys. Soc. (London), A, 66: 1153. 1953.
5. JARMAIN, W. R., FRASER, P. A., and NICHOLLS, R. W. Astrophys. J. 118: 228. 1953.
6. MONTGOMERY, C. E. and NICHOLLS, R. W. Phys. Rev. 82: 565. 1951.
7. NICHOLLS, R. W. Phys. Rev. 77: 421. 1950.
8. NICHOLLS, R. W., JARMAIN, W. R., and FRASER, P. A. Can. J. Phys. 31: 1019. 1953.

RECEIVED NOVEMBER 10, 1953.  
DEPARTMENT OF PHYSICS,  
UNIVERSITY OF WESTERN ONTARIO,  
LONDON, ONTARIO.





# CANADIAN JOURNAL OF PHYSICS

## Notes to Contributors

### Manuscripts

(i) **General.** Manuscripts should be typewritten, double spaced, on paper  $8\frac{1}{2} \times 11$  in. The original and one copy are to be submitted. Tables (each typed on a separate sheet) and captions for the figures should be placed at the end of the manuscript. Every sheet of the manuscript should be numbered.

Style, arrangement, spelling, and abbreviations should conform to the usage of this journal. Names of all simple compounds, rather than their formulas, should be used in the text. Greek letters or unusual signs should be written plainly or explained by marginal notes. Superscripts and subscripts must be legible and carefully placed.

Manuscripts should be carefully checked before they are submitted; authors will be charged for changes made in the proof that are considered excessive.

(ii) **Abstract.** An abstract of not more than about 200 words, indicating the scope of the work and the principal findings, is required, except in Notes.

(iii) **References.** References should be listed alphabetically by authors' names, numbered, and typed after the text. The form of the citations should be that used in this journal; in references to papers in periodicals, titles should not be given and only initial page numbers are required. All citations should be checked with the original articles and each one referred to in the text by the key number.

(iv) **Tables.** Tables should be numbered in roman numerals and each table referred to in the text. Titles should always be given but should be brief; column headings should be brief and descriptive matter in the tables confined to a minimum. Numerous small tables should be avoided.

### Illustrations

(i) **General.** All figures (including each figure of the plates) should be numbered consecutively from 1 up, in arabic numerals, and each figure referred to in the text. The author's name, title of the paper, and figure number should be written in the lower left corner of the sheets on which the illustrations appear. Captions should not be written on the illustrations (see Manuscript (i)).

(ii) **Line Drawings.** Drawings should be carefully made with India ink on white drawing paper, blue tracing linen, or co-ordinate paper ruled in blue only; any co-ordinate lines that are to appear in the reproduction should be ruled in black ink. Paper ruled in green, yellow, or red should not be used unless it is desired to have all the co-ordinate lines show. All lines should be of sufficient thickness to reproduce well. Decimal points, periods, and stippled dots should be solid black circles large enough to be reduced if necessary. Letters and numerals should be neatly made, preferably with a stencil (**do NOT use typewriting**), and be of such size that the smallest lettering will be not less than 1 mm. high when reproduced in a cut 3 in. wide.

Many drawings are made too large; originals should not be more than 2 or 3 times the size of the desired reproduction. In large drawings or groups of drawings the ratio of height to width should conform to that of a journal page but the height should be adjusted to make allowance for the caption.

**The original drawings and one set of clear copies (e.g. small photographs) are to be submitted.**

(iii) **Photographs.** Prints should be made on glossy paper, with strong contrasts. They should be trimmed so that essential features only are shown and mounted carefully, with rubber cement, on white cardbord.

As many photographs as possible should be mounted together (with a very small space between each photo) to reduce the number of cuts required. Full use of the space available should be made and the ratio of height to width should correspond to that of a journal page; however, allowance must be made for the captions. Photographs or groups of photographs should not be more than 2 or 3 times the size of the desired reproduction.

**Photographs are to be submitted in duplicate;** if they are to be reproduced in groups one set should be mounted, the duplicate set unmounted.

### Reprints

A total of 50 reprints of each paper, without covers, are supplied free. Additional reprints, with or without covers, may be purchased.

Charges for reprints are based on the number of printed pages, which may be calculated approximately by multiplying by 0.6 the number of manuscript pages (double-spaced typewritten sheets,  $8\frac{1}{2} \times 11$  in.) and making allowance for illustrations (not inserts). The cost per page is given on the reprint requisition which accompanies the galley.

Any reprints required in addition to those requested on the author's reprint requisition form must be ordered officially as soon as the paper has been accepted for publication.

## Contents

	Page
Counting Slow Electrons with an Electron Multiplier— <i>J. A. Cowan</i>	101
Fine Structure of the Schumann-Runge Bands near the Convergence Limit and the Dissociation Energy of the Oxygen Molecule— <i>P. Brix and G. Herzberg</i>	110
Photoneutrons in a Heavy Water Pile— <i>M. W. Johns and B. W. Sargent</i>	136
Disintegration of $Au^{196}$ — <i>L. G. Elliott, M. A. Preston, and J. L. Wolfson</i>	153
On the Nusselt Modulus as a Function of Friction Factor, Reynolds and Prandtl Moduli, for Heat Transfer to a Fluid Flowing Turbulently Through a Tube of Circular Section— <i>A. W. Marris</i>	167
An Experimental Investigation of the Heat Transfer to Turbulently Flowing Pressurized Air— <i>A. W. Marris</i>	190
Vibrational Transition Probabilities to High Quantum Numbers for the Nitrogen First and Second Positive Band Systems— <i>W. R. Jarmain and R. W. Nicholls</i>	201

